Methods Toward Improved Lower Extremity Rehabilitation

by

IAHN CAJIGAS GONZÁLEZ
B.Sc., Electrical Engineering & Computer Science
Massachusetts Institute of Technology (2002)
M.Eng., Electrical Engineering & Computer Science
Massachusetts Institute of Technology (2003)

Submitted to the Department of Health Sciences & Technology
in partial fulfillment of the requirements for the degree of

Doctor of Philosophy in Electrical and Medical Engineering

at the

MASSACHUSETTS INSTITUTE OF TECHNOLOGY

May 2012
[June 2012]

Signature of Author: .....
Department of Health Sciences & Technology
May 17, 2012

Certified by: .....
Emery N. Brown, M.D., Ph.D.
Professor of Computational Neuroscience and Health Sciences & Technology
Thesis Supervisor

Certified by: .....
Paolo Bonato, Ph.D.
Assistant Professor of Physical Medicine and Rehabilitation
Thesis Supervisor

Accepted by: .....
Ram Sasisekharan, Ph.D.
Edward Hood Taplin Professor of Health Sciences & Technology
and Biological Engineering
Director, Harvard-MIT Division of Health Sciences & Technology

Methods Toward Improved Lower Extremity Rehabilitation

by

Iahn Cajigas González

Submitted to the Department of Health Sciences & Technology
on May 21, 2012 in partial fulfillment of the
requirements for the degree of
Doctor of Philosophy in Electrical and Medical Engineering

Abstract

Ambulation is a very important part of everyday life and its absence has a detrimental effect on an individual's quality of life. While much is understood about the neurobiological systems involved in locomotion through detailed anatomical connectivity and lesion studies, it is not well understood how neurons across different regions of the nervous system share information and coordinate their firing activity to achieve ambulation. Moreover, while it is clear that understanding the processes involved in healthy ambulation are essential to understanding how diseases affect an individual's ability to walk, diseases such as stroke tend to "take out" large portions of the underlying system. Until technologies are developed to allow restoration of damaged neural tissue back to its original state, physical therapy (which aims to restore function by establishing new motor-cortical connections among the remaining neurons) remains the most viable option for patients. The aim of this thesis is to elucidate some of the underlying neurobiological mechanisms of walking and to develop tools for rehabilitation robotics that allow finer quantification of patient improvement. To elucidate the neural mechanisms of locomotion, we studied how task relevant information (e.g. positions, velocities, and forces) modulate single unit neural activity from hindlimb/trunk region of the rat motor cortex during adaptations to robot-applied elastic loads and closed-loop brain-machine-interface (BMI) control during treadmill locomotion. Using the Point Process-Generalized Linear Model (PP-GLM) statistical framework we systematically tested parametric and non-parametric point process models of increased complexity for 573 individual neurons recorded over multiple days in six animals. The developed statistical model captures within gait-cycle modulation, load-specific modulation, and intrinsic neural dynamics. Our proposed model accurately describes the firing statistics of 98.5% (563/573) of all the recorded units and allows characterization of the neural receptive fields associated with gait phase and loading force. Understanding how these receptive fields change during training and with experience will be central to developing rehabilitation strategies that optimize motor adaptations and motor learning. The methods utilized for this analysis

were developed into an open source neural Spike Train Analysis Toolbox (nSTAT) for Matlab (Mathworks, Natick MA). Systematic analyses have demonstrated the effectiveness of physical therapy, but have been unable to determine which approaches tend to be most effective in restoring function. This is likely due to the multitude of approaches, diseases, and assessment scales used. To address this issue, we develop an extension of the Force Field Adaptation Paradigm, originally developed to quantitatively assess upper extremity motor adaptation, to the lower extremity. The algorithm is implemented on the Lokomat (Hocoma HG) lower extremity gait orthosis and is currently being utilized to assess short-term motor adaptation in 40 healthy adult subjects (ClinicalTrials.gov NCT01361867). Establishing an understanding of how healthy adults' motor systems adapt to external perturbations will be important to understanding how the adaptive mechanisms involved in gait integrate information and how this process is altered by disease.

Thesis Supervisor: Emery N. Brown, M.D., Ph.D.
Thesis Supervisor: Paolo Bonato, Ph.D.

Acknowledgments

Sir Isaac Newton once said: "If I have seen further it is only by standing on the shoulders of giants." I can today say that everything that I have accomplished would be impossible if it were not for the proverbial "giants" in my life. I am indebted to my PhD mentors, Paolo Bonato and Emery Brown. They believed in me when I was not even sure of what my PhD project would become and set a wonderful example of what it means to passionate and dedicated to research. I am extremely fortunate to call the members of the Neuroscience Statistics Research Laboratory (NSRL) at MIT and the Motion Analysis Laboratory (MAL) at Spaulding Rehabilitation hospital my dear friends and colleagues. At NSRL, thanks to Francisco Flores, Antonio Molins, Camilo Lamus, Demba Ba, Zhe Chen, Rob Haslinger, Veronica Weiner, Julie Hartin, Riccardo Riccardo Barbieri, Wasim Malik, Sheri Leone, and David P. Nguyen; and at the MAL, Shyamal Patel, Chiara Mancinelli, Caiomhe Bennis, Chek-Wai Bok, Alan Dunne, Lynn Deming, Ellen Connors, Mel Meister, Giacomo Severini, Maciej Pietrusinski, Özer Ünlühisarcikli, and Yalgin Muzaffer Özseçen. I am indebted to my collaborators Heike Vallery, Maurice Smith, Alexander Duschau-Wicke, Robert Riener, Weiguo Song, and Simon Giszter.

I have been fortunate to mentor three masters students during my PhD: Mary Goldsmith, Nicolas Beuchat, and William Cusack. Thank you guys for being so patient with me. You constantly challenged me to become a better teacher and helped me learn to think about problems from many different perspectives. It was a privilege to work with such talented students, and I'm quite fortunate to call you all my friends even after all the torture of making you write your theses!

Thanks to all of my wonderful friends at MIT over the many many years that I have been at the 'tute: friends: Vincent Cheung, Rumi Chunara, Gustavo Santos, Carlos Gomez Uribe, Anne Dreyer, Kazutaka Takahashi, Sungho Jo, Ola Ayaso, Angela S. Bassa, Naveen Goela, Federico Ardila, Eduardo Torres-Jara, Rebeca Hwang, Vijay Divi, Ezra Rosen, Lakshminarayan Srinivasan, Ali Shoeb, and Sourav Dey. The numerous late night conversations while working on problem sets, between and outside of classes have truly given me the best memories. Thanks to Steve G. Massaquoi for being such an amazing mentor during my MEng thesis at MIT and for showing me that medicine and engineering can coexist. Without you, I would have never thought about pursuing an MD-PhD. Thanks to Paul Gray, Munther Dahleh, Roger Mark, Phillip Clay, Richard Melrose, Mark Harvey, Emilio Bizzi, and George Verghese for being amazing role models, mentors, and teachers.

I'm fortunate to have taken time off from graduate school and enrolled in Harvard Medical School where I met the most passionate and dedicated individuals first as classmates and then as friends. Thank you for being so amazing, loyal, and

supportive: Evgeniy Kreydin, Vincent Auyeung, Dunia Abdul-Aziz, Marie Hollenhorst, Peter Miller, Nelson Moussazadeh, Vijay Ganesh, Xavier Rios, and Takahiro Soda. Thanks to all the faculty and staff at the MD-PhD office HMS for helping me with all of the paperwork that comes from living between MIT and HMS. In particular, Steve Blacklow, Thomas Michel, Yi Shen, Amy I. Cohen, Linda Burnley, David E. Golan, and Maria Rupnick. During my brief time in the wards I interacted with some amazing clinicians that exemplified what being dedicated to patient care is all about. I owe the image of the physician I strive to become, to the caliber of physicians that you are - Marcelo Montorzi, Samuel O. Thier, Yi Bin Shen, Emily Hyle, Roby Bhattacharyya, and Luke J. Engelking.

Outside of school, I have been surrounded by amazing friends. Thanks to Tim Cummings, Bob Pan, Shaheer Hussam, Pippa Mpunzwana, Najma Saleem, and Natalia Landron for helping me keep my sanity and maintain a semblance of a social life during graduate school. Thanks to my co-worker, roommate, and friend, Alexander König for helping keep a bit of balance in my life over the last year. Of course, thanks to my long term friends from Puerto Rico, St. Croix, and all over the US: Roberto Acevedo, Juan Carlos Martinez, Benjamin Reece, Joshua Gordon, Eric Hsieh, Josh Lapan, Angelie Peterson, Eric Gonzalez, and Delimar Perez. We may be far away at time but our friendship always seem to pick up right where we left off whenever we meet. Thanks to Bibiana Caballero for your love, patience, and understanding over the last few months putting together this thesis. You are amazing and I am honored to have you in my life!

Last but certainly not least, I want to thank my family - each and everyone of you - for your limitless love and support. Mom thanks for your hard work and dedication in the midst of all the challenges life has thrown your way. My sister, Yohmarie, and brother-in-law, Carlos, for always giving me a home away from home and giving me such an amazing niece! Abuela Amada and Abuelo Doel for being such loving grandparents and part-time (sometime full-time) parents. To all my aunts, uncles, and cousins, I am blessed to have you in my life.

You are all my "giants" and I could not be where I am today without all of you. Thank you!

Contents

List of Tables

List of Figures

Introduction

Ambulation, Quality of Life, and Disease

Ambulation crucial activity of daily living (Quinn et al., 2011, Collin et al., 1988). Being such a basic component of our everyday lives, most of us take little time to think about what life would be like if we were unable to walk. It is only when our own mobility or that of friends, relatives, or colleagues is affected that we notice the tremendous importance that walking plays in our lives.

Unfortunately, many diseases and injuries can affect an individuals' ability to walk independently. For example, in the US alone, there are approximately 800,000 new cases of stroke each year and over 30% of ischemic stroke survivors are unable to walk at six months without assistance (Lloyd-Jones et al., 2009). According to one study by the Christopher & Dana Reeve Foundation, it is estimated that approximately 1.9% of the U.S. population, or some 5,596,000 people, currently suffer from some form of paralysis - largely due to stroke (29%), spinal cord injury (23%), and multiple sclerosis (17%). Limb loss, resulting from trauma or amputation, is another major contributor to loss of ambulation. In the US alone, over 1.7 million people are estimated to have lost a limb (Ziegler-Graham et al., 2008).

The ability to walk independently is a major determinant of favorable survival prognosis post stroke (Chiu et al., 2012). As such, the goal of treatment, regardless of the underlying pathology should aim to restore an individual's ability to ambulate independently.

Restoration of Gait in Disease

Understanding Neural Function

Gait results from the coordinated activity of numerous components of the nervous system. The fields of neuroscience, neurophysiology, and neuroanatomy have yielded much insight into how individual components at the level of the brain (motor cortex, basal ganglia, and cerebellum), interact with modules within the spinal cord (central pattern generators, intra-spinal circuits, and alpha motor neurons), to

drive muscles and move the body. Also, much is known about how sensory information from muscles (from spindles and Golgi tendon organs), joints (mechanoreceptors), and vision are integrated to correct ongoing movements within the brain (within the cerebellum and sensory cortices). Much of this systems-level knowledge was derived from anatomical connectivity studies, lesion studies, and from ex-vivo and in-vivo physiology. At the same time, there have been tremendous advances in understanding neural function and the changes (plasticity) that occurs within single cells as a result of experience and changes in the local microenvironment. Orlovsky et al. (1999) and Kandel et al. (2000) provide detailed introductions regarding the neural control of locomotion.

We are at the cusp of beginning to understand how the information gathered across the various levels of motor system is represented and integrated by individual cells, groups of neurons, and across brain regions in real-time to results in coordinated movement. Understanding how changes in the body and the environment affect neural plasticity will be important for understanding that processes involved in task acquisition in health, and also how brain networks are reorganized after changes in the body (such as traumatic limb loss or spinal cord injury). In particular, understanding how information is represented within neural circuits and individual cells, and how this representation changes within experience and the properties of the environment will be informative for the development of prosthetics devices for patients where the underlying upstream neural systems are still intact.

Brain Machine Interfaces

Brain machine interfaces (BMIs) hold promise for the restoration of gait. Over the last 15 years there has been a surge in the number of successful applications of BMIs for the control of reaching (Chapin et al., 1999, Velliste et al., 2008, Black et al., 2003). Numerous investigators have recently begun to apply techniques to the lower extremity (Presacco et al., 2011, Fitzsimmons et al., 2009). Current approaches have suffer from major problems such as the constant need to recalibrate(Carmena, 2012). Additionally, in order to make BMI systems widely clinically viable, significant improvements in reliability (lifetime usability of the interface) and performance (achieving control and dexterity comparable to natural movements) need to be achieved (Orsborn et al., 2012). One main limitation of current approaches is based on the limited knowledge of how information about a task is represented by an ensembles of neurons. Researcher currently "bypass" this problem by treating the relationship between neural firing and variables of interest as a "black box" and using regression based methods to obtain linear predictors that can be used to decode movement variables in real-time (Carmena et al., 2003,

Presacco et al., 2011, Fitzsimmons et al., 2009, Black et al., 2003). Developing an understanding of information processing at the individual neuron and population level (see Moran and Schwartz (1999), Georgopoulos et al. (1986)) is likely to lead to insights about the control of locomotion in health and will allow for improved information extraction from neural ensembles. Deriving models of neural function that capture how task-relevant information is represented together with an understanding of how these representations change with time, experience, and pathology will help address the current limitations of BMI reliability, performance, and calibration.

Gait Rehabilitation

Until technologies are developed to allow restoration of damaged neural tissue back to its original state (the goal of stem cell research) or for lesion sites to be bypassed (e.g. using BMIs, see Hochberg et al. (2012)), physical therapy (which aims to restore function by establishing new motor-cortical connections among the remaining neurons) remains the most viable option for patients. In stroke, for example, 80% of the nearly 800,000 new stroke survivors each year require some sort of rehabilitation, and of these only 10% regain full function(Lloyd-Jones et al., 2009).

Functional recovery during rehabilitation is the result of learned compensatory strategies and the development of new motor cortical connections, each constituting forms of motor learning. Currently, a multitude of physical therapy paradigms are practiced throughout the country, each based on a variety of underlying theoretical principles (e.g. neurophysiologic, motor learning, orthopedic) or technologies (e.g. functional electrical stimulation (Marsolais and Kobetic, 1987, Peckham and Knutson, 2005, Yan et al., 2005, Subramanya et al., 2012), interactive robotic therapy(Veneman et al., 2007, Colombo et al., 2001, Reinkensmeyer et al., 2004, Banala et al., 2009)). Given the unfortunate lack of conclusive clinical evidence on how to best implement any one approach, even when two hospitals adopt the same paradigm for physical therapy, the actual implementation is likely to vary. Moreover, given the number of clinical assessment scales currently used to determine patient progress (Barthel Index (Collin and Wade, 1990), Fugl-Meyer scale(Fugl-Meyer AR, 1975), etc.), inter-rater and intra-rater variability with use of such scales, and the varied anatomy of pathologies such as stroke, it becomes nearly impossible to discern the specific benefit of any one physiotherapeutic approach versus another from the literature. This is exemplified by a recent meta-analysis (Pollock et al., 2007) which found that compared with placebo, any type of rehabilitation after stroke does better than none at all, but no one rehabilitation paradigm could be shown to be superior to any other in a statistically significant

manner. Thus, current physiotherapeutic strategies do have a significant benefit in the functional recovery of the patient, but current limitations do not allow us to understand how each does relative to one another or how to modify a single approach to achieve the best possible results for a given patient. It is likely that these limitations are the result of: 1) varied theory or application driven paradigms applied without uniform implementation or assessment of the rate of patient progress, and 2) varied clinical assessment scales each using distinct sets of surrogate variables to determine "patient recovery."

Motor Adaptation

Motor adaptation refers to the trial-by-trial alternation of motor commands in response to error feedback (Martin et al., 1996b), and has been extensively studied in the upper arm over the last 20 years utilizing common experimental paradigms, such as the Force Field Adaptation Paradigm (Shadmehr and Mussa-Ivaldi, 1994, Scheidt et al., 2000b). Under the hypothesis that long-term skill relearning during rehabilitation (termed motor learning) results from a series of short term motor adaptations, the relevance of motor adaptations within the context of rehabilitation becomes clear. Additionally, as Reisman and Bastian (2010) note, "adaptation allows us to determine whether the nervous system is still capable of a more normal pattern of movement." It is therefore not surprising that numerous researchers have begun to study motor adaptation in the lower extremity (Emken and Reinkensmeyer, 2005, Lam et al., 2006, Fortin et al., 2009, Reisman et al., 2007, Banala et al., 2009). Unfortunately, many of the approaches have been implemented on devices that are not commercially available and even in the case where devices have been comparable, the approaches have been varied. The end result is that the outcomes of these studies are quite difficult to compare.

Summary of Aims

This thesis aims to yield methods for improved lower extremity rehabilitation. We believe that improved patient outcomes will be achieved via the successful integration of knowledge about the underlying neural control of locomotion under a range of conditions and via the uniform characterization of the motor adaptations that result during gait retraining. More specifically, the aims of this thesis are detailed below.

Development tools for systematic analysis of neural function

Current approaches to BMI design treat the relationship between task-relevant variables and neural firing as a "black box." These methods have shown that BMIs hold great promise for the restoration of function in patients but performance, reliability, and calibration issues are likely to be minimized if more detailed models of neural information encoding are used. Over the last decade there has been a tremendous advance in the analytical tools available to neuroscientists to understand and model neural function. In particular, the Point Process - Generalized Linear Model (PPGLM) framework has been successfully applied to problems ranging from neuro-endocrine physiology to neural decoding. However, lack of availability of published PP-GLM algorithms together with problem-specific modifications required for their use, limit wide application of these techniques. In an effort to make existing PP-GLM methods more accessible to the neuroscience community, we have developed nSTAT – an open source neural spike train analysis toolbox for Matlab®. nSTAT allows for the systematic testing and analysis of point process models over a large number of neurons. It is our hope that developing an easy to use and open-source implementation will assist neurophysiologists in developing accurate models of neural function that will someday yield more robust and reliable BMI implementations.

Adaptation of neural dynamics of locomotion under changes in environmental conditions

To elucidate the neural mechanisms of locomotion, we studied in collaboration with Dr. Weiguo Song and Dr. Simon Giszter, how task relevant information (e.g. positions, velocities, and forces) modulate single unit neural activity from hindlimb/trunk region of the rat motor cortex during adaptations to robot-applied elastic loads and closed-loop brain-machine-interface (BMI) control during treadmill locomotion. Using the Point Process-Generalized Linear Model (PP-GLM) statistical framework we systematically tested parametric and non-parametric point process models of increased complexity for 573 individual neurons recorded over multiple days in six animals. The developed statistical model captures within gait-cycle modulation, load-specific modulation, and intrinsic neural dynamics.

Development of tools to assess motor adaptation during gait rehabilitation

We develop an extension of the Force Field Adaptation Paradigm, originally developed to quantitatively assess upper extremity motor adaptation, to the lower

extremity. The algorithm is implemented on the Lokomat (Hocoma HG) lower extremity gait orthosis and is currently being utilized to assess short-term motor adaptation in 40 healthy adult subjects (ClinicalTrials.gov NCT01361867). Establishing an understanding of how healthy adults' motor systems adapt to external perturbations will be important to understanding how the adaptive mechanisms involved in gait integrate information and how this process is altered by disease.

Thesis Outline

In Chapter 2, we introduce our open source neural spike train analysis toolbox (nSTAT), discuss the PP-GLM framework, and provide examples of how nSTAT can be used to address 5 common problems in neuroscience. In Chapter 3, we studied how task relevant information (e.g. positions, velocities, and forces) modulate single unit neural activity from hindlimb/trunk region of the rat motor cortex during adaptations to robot-applied elastic loads and closed-loop brain-machine-interface (BMI) control during treadmill locomotion. Using the Point Process-Generalized Linear Model (PP-GLM) statistical framework we systematically tested parametric and non-parametric point process models of increased complexity for 573 individual neurons recorded over multiple days in six animals. Lastly, in Chapter 4, we introduce our extension of the Force Field Adaptation Paradigm (FFAP) to the lower extremity. We describe our algorithm, its corresponding implementation within the Lokomat lower extremity gait orthosis, and perform some preliminary analysis from our ongoing clinical trial.

Acknowledgements

This work was supported by NIH F31NS058275 - "Automated and Adaptive Lower Extremity Neuro-Rehabilitation for Stroke" to Iahn Cajigas.

References

Banala, S., Kim, S.H., Agrawal, S., Scholz, J.. Robot Assisted Gait Training With Active Leg Exoskeleton (ALEX). Neural Systems and Rehabilitation Engineering, IEEE Transactions on 2009;17(1):2–8.

Black, M., Bienenstock, E., Donoghue, J.P., Serruya, M., Wu, W., Gao, Y.. Connecting brains with machines: the neural control of 2D cursor movement. In: Neural Engineering, 2003. Conference Proceedings. First International IEEE EMBS Conference on. 2003. p. 580–583.

Carmena, J.M.. Becoming Bionic. Spectrum, IEEE 2012;49(3):24–29.

Carmena, J.M., Lebedev, M.A., Crist, R.E., O'Doherty, J.E., Santucci, D.M., Dimitrov, D.F., Patil, P.G., Henriquez, C.S., Nicolelis, M.A.L.. Learning to control a brain-machine interface for reaching and grasping by primates. PLoS biology 2003;1(2):E42–E42.

Chapin, J.K., Moxon, K.A., Markowitz, R.S., Nicolelis, M.A.. Real-time control of a robot arm using simultaneously recorded neurons in the motor cortex. Nat Neurosci 1999;2(7):664–670.

Chiu, H.T., Wang, Y.H., Jeng, J.S., Chen, B.B., Pan, S.L.. Effect of Functional Status on Survival in Patients With Stroke: Is Independent Ambulation a Key Determinant? Archives of physical medicine and rehabilitation 2012;93(3):527–531.

Collin, C., Wade, D.. Assessing motor impairment after stroke: a pilot reliability study. J Neurol Neurosurg Psychiatry 1990;53(7):576–579.

Collin, C., Wade, D.T., Davies, S., Horne, V.. The Barthel ADL Index: A reliability study. Disability and Rehabilitation 1988;10(2):61–63.

Colombo, G., Wirz, M., Dietz, V.. Driven gait orthosis for improvement of locomotor training in paraplegic patients. Spinal Cord 2001;39(5):252–255.

Eden, U.T., Frank, L.M., Barbieri, R., Solo, V., Brown, E.N.. Dynamic analysis of neural encoding by point process adaptive filtering. Neural Comput 2004a;16(5):971–998.

Emken, J.L., Reinkensmeyer, D.J.. Robot-enhanced motor learning: accelerating internal model formation during locomotion by transient dynamic amplification. IEEE Trans Neural Syst Rehabil Eng 2005;13(1):33–39.

Fitzsimmons, N.A., Lebedev, M.A., Peikon, I.D., Nicolelis, M.A.L.. Extracting kinematic parameters for monkey bipedal walking from cortical neuronal ensemble activity. Front Integr Neurosci 2009;3:3.

Fortin, K., Blanchette, A., McFadyen, B.J., Bouyer, L.J.. Effects of walking in a force field for varying durations on aftereffects and on next day performance. Experimental brain research Experimentelle Hirnforschung Experimentation cerebrale 2009;199(2):145–155.

Fugl-Meyer AR, J.L.L.. The post stroke hemiplegic patient I. A method for evaluation of physical performance . Scandinavian Journal of Rehabilitation Medicine 1975;7(1):13–31.

Georgopoulos, A.P., Schwartz, A.B., Kettner, R.E.. Neuronal population coding of movement direction. Science (New York, NY 1986;233(4771):1416–1419.

Hochberg, L.R., Bacher, D., Jarosiewicz, B., Masse, N.Y., Simeral, J.D., Vogel, J., Haddadin, S., Liu, J., Cash, S.S., van der Smagt, P., Donoghue, J.P.. Reach and grasp by people with tetraplegia using a neurally controlled robotic arm. Nature 2012;485(7398):372–375.

Kandel, E.R., Schwartz, J.H., Jessell, T.M.. Principles of neural science. McGraw-Hill/Appleton & Lange, 2000.

Lam, T., Anderschitz, M., Dietz, V.. Contribution of Feedback and Feedforward Strategies to Locomotor Adaptations. J Neurophysiol 2006;95(2):766–773.

Lloyd-Jones, D., Adams, R., Carnethon, M., De Simone, G., Ferguson, T.B., Flegal, K., Ford, E., Furie, K., Go, A., Greenlund, K., Haase, N., Hailpern, S., Ho, M., Howard, V., Kissela, B., Kittner, S., Lackland, D., Lisabeth, L., Marelli, A., McDermott, M., Meigs, J., Mozaffarian, D., Nichol, G., O'Donnell, C., Roger, V., Rosamond, W., Sacco, R., Sorlie, P., Stafford, R., Steinberger, J., Thom, T., Wasserthiel-Smoller, S., Wong, N., Wylie-Rosett, J., Hong, Y., American Heart Association Statistics Committee and Stroke Statistics Subcommittee, . Heart disease and stroke statistics–2009 update: a report from the American Heart Association Statistics Committee and Stroke Statistics Subcommittee. Circulation 2009;119(3):480–486.

Marsolais, E.B., Kobetic, R.. Functional electrical stimulation for walking in paraplegia. J Bone Joint Surg Am 1987;69(5):728–733.

Martin, T.A., Keating, J.G., Goodkin, H.P., Bastian, A.J., Thach, W.T.. Throwing while looking through prisms. II. Specificity and storage of multiple gaze-throw calibrations. Brain 1996b;119 (Pt 4):1199–1211.

Moran, D.W., Schwartz, A.B.. Motor cortical representation of speed and direction during reaching. J Neurophysiol 1999;82(5):2676–2692.

Orlovsky, G.N., Deliagina, T.G., Grillner, S.. Neuronal Control of Locomotion: From Mollusc to Man (Oxford Neuroscience). 1st ed. Oxford University Press, USA, 1999.

Orsborn, A., Dangi, S., Moorman, H., Carmena, J.. Closed-Loop Decoder Adaptation on Intermediate Time-Scales Facilitates Rapid BMI Performance Improvements Independent of Decoder Initialization Conditions. Neural Systems and Rehabilitation Engineering, IEEE Transactions on 2012;PP(99):1–1.

Peckham, P.H.P., Knutson, J.S.J.. Functional electrical stimulation for neuromuscular applications. Annu Rev Biomed Eng 2005;7:327–360.

Pollock, A., Baer, G., Pomeroy, V., Langhorne, P.. Physiotherapy treatment approaches for the recovery of postural control and lower limb function following stroke. Cochrane database of systematic reviews (Online) 2007;(1):CD001920.

Presacco, A., Goodman, R., Forrester, L., Contreras-Vidal, J.L.. Neural decoding of treadmill walking from noninvasive electroencephalographic signals. J Neurophysiol 2011;106(4):1875–1887.

Quinn, T.J., McArthur, K., Ellis, G., Stott, D.J.. Functional assessment in older people. BMJ 2011;343(aug22 1):d4681–d4681.

Reinkensmeyer, D.J., Aoyagi, D., Emken, J.L., Galvez, J., Ichinose, W., Kerdanyan, G., Nessler, J., Maneekobkunwong, S., Timoszyk, B., Vallance, K., Weber, R., de Leon, R., Bobrow, J.E., Harkema, S.J., Wynne, J., Edgerton, V.. Robotic gait training: toward more natural movements and optimal training algorithms. Conference proceedings : Annual International Conference of the IEEE Engineering in Medicine and Biology Society IEEE Engineering in Medicine and Biology Society Conference 2004;7:4818–4821.

Reisman, D.S., Bastian, A.J.. Neurophysiologic and rehabilitation insights from the split-belt and other locomotor adaptation paradigms. Phys Ther 2010;.

Reisman, D.S., Wityk, R., Silver, K., Bastian, A.J.. Locomotor adaptation on a split-belt treadmill can improve walking symmetry post-stroke. Brain 2007;130(Pt 7):1861–1872.

Riener, R., Lunenburger, L., Jezernik, S., Anderschitz, M., Colombo, G., Dietz, V.. Patient-cooperative strategies for robot-aided treadmill training: first experimental results. IEEE Trans Neural Syst Rehabil Eng 2005;13(3):380–394.

Scheidt, R.A.R., Reinkensmeyer, D.J.D., Conditt, M.A.M., Rymer, W.Z.W., Mussa-Ivaldi, F.A.F.. Persistence of motor adaptation during constrained, multijoint, arm movements. J Neurophysiol 2000b;84(2):853–862.

Shadmehr, R., Mussa-Ivaldi, F.A.. Adaptive representation of dynamics during learning of a motor task. J Neurosci 1994;14(5 Pt 2):3208–3224.

Srinivasan, L., Eden, U.T., Mitter, S.K., Brown, E.N.. General-purpose filter design for neural prosthetic devices. J Neurophysiol 2007;98(4):2456–2475.

Subramanya, K.B.K., Kanakabettu, A.K.M.A., Mahadevappa, M.M.. Functional electrical stimulation for stoke rehabilitation. Med Hypotheses 2012;78(5):687–687.

Velliste, M.M., Perel, S.S., Spalding, M.C.M., Whitford, A.S.A., Schwartz, A.B.A.. Cortical control of a prosthetic arm for self-feeding. CORD Conference Proceedings 2008;453(7198):1098–1101.

Veneman, J.F., Kruidhof, R., Hekman, E.E.G., Ekkelenkamp, R., van Asseldonk, E.H., van der Kooij, H.. Design and evaluation of the LOPES exoskeleton robot for interactive gait rehabilitation. IEEE Trans Neural Syst Rehabil Eng 2007;15(3):379–386.

Yan, T., Hui-Chan, C.W.Y., Li, L.S.W.. Functional electrical stimulation improves motor recovery of the lower extremity and walking ability of subjects with first acute stroke: a randomized placebo-controlled trial. Stroke 2005;36(1):80–85.

Ziegler-Graham, K., MacKenzie, E.J., Ephraim, P.L., Travison, T.G., Brookmeyer, R.. Estimating the prevalence of limb loss in the United States: 2005 to 2050. Archives of physical medicine and rehabilitation 2008;89(3):422–429.

nSTAT: Open-Source Neural Spike Train Analysis Toolbox for Matlab

Abstract

Over the last decade there has been a tremendous advance in the analytical tools available to neuroscientists to understand and model neural function. In particular, the Point Process - Generalized Linear Model (PPGLM) framework has been successfully applied to problems ranging from neuro-endocrine physiology to neural decoding. However, lack of availability of published PP-GLM algorithms together with problem-specific modifications required for their use, limit wide application of these techniques. In an effort to make existing PP-GLM methods more accessible to the neuroscience community, we have developed nSTAT – an open source neural spike train analysis toolbox for Matlab®. nSTAT adopts an Object-Oriented Programming (OOP) approach to allow the user to easily manipulate data by performing operations on objects that have an intuitive connection to the experiment (spike trains, covariates, etc.), rather than by dealing with data in vector/matrix form. The algorithms implemented within nSTAT address a number of common problems including computation of peri-stimulus time histograms, quantification of the temporal response properties of neurons, and characterization of neural plasticity within and across trials. nSTAT provides a starting point for exploratory data analysis, allows for simple and systematic building and testing of point process models, and for decoding of stimulus variables based on point process models of neural function. By providing an open-source implementation, we hope to establish a platform that can be easily used, modified, and extended by the neuroscience community to address limitations of current techniques and to extend available techniques to more complex problems.

Introduction

Understanding how neurons represent information is a central problem in neuroscience. Whether it involves understanding how the concentration of a particular chemical present within the bath solution of an isolated neuron affects its spontaneous firing activity (Phillips et al., 2010) or how a collection of neurons encode arm movement information (Georgopoulos et al., 1986), the neurophysiologist aims to decipher how the individual or collective action potentials of neurons are correlated with the stimulus, condition, or task at hand. Due to the stereotypic all-or-none nature of action potentials, neural spiking activity can be represented as a stochastic point process, a time series that takes on the value 1 at the times of an action potential and is 0 otherwise (Daley and Vere-Jones, 1988). Point processes are completely characterized by their conditional intensity function (CIF), a generalization of the "rate" for a Poisson process (Daley and Vere-Jones, 1988). Many other common phenomena can be described as a point process ranging from geyser eruptions (Azzalini and Bowman, 1990) to data traffic within a computer network (Barbarossa et al., 1997).

Generalized Linear Models (GLMs) (McCullagh and Nelder, 1989), a flexible generalization of ordinary least squares regression, can be used in concert with point process models to yield a robust and efficient framework for estimating the conditional intensity function of a point process. This Point Process - Generalized Linear Model (PP-GLM) framework has been successfully applied to a broad range of problems including the study of cardiovascular physiology (Chen et al., 2011a, 2010c,d, 2009b, Brown and Barbieri, 2008, Chen et al., 2008, Barbieri and Brown, 2004, Barbieri et al., 2005a, Barbieri and Brown, 2006b,a), neuro-endocrine physiology (Brown et al., 2001a), neurophysiology (Frank et al., 2002, 2004, 2006, Eden et al., 2004b), and neural decoding (Barbieri et al., 2004b, 2008, Eden et al., 2004a, Srinivasan et al., 2006, 2007). Truccolo et al. (2005) provide a broad overview of the PP-GLM framework.

While much progress has been made in the development and application of PP-GLM methods within neuroscience, the use of these methods/algorithms typically requires in-depth knowledge of point process theory. Additionally, while there are widely available implementations for the estimation of GLMs within software packages such as Matlab® (The Mathworks, Natick, MA), S, or R programming languages, their use to analyze neural data requires problem specific modifications and the implementation of a number of non-trivial analysis routines. These adaptations require much work on the part of the experimentalist and detract from the goal of neural data analysis. These barriers are exacerbated by the fact that even when software implementations are made publicly available they vary greatly in the amount of documentation provided, the programming style used, and in the

problem-specific details.

Numerous investigators have successfully addressed common problems within neuroscience (such as spike sorting, data filtering, and spectral analysis) via the creation of freely available software toolboxes that encapsulate the implementation details from the user with the aim of allowing widespread adoption of these methods by the neuroscience community. Chronux (Bokil et al., 2010), FIND (previously MEA-Tools) (Meier et al., 2008, Egert et al., 2002), STAToolkit (Goldberg et al., 2009), and SPKtool (Liu et al., 2011) are a few examples of such tools. Chronux offers several routines for computing spectra and coherences for both point and continuous processes along with several general purpose routines for extracting specified segments from data, or binning spike time data with bins of a specified size. STAToolkit offers robust and well-documented implementations of a range of information-theoretic and entropy-based spike train analysis techniques. The FIND toolbox provides analysis tools to address a range of neural activity data, including discrete series of spike events, continuous time series and imaging data, along with solutions for the simulation of parallel stochastic point processes to model multi-channel spiking activity. SPKtool provides a broad range of tools for spike detection, feature extraction, spike sorting, and spike train analysis. However, a simple software interface to PP-GLM specific techniques is still lacking.

Fortunately, the method for systematic analysis of data within the PP-GLM framework is remarkably consistent and amenable to implementation as software toolbox. Broadly speaking there are two main types of analysis that can be performed: 1) encoding analysis and 2) decoding analysis. In encoding analysis, the experimenter seeks to build the simplest model that describes the firing properties of the neurons under consideration. This type of analysis requires comparison of the "goodness" of competing models while penalizing model complexity with the goal of arriving at the simplest model that describes the data. Decoding analysis, on the other hand, builds on prior knowledge of neural function (such as could be gained from encoding analysis) to estimate the value of stimuli responsible for the neural firing activity being observed. An example of this type of analysis would aim to estimate arm movement velocity given the population firing activity of a collection of M1 neurons and a model of their firing properties such as that developed by Moran and Schwartz (1999).

We leverage the consistency of the data analysis process within the PP-GLM framework in the design of our neural spike train analysis toolbox (nSTAT). Our object-oriented software implementation incorporates knowledge of the standard encoding and decoding approaches together with knowledge of the common elements present in most neuroscience experiments (e.g. neural spike trains, covariates, events, and trials) to develop code that can be used across a broad range of problems with few changes. Object-oriented programming (OOP) represents an at-

tempt to make programs more closely model the way people think about and deal with the world. By adopting an OOP approach for the software development within nSTAT we hope to allow the user to easily manipulate data by performing operations on objects that have an intuitive connection to the experiment and hypothesis at hand, rather than by dealing with raw data in matrix/vector form. Additionally, by building the toolbox for MATLAB®, we make sure that users can easily transfer their data and results from nSTAT to other freely or commercially available software packages, and develop their own extensions for nSTAT with relative ease.

The algorithms implemented within nSTAT address a number of problems of interest to the neuroscience community including computation of peri-stimulus time histograms, quantification of the temporal response properties of neurons (e.g. refractory period, bursting activity, etc.), characterization of neural plasticity within and across trials, and decoding of stimuli based on models of neural function (which can be pre-specified or estimated using the encoding methods in the toolbox). It should be noted that while all of the examples presented in the paper focus on the PP-GLM framework, nSTAT contains methods for analyzing spike trains when they are represented by their firing rate and treated as a Gaussian time-series instead of a point process. These include time-series methods such as Kalman Filtering (Kalman, 1960a), frequency domain methods like multi-taper spectral estimation (Thomson, 1982), and mixed time-frequency domain methods such as the spectrogram (Cohen and Lee, 1990, Boashash, 1992a). For brevity, and because these methods are also available in other toolboxes, we do not discuss these elements of the toolbox herein.

This paper is organized as follows: Section summarizes the general theory of point processes and generalized linear models as it applies to our implementation. We include brief descriptions of some of the algorithms present in nSTAT to establish consistent notation across algorithms developed by distinct authors. Section describes the software classes that make up nSTAT, the relationships among classes, and relevant class methods and properties. Section describes five examples that highlight common problems addressed using the PP-GLM framework and how they can be analyzed using nSTAT. Lastly, results for each of the different examples are summarized in Section . nSTAT is available for download at *http://www.neurostat.mit.edu/nstat/*. All examples described herein (including data, figures, and code) are contained within the toolbox help files. The software documentation also includes descriptions and examples of the time-series methods not discussed herein.

Material and Methods

Summary of the PP-GLM Framework

In this section, we describe the PP-GLM framework and describe several model selection and goodness of fit techniques that can be applied within the framework to select between competing hypotheses or between models of varying complexity. The peri-stimulus time histogram (PSTH) and its PP-GLM analogue, the GLM-PSTH, are then presented together with extensions of the GLM-PSTH that allow for estimation of both within-trial and across-trial neural dynamics (SS-GLM). We then discuss how point process models can be used in decoding applications, where neural firing information is used to estimate a driving stimulus.

Point Process Theory

Due to the stereotyped all-or-none nature of action potentials or spikes, neural spiking activity can be represented as a stochastic point process, a time series that takes on the value 1 at the time of an action potential and is 0 otherwise. A point process is completely characterized by its conditional intensity function (CIF) (Daley and Vere-Jones, 1988) defined as

$$\lambda(t|H_t) \triangleq \lim_{\Delta \to 0} \frac{P(N(t+\Delta) - N(t) = 1 \mid H_t)}{\Delta} \tag{2.2}$$

where H_t is all the history information from 0 up to time t and $N(t)$ is a counting process denoting the sum of all spike events up to time t. For any finite Δ, the product $\lambda(t|H_t)\Delta$ is approximately equal to the probability of a single spike in the interval $(t, t+\Delta]$ given the firing history up to time t. The conditional intensity function can be considered a generalization of the "rate" for a homogeneous Poisson process.

If the observation interval is partitioned into $\{t_j\}_{j=0}^{J}$ and individual time steps are denoted by $\Delta t_j = t_j - t_{j-1}$, we can refer to each variable by its value within the time step. We denote $N_j = N(t_j)$ and refer to $\Delta N_j = N_j - N_{j-1}$ as the spike indicator function for the neuron at time t_j. If Δt_j is sufficiently small, the probability of more than one spike occurring in this interval is negligible, and ΔN_j takes on the value 0 if there is no spike in $(t_{j-1}, t_j]$ and 1 if there is a spike. In cases where fine temporal resolution of the count process, $N(t)$, is not required we define $\Delta N(t_A, t_B)$ to equal the total number of spikes observed in the interval $(t_A, t_B]$.

Generalized Linear Models

The Generalized Linear Model (GLM) framework is a flexible generalization of ordinary least squares regression developed byMcCullagh and Nelder (1989) as a way of unifying various statistical models (including linear, logistic, and Poisson regressions) under one common framework that allowed efficient maximum likelihood parameter estimation. If the conditional intensity function is modeled as a member of the exponential family (i.e. the family of distributions covered by GLMs), we have an efficient algorithm for estimating CIF model parameters. Additionally, this approach will allow us to effectively select between competing models via the likelihood-criteria described below. In particular, we will use two main types of GLMs for the conditional intensity functions herein:

1) Poisson regression models where we write $\log\left(\lambda\left(t_j|H_{t_j}\right)\Delta\right)$ as a linear function of relevant covariates, e.g.

$$\log\left(\lambda\left(t_j|H_{t_j}\right)\Delta\right) = x_j^T\beta \iff \lambda\left(t_j|H_{t_j}\right)\Delta = \exp\left(x_j^T\beta\right) \tag{2.3}$$

and 2) Binomial regression models where we write the inverse of the logistic function, $\text{logit}\left(\lambda\left(t|H_t\right)\Delta\right)$, as a linear function of covariates, e.g.

$$\text{logit}\left(\lambda\left(t_j|H_{t_j}\right)\Delta\right) = x_j^T\beta \iff \lambda\left(t_j|H_{t_j}\right)\Delta = \frac{\exp\left(x_j^T\beta\right)}{1+\exp\left(x_j^T\beta\right)} \tag{2.4}$$

where x_j^T is the j^{th} row of the design matrix X and β is the vector of model parameters to be estimated. The spike indicator function, ΔN_j, is taken as the observation, termed y_j, and is modeled either as a Poisson or Binomial random variable. That is $y_j = \Delta N_j \sim exp\left(x_j^T\beta\right)$ or $y_j \sim \frac{\exp(x_j^T\beta)}{1+\exp(x_j^T\beta)}$.

Model Selection

Goodness of fit measures currently implemented in nSTAT include the time rescaling theorem for point processes (Brown et al., 2002), Akaike's information criteria (AIC) (Akaike, 1973), and Bayesian information criteria (BIC) (Schwarz, 1978). Briefly, the time rescaling theorem states that given the true conditional intensity function of a point process, λ, and a sequence of spike times $0 < t_1 < t_2 < \ldots < t_s < \ldots < t_S < T$, the rescaled spike times defined as

$$u_s = 1 - exp\left(\int_{t_{s-1}}^{t_s} \lambda(\tau|H_\tau)\mathrm{d}\tau\right) \tag{2.5}$$

$s = 1, ..., S$ are independent, identically distributed, uniform random variables on the interval $(0,1)$. To use the time-rescaling theorem to test the model goodness of fit, one can apply Equation 2.5 to each candidate model, λ^i, to obtain a set of candidate rescaled spike times u_s^i that can then be tested for independence and their closeness (to be made precise below) to an uniform distribution.

The Kolmogorov-Smirnov (K-S) test can be used to compare how close the empirical distribution of rescaled spike times, u_s's, are to a reference uniform distribution on the interval $(0,1)$. The visual representation of this test, termed a K-S plot (Truccolo et al., 2005, Brown et al., 2002), together with corresponding confidence intervals (Johnson and Kotz, 1970) allows for comparison of multiple models simultaneously. If candidate model is correct, the points on the K-S plot should lie on a 45° line (Johnson and Kotz, 1970). The K-S statistic is the largest deviation from the 45° line. Application of the time-rescaling theorem to sampled data produces some artifacts within K-S plots since the actual spike times could have occurred anywhere within the finite-sized time bins. These artifacts are addressed within nSTAT using the discrete time rescaling theorem (Haslinger et al., 2010).

Independence of the rescaled spike times can be assessed by plotting u_{s+1}^i vs. u_s^i (Truccolo et al., 2005). In this case, a correlation coefficient statistically different from zero casts doubt on the independence of the rescaled spike times. This test is equivalent to determining if the lag-1 coefficient of the auto-correlation function for the u_j^i's is statistically different from zero. A stronger test for independence uses the fact that uncorrelated Gaussian random variables are also independent. If the u_s^i's are uniform random variables on the interval $(0,1)$, then

$$x_s^i = \Phi^{-1}\left(u_s^i\right) \tag{2.6}$$

where $\Phi^{-1}(\cdot)$ is the inverse of the standard normal distribution cumulative distribution function (CDF), will be normally distributed with zero mean and unit variance. Significant non-zero coefficients of the auto-correlation function of the x_s^i's at non-zero lags cast doubt on the independence of the rescaled spike times (Truccolo et al., 2005). The 95% confidence interval for the non-zero lag coefficients of the auto-correlation function is $\pm 1.96/\sqrt{n}$ where n is the total number of rescaled spike times.

Goodness of fit can also be assessed by examining the structure of the point process model residual (Andersen, 1997, Truccolo et al., 2005) defined over non-overlapping moving time windows of size B as

$$M_j^i = M(t_j) = \sum_{n=j-B}^{j} \Delta N(t_n) - \int_{t_j-B}^{t_j} \lambda^i\left(\tau | H_\tau, \hat{\theta}\right) \mathrm{d}\tau \tag{2.7}$$

for $j-B \geq 1$. Strong correlations between covariates absent from the model for λ^i and M_j^i are indicative of potentially important un-modeled effects.

The AIC, BIC, rescaled spike times, and the point process residuals are automatically computed within the nSTAT **Analysis** class for each candidate model, λ^i, and stored within the returned **FitResult** object (see Section for more details). The **FitResult** method *plotResults* displays the K-S plot, the plot of u_{s+1}^i vs. u_s^i and corresponding correlation coefficient, the auto-correlation function of the x_s^i's, and the point process residual for each of the candidate λ^i's.

Simulating Point Processes

Validation and testing of new algorithms requires generating spiking activity according to know prior behavior. Given an integrable conditional intensity function $\lambda(t|H_t)$ for $0 \leq t \leq T$, a realization of the point process compatible with this CIF can be generated via time rescaling (Brown et al., 2002) as follows:

1. Set $t_0 = 0$; Set $s = 1$.
2. Draw z_s an exponential random variable with mean 1.
3. Find t_s as the solution to $z_s = \int_{t_{s-1}}^{t_s} \lambda(\tau|H_\tau)\mathrm{d}\tau$.
4. If $t_s > T$, then stop.
5. $s = s+1$
6. Go to 2.

In instances where the CIF is independent of history (e.g. a homogenous or inhomogenous Poisson process), the more computationally efficient point process thinning algorithm (Lewis and Shedler, 1978, Ogata, 1981) can be used. The nSTAT **CIF** class contains static methods (e.g. *CIF.simulateCIF, CIF.simulateCIFByThinning, and CIF.simulateCIFByThinningFromLambda*) to generate a realizations of a point process based on either time rescaling or the point process thinning algorithm.

PSTH and the GLM Framework

In neurophysiology, the peri-stimulus time histogram and post-stimulus time histogram, both abbreviated PSTH or PST histogram, are histograms of the times at which neurons fire. These histograms are used to visualize the rate and timing of neuronal spike discharges in relation to an external stimulus or event. To make a PSTH, a spike train recorded from a single neuron is aligned with the onset, or a fixed phase point, of an identical repeatedly presented stimulus. The aligned

sequences are superimposed in time and then combined to construct a histogram (Gerstein and Kiang, 1960, Palm et al., 1988).

According to Czanner et al. (2008), the PSTH is a special case of the conditional intensity function defined by the following GLM

$$\log\left(\lambda\left(k,n\Delta|\theta\right)\Delta\right)=\sum_{r=1}^{R}\theta_{r}g_{r}\left(n\Delta\right) \tag{2.8}$$

for $k=1,...,K$ and $n=1,...,N$. Here k and n are the trial number and bin within a trial respectively, and

$$g_{r}\left(n\Delta\right)=\begin{cases}1 & \text{if } n=(r-1)NR^{-1}+1,...,rNR^{-1}\\ 0 & \text{otherwise}\end{cases} \tag{2.9}$$

are the unit pulse functions in the observation interval $(0,T]$ (equivalently $[1,N\Delta]$). This conditional intensity function is the same for all trials $k=1,..,K$. Note that since there are R unit pulse functions over the N observed samples, the width of each unit pulse function is NR^{-1} . For the bin in which $g_{r}\left(n\Delta\right)=1$, the spiking activity obeys a homogenous Poisson process with mean rate $\exp\left(\theta_{r}\right)/\Delta$, and since the basis functions in Equation 2.9 are orthogonal, the values $\exp\left(\theta_{r}\right)/\Delta$ $r=1,...,R$ can be estimated independently of each other. The maximum-likelihood estimate of $\exp\left(\theta_{r}\right)/\Delta$ is the number of spikes that occur in the bin in which $g_{r}\left(n\Delta\right)=1$, summed across all trials, and divided by the number of trials and the bin width (e.g. equal to the value of the PSTH). Within nSTAT, the PSTH and the GLM-PSTH can be computed for any collection of neural spike trains (represented by the class **nstColl**) by specifying the bin width Δ. The GLM-PSTH routine (*psthGLM* method) also allows for the estimation of firing history effect of the same form as described in Section below.

State Space GLM Framework

The standard PSTH treats each trial as independent to produce an estimate of the firing rate. In many experiments it is of interest to not only capture the dominant variation in firing rates within a trial, but also to examine changes that might be occurring from one trial to the next (for example to examine neural plasticity or learning). Czanner et al. (2008) formulated the state-space generalized linear model (SS-GLM) framework to allow for this type of analysis. Briefly the SS-GLM framework proposes that the neural conditional intensity function be modeled as

$$\log\left(\lambda\left(k,n\Delta|\theta\right)\Delta\right)=\sum_{r=1}^{R}\theta_{k,r}g_{r}\left(n\Delta\right)+\sum_{j=1}^{J}\gamma_{j}\Delta N_{k}\left(t_{n}-t_{j-1},t_{n}-t_{j}\right) \tag{2.10}$$

where k is the current trial index and $\Delta N_k(t_A, t_B)$ equals the total number of spikes observed in the interval $(t_A, t_B]$ of the k^{th} trial. The stochastic trial-to-trial dependence between the parameters $\theta_k = \begin{bmatrix} \theta_{k,1} & \dots & \theta_{k,r} & \dots & \theta_{k,R} \end{bmatrix}$ is described by the random walk model

$$\theta_k = \theta_{k-1} + \varepsilon_k \tag{2.11}$$

for $k = 1, \dots, K$, where K is the total number of trials, ε_k is an R-dimensional Gaussian random vector with mean 0 and unknown covariance matrix Σ. The initial vector θ_0 is also assumed to be unknown. Because the parameters θ_k and γ_j of the GLM and the covariance parameter, Σ, of the random walk model are unknown, an iterative Expectation-Maximization algorithm (Dempster et al., 1977) is employed to estimate them.

The expected number of spikes in trial k within the time interval $[t_1, t_2]$ can be computed as

$$\Lambda_k(t_1, t_2) = \int_{t_1}^{t_2} \lambda(k, \tau | \theta_k, \gamma, H_{k,\tau}) \, \mathrm{d}\tau \tag{2.12}$$

and used to define spike rate function on the interval $[t_1, t_2]$ as

$$(t_2 - t_1)^{-1} \Lambda_k(t_1, t_2) = (t_2 - t_1)^{-1} \int_{t_1}^{t_2} \lambda(k, \tau | \theta_k, \gamma, H_{k,\tau}) \, \mathrm{d}\tau \tag{2.13}$$

The corresponding maximum likelihood estimates of the expected number of spikes and the spike rate function are obtained by evaluating Equations 2.12 and 2.13 with the estimated conditional intensity function. Confidence intervals can be constructed via the Monte Carlo methods described by Czanner et al. (2008). Statistical comparisons of the spike rate function between trials can be performed in order to examine experience dependent changes or learning across trials. In particular, for a given interval $[t_1, t_2]$ and trials m and k we can compute the maximum-likelihood estimates of Equation 2.13 and use Monte Carlo methods to compute

$$\Pr\left[(t_2 - t_1)^{-1} \hat{\Lambda}_m(t_1, t_2) > (t_2 - t_1)^{-1} \hat{\Lambda}_k(t_1, t_2)\right] \tag{2.14}$$

for any $k = 1, \dots, K-1$ and $m > k$. The smallest m such that probability in Equation 2.14 is greater than or equal to 95% is denoted as the learning trial with respect to trial k (i.e. the first trial where the spike rate function in the time interval $[t_1, t_2]$ is significantly different than the spike rate function in trial k).

The SSGLM routine is implemented by the **nstColl** class and requires specification of the number of $J+1$ time points ($[t_0, t_1, \dots, t_J]$) that are used to construct

J time windows of prior spiking activity, along with the number of within-trial bins, R, to be used. The routine returns estimates of θ_k for $k = 1,...,K$, Σ, and $\gamma = [\gamma_1,...,\gamma_J]$.

Point Process Adaptive Filter

In some situations, one has prior knowledge of the form of the conditional intensity function, $\lambda^c(t|x(t),\theta,H_t)$ for $c = 1,...,C$, where C is the number of individual neurons being observed, $x(t)$ is a vector of stimuli/covariates of interest, θ is a vector of parameters (typically obtained via GLM), and H_t is all of the relevant history up to time t. The decoding problem is then, given a collection of CIFs, to estimate the stimuli/covariates $x(t) = \left[\begin{array}{ccc} x_1(t) & ... & x_N(t) \end{array}\right]^T$ based on the firing activity of the ensemble $\Delta N^{1:C}(t)$. It is customary to discretize time and adopt the notation $x_k = x(t)|_{t=kT}$. We denote the spiking activity in the k^{th} time step by the vector $\Delta N_k^{1:C} = \left[\begin{array}{cccc} \Delta N_k^1 & \Delta N_k^2 & ... & \Delta N_k^C \end{array}\right]^T$ of binned spike counts. The c^{th} element of $\Delta N_k^{1:C}$ contains the total number of of spikes generated by the c^{th} neuron in the k^{th} time step. Spike history is represented by $H_k = \left[\begin{array}{cccc} \Delta N_1^{1:C} & \Delta N_2^{1:C} & ... & \Delta N_{k-1}^{1:C} \end{array}\right]$.

The system of equations for the state (stimuli) vector are defined as

$$x_{k+1} = A_k x_k + \omega_k$$

where A_k is the state transition matrix and ω_k is a zero mean Gaussian random vector with covariance Q_k. The effect of the stimuli is only observed via the firing of each of the individual cells, i.e.,

$$p(\Delta N_k^c|x_k,H_k) \approx \lambda_k^c \Delta \tag{2.15}$$

for $c = 1,...,C$, where $p\left(\Delta N_k^c|x_k,H_k\right)$ denotes the conditional probability distribution function of a spike in the k^{th} time bin by the c^{th} cell conditioned on the current stimulus, x_k, and history. Decoding is then equivalent to estimating the posterior density

$$p\left(x_k|\Delta N_k^{1:C},H_k\right) = \frac{p\left(\Delta N_k^{1:C}|x_k,H_k\right)p\left(x_k|H_k\right)}{p\left(\Delta N_k^{1:C}|H_k\right)} \tag{2.16}$$

Eden et al. (2004a) proposed a Gaussian approximation to this posterior and demonstrated that the recursive estimates for the stimulus mean and covariance at time k are given by the point process adaptive filter (PPAF) equations

Prediction:

$$x_{k+1|k} = A_k x_{k|k} \tag{2.17}$$

$$W_{k+1|k} = A_k W_{k|k} A_k^T + Q_k \tag{2.18}$$

Update:

$$(W_{k|k})^{-1} = (W_{k|k-1})^{-1} - \sum_{c=1}^{C} \left(\frac{\partial}{\partial x_k} \left[(\frac{\partial \log(\lambda_k^c \Delta)}{\partial x_k})^T (\Delta N_k^c - \lambda_k^c \Delta) \right]_{x_k = x_{k|k-1}} \right) \tag{2.19}$$

$$x_{k|k} = x_{k|k-1} + W_{k|k} \sum_{c=1}^{C} \left((\frac{\partial \log(\lambda_k^c \Delta)}{\partial x_k})^T (\Delta N_k^c - \lambda_k^c \Delta) \right) \tag{2.20}$$

If the final state x_K is known (e.g. reaching to a known target), the point process adaptive filter can be modified according to Srinivasan et al. (2006) so that the final state estimate matches the known final state. Decoding of both discrete and continuous states, s_k and x_k respectively, from point process observations termed the Point Process Hybrid Filter (PPHF) was derived bySrinivasan et al. (2007). The equations for the PPHF are not reproduced here for brevity but are implemented within nSTAT.

The PPAF is implemented by the *PPDecodeFilter* and *PPDecodeFilterLinear* methods of the **DecodingAlgorithms** class. It requires the specification of the state transition matrix, A_k, the covariance matrix, Q_k, a description of the CIF for each cell, the observed firing activity, $\Delta N_k^{1:C}$ for $k = 1, ..., K$, and optionally target specific information. The method returns estimates of states $x_{k|k}$ and $x_{k+1|k}$, and the corresponding covariances $W_{k|k}$ and $W_{k+1|k}$. The PPHF is implemented by the *PPHybridFilter* and *PPHybridFilterLinear* methods of the **DecodingAlgorithms** class. It requires the specification of the matrices, $A_k^{(s_k=i)}$ and $Q_k^{(s_k=i)}$ for each possible value of the the discrete state, s_k, a description of the CIF for each cell under for each value of s_k, the observed firing activity, $\Delta N_k^{1:C}$ for $k = 1, ..., K$, a matrix of state transition probabilities $p(s_k|s_{k-1})$, and optionally target specific information. The method returns estimates of $s_{k|k}$, $x_{k|k}$ and $W_{k|k}$.

Object Oriented Program Structure

Object oriented programming (OOP) is a programming language model that is organized around "objects" – data structures consisting of data fields and methods. Objects are specified by their class definitions which specify the fundamental properties of the object and how the data within the object can be manipulated. This programming approach allows for inheritance - the notion that a more sophisticated class can reuse the properties and methods of elementary classes. The

PP-GLM framework consists of some fundamental elements that lend themselves directly into this model. While the specific applications/experiments might range widely, encoding and decoding analysis within the framework always consists of the same basic elements: spike trains, covariates, trials, and events (within trials). The benefits of this approach are

1. Data Encapsulation: Once an object is created, it can be manipulated only in the ways pre-specified by the class. The helps maintain the consistency of the data as the object is manipulated during the analysis process. This encapsulation is essential for complex problems where specific implementation details might become overwhelming. For example, when manipulating an object of the **Trial** class, users need not focus on the implementation details of spike trains (class **nspikeTrain**), covariates (class **Covariate**), and events (class **Event**), but can rather perform operations on trials as a whole via the methods provided by the **Trial** class.

2. Method access: Each class has methods that are relevant to it and the type of information that it contains. This helps users know what kinds of operations can be performed on different types of objects.

3. Code reuse: Due to inheritance, methods need not be implemented for each new object. This leads to organization of methods across classes and simplified code maintenance. Additionally, this property can allow for decrease programming complexity. For example, consider the computation of the time rescaling theorem. Suppose we have a collection of spike times, $0 < t_1 < t_2 < ... < t_s < ... < t_S < T$, represented as a vector called spikeTimes, and a conditional intensity function, $\lambda(t|H_t)$, represented as a **SignalObj** called lambda. The rescaled spike times, u_s, from the time rescaling theorem are computed by the following code:

```
%%  Time Rescaling Theorem
  t_s = spikeTimes(2:end);        % t_1,..., t_S
  t_sMinus1 = spikeTimes(1:end-1); % 0,t_1,...,t_{S-1}
  lambdaInt = lambda.integral;
  % lambdaInt(t) = integral from 0 to t of lambda(t)
  z_s=lambdaInt.getValueAt(t_s) - ...
      lambdaInt.getValueAt(t_sMinus1);
  u_s=1-exp(z_s);
```

where the *integral* method of class **SignalObj** returns a **SignalObj** object. Since lambdaInt is an object of class **SignalObj** it has a *getValueAt* method

that can be used to obtain the value of the integral at each of the spike times in the vectors *t_s* and *t_sMinus1*.

Figure 2.2 highlights how the standard PP-GLM workflow is related to the nSTAT classes, and how a particular problem can be analyzed using nSTAT. In this case, the included code corresponds to the first portion of Example 1. Figure 2.3 uses unified modeling language (UML) formalism (Booch et al., 2005, Bézivin and Muller, 1999) to show how the classes that make up nSTAT are related.

nSTAT Classes

1. **SignalObj** - a class representing a signal abstraction. In general, a signal is any time-varying or spatial-varying quantity (e.g. a time-series). This implementation of the signal abstraction consists of the pair $(t, x(t))$, where t is a one-dimensional indexing variable (time, space, etc.) and $x(t)$ is the corresponding data specified at each value of the indexing variable. A signal can be multivariate if at every value of the indexing variable, a vector of data is specified (the size of this vector determines the dimension of the signal). **SignalObj**'s have a number of methods that facilitate the manipulation of their data such as maxima, minima, frequency spectra, etc. **SignalObj**'s can be integrated, differentiated, filtered, shifted, scaled, added, and subtracted among other operations and the result of these operations is also a **SignalObj**.

2. **Covariate** - a class representing the explanatory variables used in the construction of conditional intensity function models within the PP-GLM framework. **Covariates** are **SignalObj**'s with mean μ and a standard deviation σ.

3. **CovColl** - a container for multiple **Covariate** objects. This container ensures that all the covariates have the same sampling rate, start time, and end time. **CovColl** has a *covMask* field that allows some **Covariates** to be masked or effectively hidden. Additionally, the **CovColl** can be converted to a matrix by the *dataToMatrix* method. Only covariates that are currently selected in the *covMask* field are used in the creation of the matrix representation of the **CovColl**. This matrix representation is used to generate part of the design matrix, X , for GLM analysis (see Equations 2.3 and 2.4).

4. **nspikeTrain** - a neural spike train object consists of a set of spike times. The spike train can be represented as a signal of class **SignalObj** with a particular sampling rate. If the bin size resulting from the specified sample rate is larger than the difference between any two spike times, the neural spike train will

not have a binary **SignalObj** representation. Effectively, specification of sample rate for an object of class **nspikeTrain** specifies how the spike train will be binned.

5. **nstColl** -a container for objects of class **nspikeTrain** that ensures that all the contained spike trains have the same start time, end time, and sample rate. Similar to **covColl**, **nstColl** has a *neuronMask* field that allows selection of a subset of all the spike trains in the collection. **nstColl** includes methods for the generation of inter-spike interval (ISI) histograms and peri-stimulus time histograms (PSTH). The method dataToMatrix can be used to obtain a matrix representation of the spike trains that is used by the **Analysis** class to obtain the observations, $y_j = \Delta N(t_j)$, used in GLM analysis.

6. **Event** - consists of a collection of pairs of times and labels, (t_k, ℓ_k), that are used to identify important points within **Trial** objects.

7. **History** - defines a collection of time window edges/boundaries within which the spiking activity of a **nspikeTrain** is to be analyzed. For example the vector of window times, $[0, 0.002, 0.01]$, specifies one window from 0 to 2ms and another from 2ms to 10ms. Calling the *computeHistory* method on a spike train using the previously mentioned window times would yield a **Covariate** object with two dimensions. The first dimension would be a time-series that at time t has the value of the summed spiking activity in the interval $[t-2, t)$ and the second a time-series that at time t equals the sum of the spiking activity in the interval $[t-10, t-2)$.

8. **Trial** - Consists of **covColl**, **nstColl**, and **Event** objects and implements the abstraction of an experimental trial by keeping all of the corresponding data together. The trial data can be visualized using the *plot* method. This class ensures that the spike trains and covariates are all properly sampled and aligned in time.

9. **TrialConfig** - A class that specifies the manner in which a **Trial** object should be analyzed. Each **TrialConfig** object specifies the name of the covariates to be included in the analysis, the sample rate to be used for all of the covariates and spike trains, the history windows to be used, and the time window for analysis (i.e. can perform analysis on a subset of all the trial data).

10. **ConfColl** - A container for multiple **TrialConfig** objects.

11. **Analysis** - A collection of static methods for analyzing a **Trial** according to the specifications included in a **ConfigColl**. Given a **Trial** and **ConfigColl**

object, the method *RunAnalysisForAllNeurons* returns a **FitResult** object for each spike train in the trial. Each **FitResult** object contains the results of all the different configurations specified in the **ConfigColl** as applied to each spike train.

12. **FitResult** - Contains the GLM coefficients (with corresponding standard errors), AIC, BIC, KS statistics, rescaled spike times, and point process residual for each of the specified configurations in **ConfigColl**. Includes methods to visualize the results of each of the different configurations to assist in the model selection process. For example, the *plotResults* method overlays the KS plot, the autocorrelation function of the u_s^i's, the lag-1 correlation coefficient of the u_s^i's, the GLM fit coefficients with 95% confidence intervals, and the point process residual for each of the models specified in the **ConfigColl**.

13. **FitResSummary** - given a collection of **FitResult** objects (one for each neuron, each containing the results of multiple regressions), computes summary statistics across all neurons and all configurations in the **ConfigColl**. This class allows visualization of commonalities in the data across multiple neurons.

14. **CIF** - Conditional Intensity Function abstraction. Allows a conditional intensity function to be defined symbolically. Symbolic differentiation of the CIF can be performed to compute the Jacobian and Hessian of $\log(\lambda^c(t|x(t),\theta,H_t)\Delta)$ and $\lambda^c(t|x(t),\theta,H_t)\Delta$ required for computation within the point process adaptive filter or the point process hybrid filter. The **CIF** class also contains static functions that allow simulating point processes based on specification of the conditional intensity function via time rescaling or the point process thinning algorithm.

15. **DecodingAlgorithms** - Includes static methods that implement the point process adaptive filter (PPAF), the state-space GLM (SSGLM) filter, and the point process hybrid filter (PPHF) among others. In particular, this class also implements non-point process algorithms such as the Kalman Filter (Kalman, 1960a) and the Kalman Smoother (Rauch et al., 1965).

Examples

Example 1 - Homogeneous/Inhomogenous Poisson Models - The Miniature Excitatory Post-Synaptic Current

Miniature excitatory post-synaptic currents (mEPSCs) have become a primary measure of synaptic modification during development, plasticity, and disease. These

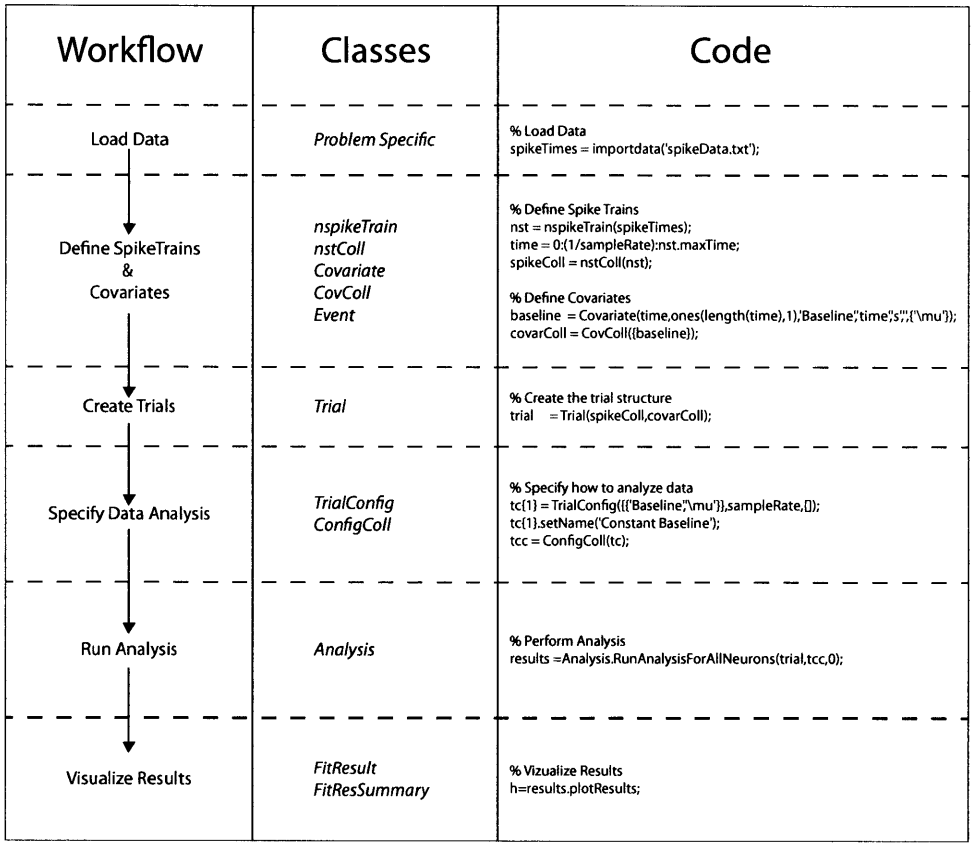

Figure 2.2: **Visual overview of the data analysis workflow, relevant classes, and code using nSTAT.** This particular example shows the typical workflow in the testing of candidate conditional intensity functions. For brevity, the workflow for decoding stimuli using the Point Process Adaptive Filter or the Hybrid Point Process Filter is not shown (see the Matlab help files for these examples for the corresponding code).

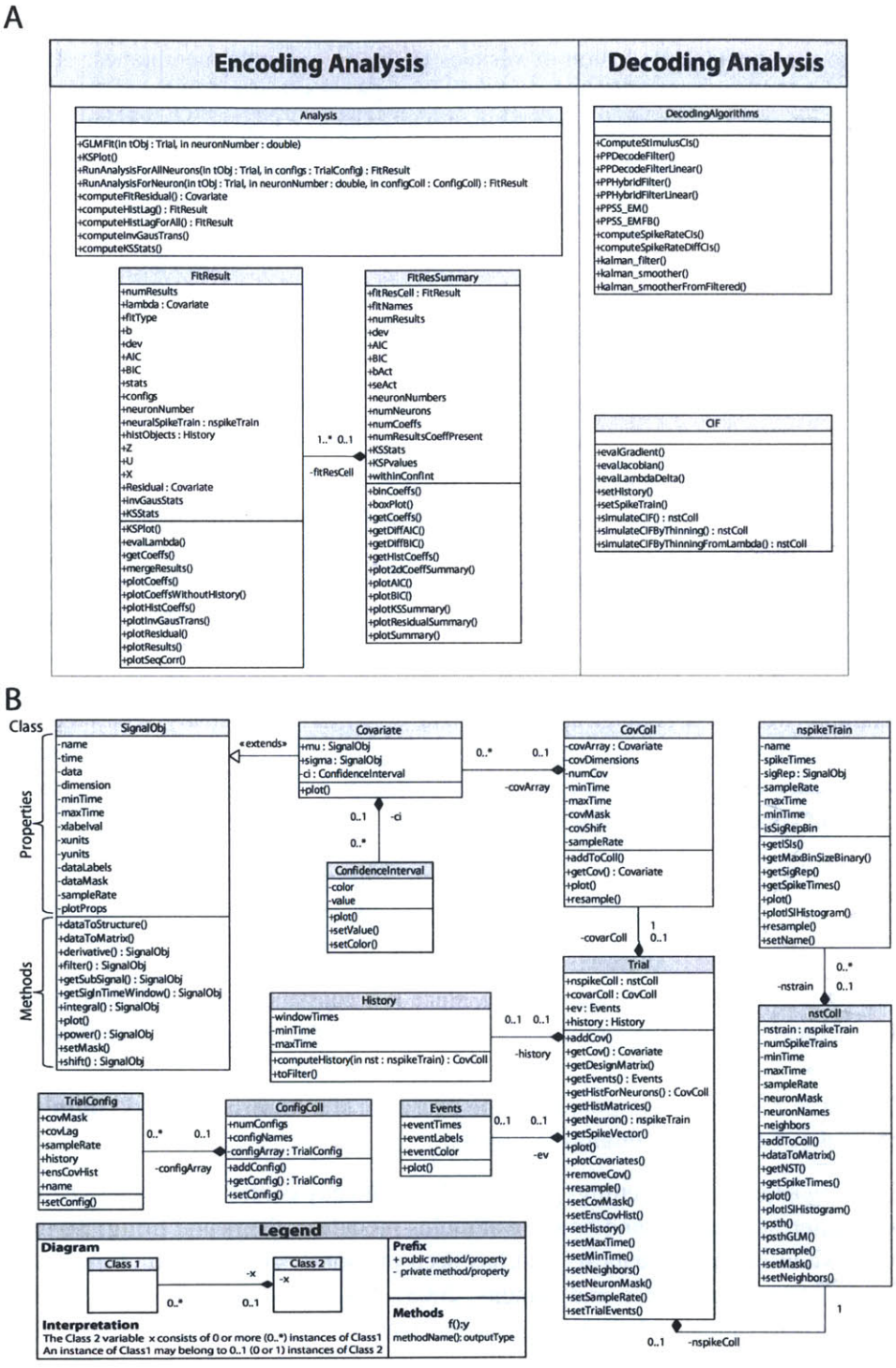

Figure 2.3: **Class Diagrams** - A) Unified Modeling Language (UML) representation of the classes that implement the encoding and decoding analysis routines and store the relevant results. B) UML diagram of the remaining classes within nSTAT.

post-synaptic currents (or "mini's") represent the response of postsynaptic receptors to the spontaneous fusion of vesicles in the pre-synaptic membranes. Recent work by Phillips et al. (2010) has shown that the arrival of mEPSCs under a constant concentration of magnesium is well described as a homogenous Poisson process (i.e. the time between mEPSCs is exponentially distributed). Additionally, as the magnesium magnesium concentration is decreased, the rate of mEPSC arrivals begins to increase.

We illustrate the use of nSTAT to analyze the arrival of mEPSCs under two distinct experimental conditions. First, we confirm homogeneous poisson behavior under constant magnesium conditions by fitting a constant conditional intensity function model to the data in Figure 2.4, e.g.

$$\log\left(\lambda\left(t|H_t\right)\Delta\right) = \mu \tag{2.21}$$

and refer to this CIF as λ_{CONST}.

As seen in Figure 2.4 C, when the magnesium concentration in decreased, the rate of mEPSC arrivals increases over time. There are many potential ways to analyze how the underlying firing rate changes with time. For example, under the assumption that the form of the conditional intensity function remains the same as Equation 2.21 we could decode the rate parameter, $\mu\left(t\right)$, using the Point Process Adaptive Filter described in Section and used in Example . However, in this example we take a simpler approach. The spike train is visually separated into three distinct epochs where the baseline firing rates are assumed to be constant within each epoch (shown in Figure 2.4). Under this assumption, we fit a piecewise constant conditional intensity function

$$\log\left(\lambda\left(t|H_t\right)\Delta\right) = \begin{cases} \mu_1 & T_0 \leq t < T_1 \\ \mu_2 & T_1 \leq t < T_2 \\ \mu_3 & T_2 \leq t < T_f \end{cases} \tag{2.22}$$

We refer to this CIF as $\lambda_{CONST-EPOCH}$ since it is constant within each time epoch. For comparison, we also fit the constant baseline model of Equation 2.21 this data.

Example 2 - Neural Responses in the presence of a known external stimulus (Whisker Stimulus/Thalamic Neurons)

In many experimental settings, the stimulus is directly controlled. In these cases it is of interest to understand how the stimulus modulates the neural firing. To illustrate we use a sample data set that has been previously summarized (Temereanca et al., 2008, Temereanca and Simons, 2003). Briefly, a piezoelectric stimulator was used to caudally deflect the principal whisker (e.g. the whisker that evoked

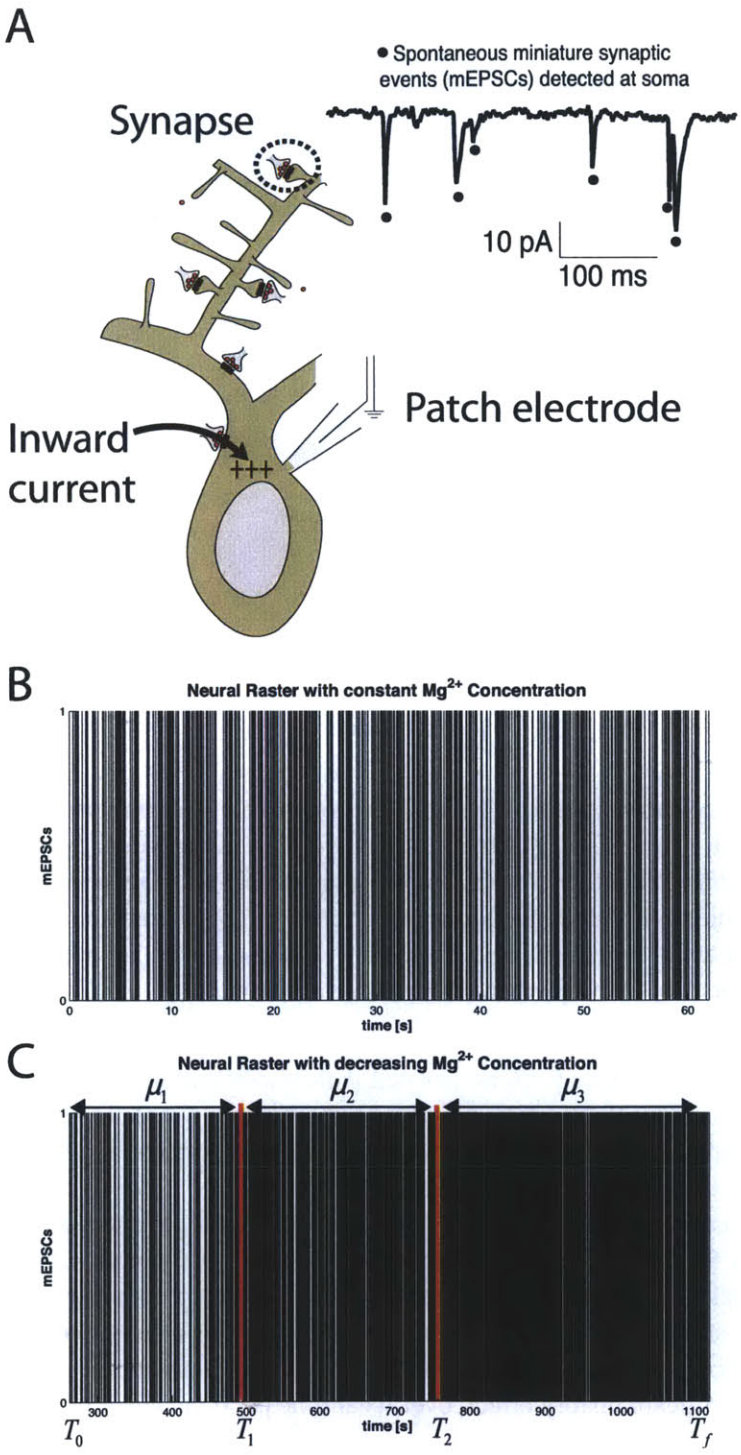

Figure 2.4: **Example 1 Data** - A) Experimental Setup B) mini Excitatory Post Synaptic Currents under a constant Magnesium concentration. C) mEPSCs as the magnesium concentration of the bath is reduced. (Image in panel A) courtesy of Marnie Phillips, PhD)

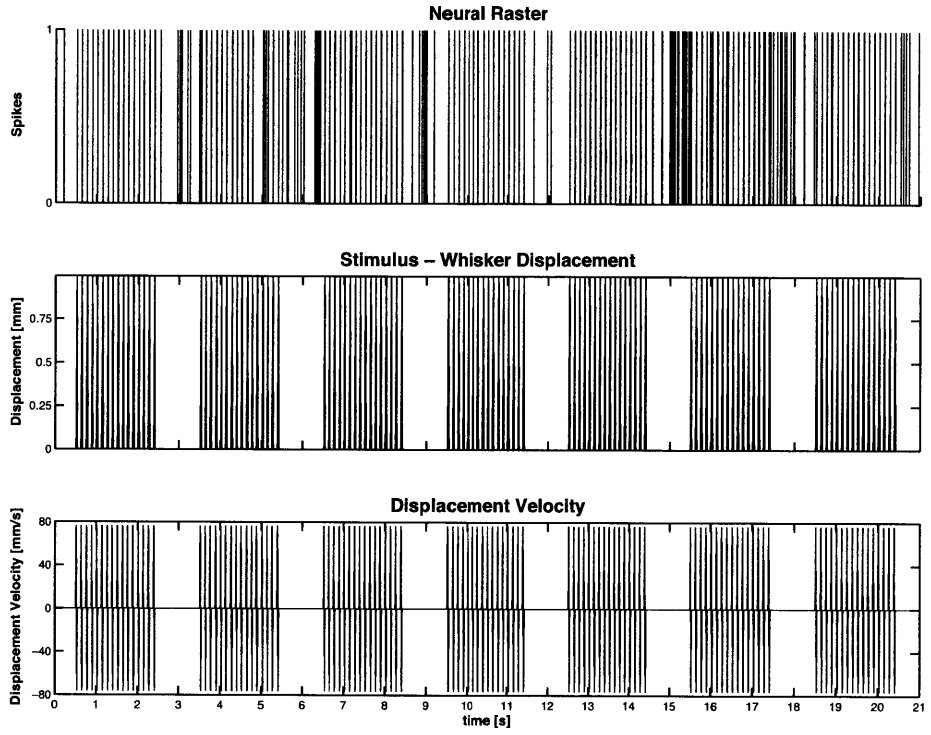

Figure 2.5: **Example 2 Data** - Thalamic neuron discharge during periodic whisker displacement. (top) Spiking activity of a single unit in the Ventral posteromedial nucleus (VPm) of the thalamus during periodic deflection of its principal whisker (PW). (middle) Whisker deflection and (bottom) whisker deflection velocity. Note that the unit tends to show firing activity that is in-phase with the applied stimulus and short bursts of activity when the stimulus is absent.

the most robust response from an isolated thalamocortical unit in the ventral posteromedial nucleus). In the data shown here, the whisker was deflected 1mm in the caudal direction beginning from the whisker's neutral position at a velocity of 80 mm/s for 2 sec with interstimulus interval of 1.5 sec.

Given such a data set, several important neurophysiologic questions become of interest: 1) Is there a significant modulatory effect of the stimulus on the neural firing? 2) What is the temporal relationship (lead vs. lag) of the neural response to the applied stimulus? 3) Does the neural firing behave as a simple inhomogenous Poisson process or is there a significant history effect (refractoriness, etc.)? 4) If there is a significant history effect, over what time period is this effect important?

In order to address these questions, we proceed as follows

1. We fit a constant baseline conditional intensity function, λ_{CONST}, as in Equation 2.21.

2. We look at the cross-correlation between the point process residual $M_{CONST}(t_k)$ (see Equation 2.7)for the λ_{CONST} fit and the known stimulus, $s(t)$, to determine the stimulus lag, τ_{lag}.

3. We fit a baseline plus stimulus model

$$\log(\lambda(t|H_t)\Delta) = \mu + b_1 s(t - \tau_{lag}) \tag{2.23}$$

   and refer to this CIF as $\lambda_{CONST+STIM}$.

4. We use model selection techniques to determine the number of history windows to include in a model with 30 logarithmically spaced history windows in the past 1 sec. That is

$$\log(\lambda(t|H_t)\Delta) = \mu + b_1 s(t - \tau_{lag}) + \sum_{j=1}^{J} \gamma_j \Delta N(t - t_{j-1}, t - t_j) \tag{2.24}$$

   where $\Delta N(t - t_{j-1}, t - t_j)$ is the total number of spikes that occurred in the time interval $[t - t_{j-1}, t - t_j)$ and J is the number of history windows to be determined via model selection. The time windows are defined such that $t_1 = 0$, $t_{30} = 1$, and t_j for $2 < j < 29$ are logarithmically spaced between 0 and 1. We refer to this CIF as $\lambda_{CONST+STIM+HIST}$.

5. Having determined the "optimal" number of history windows (via AIC, BIC, and K-S statistics), we compare the three candidate conditional intensity functions λ_{CONST}, $\lambda_{CONST+STIM}$, and $\lambda_{CONST+HIST+STIM}$ using the time-rescaling theorem (KS statistic and rescaled spike times), GLM regression coefficients and their significance, and the point process residuals for each model.

Example 3 - Neural Responses to an unknown/implicit stimulus

Recording single-neuron activity from a specific brain region across multiple trials in response to the same stimulus or execution of the same behavioral task is a common neurophysiology protocol. In order to capture the effective neural stimulus that results from the applied physical stimulus, many investigators turn to the peri-stimulus time histogram. To illustrate the construction of PSTH based on a neural raster using nSTAT, we use both simulated and actual data. In Figure 2.6 A,

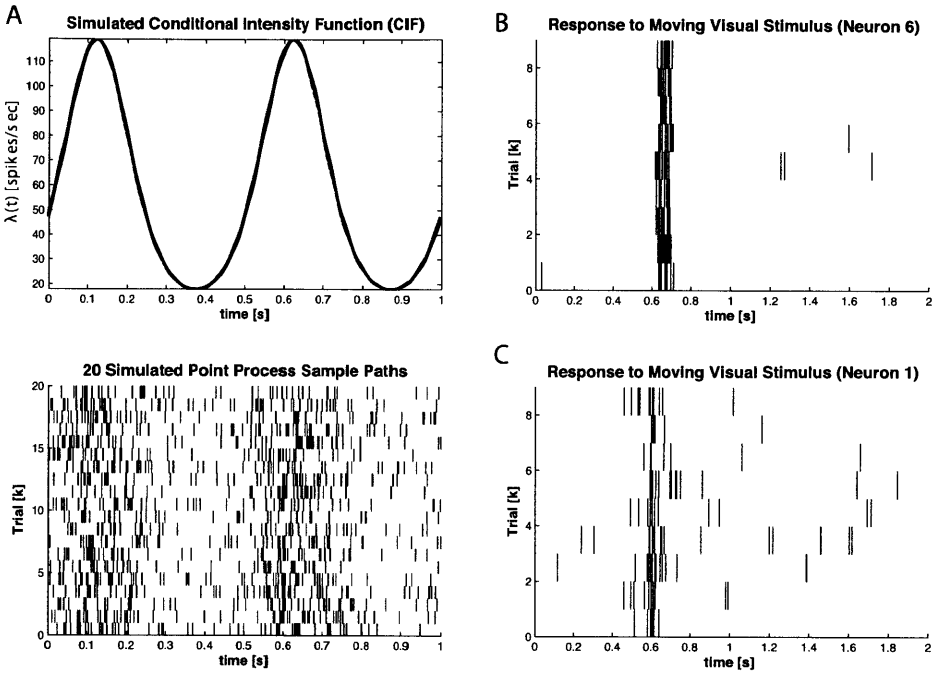

Figure 2.6: **Example 3 PSTH Data** - Simulated and Actual Data for PSTH Computation. A) (top) A graph of $\lambda(t)$ from Equation 2.25 (bottom) Raster of 20 "cells" obtained from the conditional intensity function in Equation 2.25 via the Point Process Thinning Algorithm. B) 9 trials of stimulus exposure to a single cell. C) Same as B) with different cell.

the point process thinning algorithm was used to generate 20 realizations of a point process governed by the conditional intensity function

$$\text{logit}(\lambda(t)\Delta) = \sin(2\pi f t) + \mu \tag{2.25}$$

where $f = 2$ and $\mu = -3$.

Figure 2.6 B and C show the response of two V1 neurons when a visual stimulus was shown to an adult monkey during a fixation period in response to a moving bar. This data has been published previously (Pipa et al., 2009, 2011).

SGLM-PSTH To demonstrate how the SSGLM framework described in Section can be applied to estimate both within-trial and across-trial effects we simulate the

following conditional intensity function

$$\text{logit}\left(\lambda\left(k,t_n|H_{t_n}\right)\Delta\right) = \mu + b_k \sin\left(2\pi f t_n\right) + \sum_{j=1}^{J} \gamma_j \Delta N_k\left(t_n - t_{j-1}, t_n - t_j\right) \quad (2.26)$$

$$b_k = \frac{3k}{K} \quad (2.27)$$

where $\lambda\left(k,t_n|H_{t_n}\right)$ is the CIF in the n^{th} time bin of the k^{th} trial, $\mu = -3$ (corresponds to a baseline firing rate of approximately 50 Hertz), $\Delta = .001$ s, $f = 2$, $K = 50$ is the total number of trials, $J = 3$, $t_j = j$ milliseconds for $j = 0,\ldots,J$, and $\gamma = \begin{bmatrix} \gamma_1 & \gamma_2 & \gamma_3 \end{bmatrix}^T = \begin{bmatrix} -4 & -1 & -0.5 \end{bmatrix}^T$. The inclusion of the history term models the refractory period of the cell. We refer to $\sin\left(2\pi f t\right)$ as the within-trial stimulus (since it is consistent across all trials) and b_k as the across-trial stimulus. The aim of the SSGLM framework is to estimate the history parameter vector, γ, and the non-history dependent stimulus parameters. The SSGLM framework returns an estimate of the stimulus-dependent component of the CIF, e.g.

$$\text{logit}\left(\lambda_{stim}\left(k,t|H_t\right)\Delta\right) = \mu + b_k \sin\left(2\pi f t\right) \quad (2.28)$$

for $k = 1,\ldots,50$.

Example 4 - Neural Responses to a continuous stimulus - Hippocampal place cells

In the rat hippocampus (a region of the brain important for long-term memory formation) pyramidal neurons known as place cells form spatial receptive fields as the animal forages in its environment (O'Keefe and Dostrovsky, 1971, O'Keefe, 1976, O'Keefe and Conway, 1978). In order to show how the spatial receptive fields can be estimated using nSTAT, we reproduce the analysis of Barbieri et al. (2005b) which compared the accuracy of receptive fields constructed using a Gaussian kernel versus Zernike polynomials. Briefly, a Long-Evans rat was allowed to freely forage in a circular environment 70 cm in diameter with 30 cm high walls and a fixed visual cue. A multi-electrode array was implanted into the CA1 region of the hippocampus. The simultaneous activity of 49 place cells was recorded from the electrode array while the animal foraged in the open circular environment for 25 min. Simultaneous with the recording of the place cell activity, the position was measured at 30 Hz by a camera tracking the location of two infrared diodes mounted on the animal's head stage. Figure 2.8 shows the response of 4 randomly selected cells.

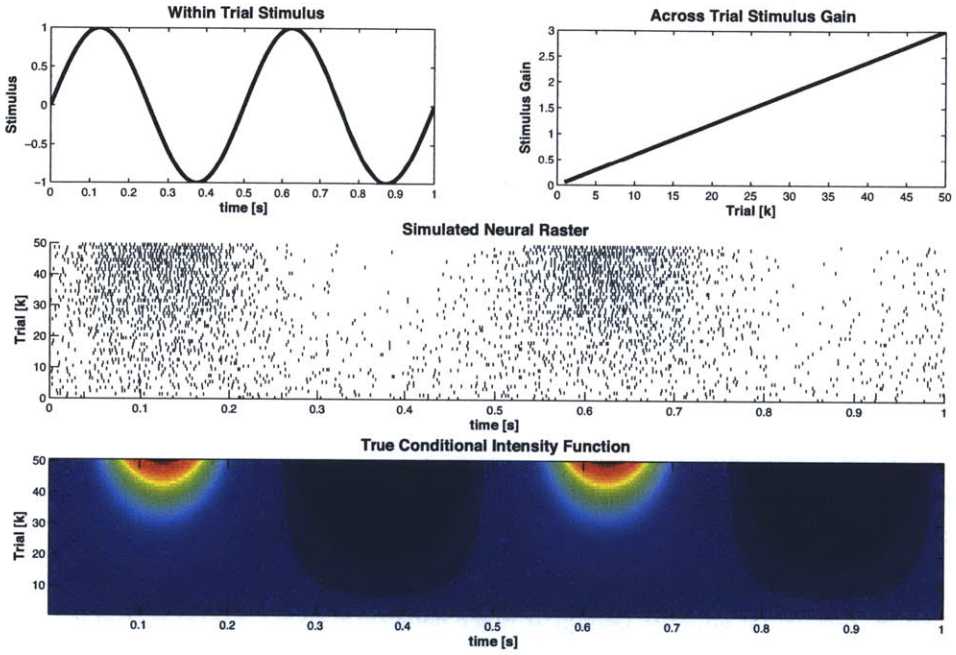

Figure 2.7: **Example 3 SSGLM Data** - Time varying stimulus response. The within-trial stimulus is modulated by the across-trial stimulus gain in order to simulate neural plasticity across trials. The simulated neural raster is generated via the time rescaling algorithm described in Section using the nSTAT CIF class. The true conditional intensity function is obtained from Equation 2.28.

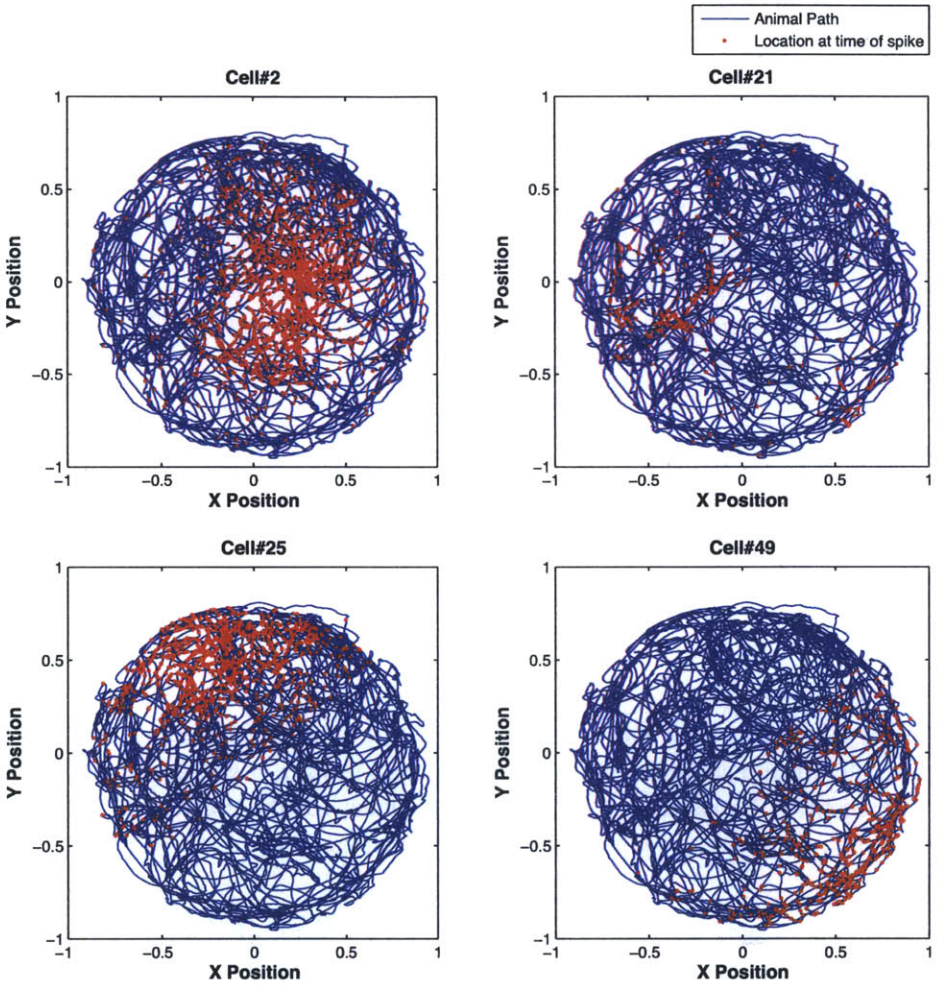

Figure 2.8: **Example 4 Data** - Hippocampal neural firing during free foraging. Four cells recorded while a rat was freely foraging in a circular environment. The x-y position at which the cell fires is denoted in red and superimposed on the path of the freely foraging rat in blue. Note that each cell tends to fire near certain locations more than others. The goal in experiments such as this one is to estimate the receptive field or "place" field of each cell based on the recorded spiking activity.

Estimation of the spatial receptive fields using a Gaussian kernel is equivalent to finding the mean, covariance, and baseline firing rate for the conditional intensity function, λ_G, defined as

$$\log(\lambda_G(t|x(t),\theta_G)\Delta) = \alpha - \frac{1}{2}(x(t)-\mu)^T Q^{-1}(x(t)-\mu) \tag{2.29}$$

where α is the baseline firing rate, $x(t) = [x(t), y(t)]^T$ is the normalized position vector of the rat consisting of the x and y coordinates of the rat within the circular environment, and μ the mean and Q the covariance of the two-dimensional Gaussian kernel respectively. Here θ_G represents the parameters on the right hand side of Equation 2.29. In order to perform the model fits we need to specify the covariates that will be used in the GLM regression. We expand Equation 2.29 and rewrite in standard matrix notation as

$$\begin{aligned}\log(\lambda_G(t|x(t),\theta_G)\Delta) &= \begin{bmatrix} 1 & x(t) & x(t)^2 & y(t) & y(t)^2 & x(t)\cdot y(t) \end{bmatrix} \begin{bmatrix} b_0 \\ b_1 \\ b_2 \\ b_3 \\ b_4 \\ b_5 \end{bmatrix} \\ &= X_G\beta_G \end{aligned} \tag{2.30}$$

where 1 is a vector with every element equal to 1 and of appropriate length. We define each of the columns of the design matrix, X_G, as a covariate for the fitting of the GLM in Equation 2.30. The second model for the conditional intensity function, corresponding to the Zernike polynomial basis, λ_Z, is defined as

$$\log(\lambda_Z(t|x(t),\theta_Z)\Delta) = \mu + \sum_{l=0}^{L}\sum_{m=-l}^{l}\theta_{l,m}z_l^m(p(t)) \tag{2.31}$$

where z_l^m is the m^{th} component of the l^{th} order Zernike polynomial, $p(t) = [\rho(t), \phi(t)]$ is the polar coordinate representation of the Cartesian position vector $x(t)$ and $\theta_Z = \left\{\{\theta_{l,m}\}_{m=-l}^{l}\right\}_{l=0}^{L}$. We rewrite the equation in matrix notation

$$\log(\lambda_Z(t|x(t),\theta_Z)\Delta) = \begin{bmatrix} 1 & z_1(p(t)) & \cdots & z_{10}(p(t)) \end{bmatrix} \begin{bmatrix} \mu \\ \theta_1 \\ \vdots \\ \theta_{10} \end{bmatrix} \tag{2.32}$$

$$= X_Z\beta_Z \tag{2.33}$$

where the notation has been replaced by an ordered numbering of the 10 unique non-zero Zernike polynomials for $L = 3$ as used by Barbieri et al. (2005b). We define each of the columns of the design matrix, X_Z, as a covariate for the fitting of the GLM in Equation 2.32

Example 5 - Decoding Continuous Stimuli based on Point Process Models

Decoding a driving stimulus from Point Process Observations

Suppose we have a collection of $c = 1,...,C$ cells with conditional intensity function

$$\text{logit}\left(\lambda^c(t)\Delta\right) = b_0^c + b_1^c \sin\left(2\pi f t\right) \tag{2.34}$$

as shown in Figure 2.9. We define the stimulus $x(t) = \sin(2\pi f t)$ and aim to obtain an estimate $\hat{x}(t)$ of the true stimulus $x(t)$ based on the ensemble firing activity $\Delta N^{1:C}(t)$ and knowledge of each $\lambda^c(t)$. For this example we choose, $C = 20$, $f = 2$, $b_0 \sim \mathcal{N}(\mu = -4.6, \sigma = 1)$, and $b_1 \sim \mathcal{N}(\mu = 0, \sigma = 1)$. A value of $b_0 = -4.6$ corresponds to a baseline firing rate of approximately 10 spikes/sec. Simulated spike trains for each cell, obtained via the point process thinning algorithm, are shown in Figure 2.9.

Decoding a movement trajectory from Point Process Observations

Suppose that we have a collection of cells $c = 1,...,C$ with condition intensity function adapted from a model of primary motor cortex (Moran and Schwartz, 1999, Srinivasan et al., 2006)

$$\begin{aligned} \log\left(\lambda^c(t|v_x, v_y)\Delta\right) &= \beta_0^c + \beta_1^c \left(v_x^2 + v_y^2\right)^{1/2} cos\left(\theta - \theta_p^c\right) \\ &= \beta_0^c + \alpha_1^c v_x + \alpha_2^c v_y \end{aligned} \tag{2.35}$$

where v_x and v_y are velocities of the arm end-effector in orthogonal directions. An arm reach from an initial position, $x_0 = [0,0]^T$, to a target at $x_0 = [-35,20]^T$ cm was simulated using the reach-to-target equation in (Srinivasan et al., 2006). The resulting velocities were used to generated a CIF according to Equation 2.35 and neural rasters were generated using the point process thinning algorithm. The final and initial state covariances were $\Lambda_{x_0} = \Lambda_{x_T} = \varepsilon \times I_{4\times4}$, where $\varepsilon = 10^{-6}$ and $I_{4\times4}$ is the 4×4 identity matrix. The corresponding receptive field parameters were selected so that each cell had preferred direction uniformly distributed between $-\pi$ and π, and $\beta_0^c \sim \mathcal{N}(\mu = -4.6, \sigma = 1)$. The same velocity information was used to simulate the firing of $C = 20$ distinct cells a total of 20 times to show how the algorithm performed in the presence of varying cell responses.

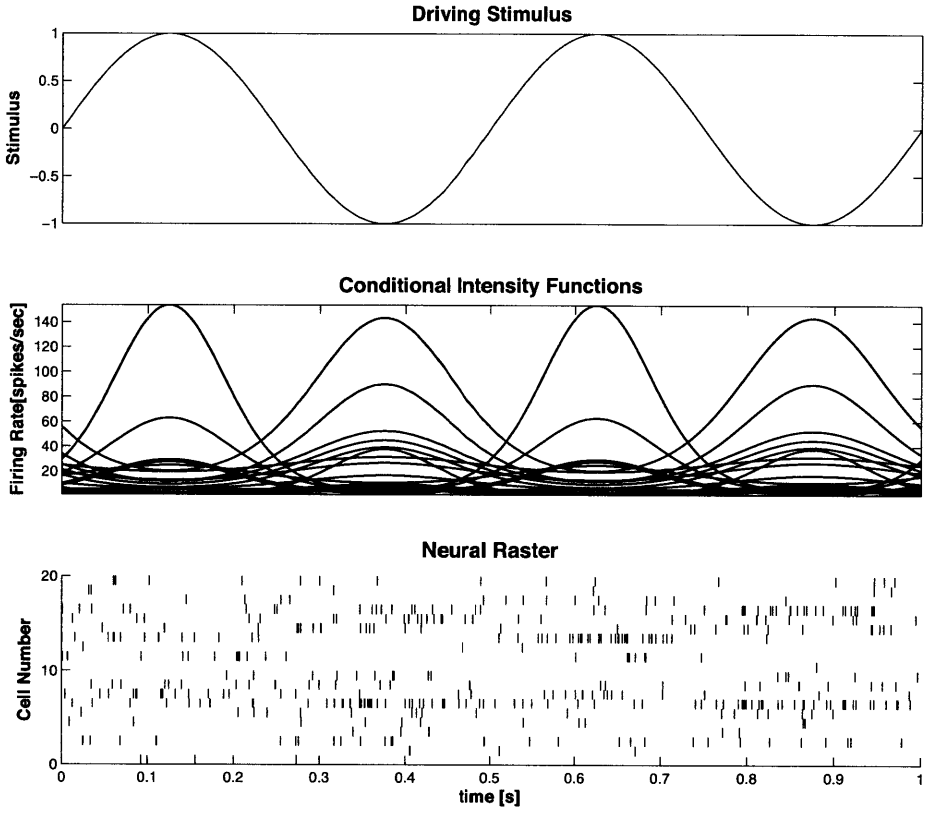

Figure 2.9: **Example 5 Driving Stimulus Data** - (top) Driving stimulus, (middle) conditional intensity function for each cell, (bottom) raster of simulated cells begin driven by a sinusoidal stimulus.

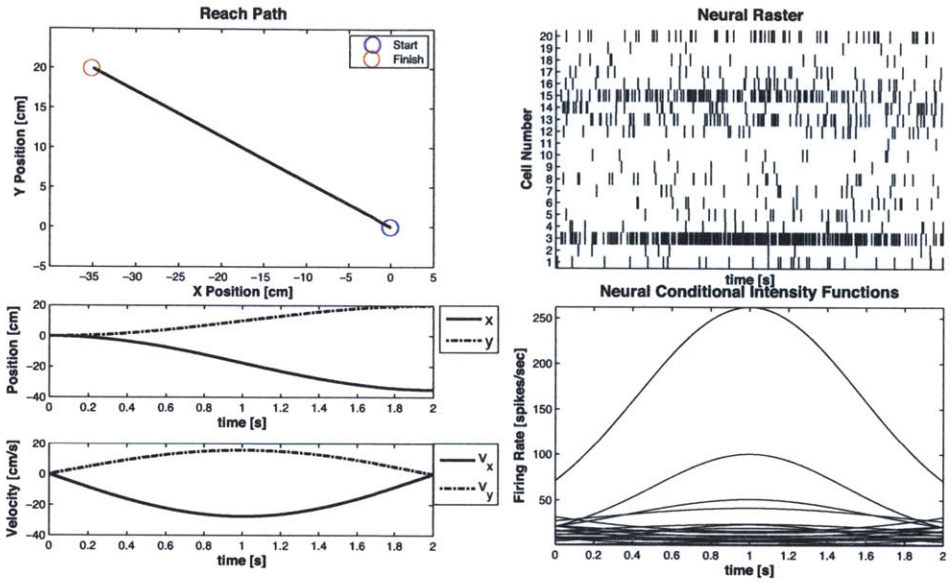

Figure 2.10: **Example 5 Movement Trajectory Data** - Reach-to-target simulated data

Results

Example 1 - Constant and piece wise constant Poisson process - The Miniature Excitatory Post-Synaptic Current

Figure 2.11 summarizes the results of mEPSC data in Example 1. Under constant magnesium concentrations, the mEPSC data is well fit by the constant conditional intensity function in Equation 2.21, suggesting that the inter-spike-interval (ISI) distribution for the mEPSC events is well described by an exponential distribution. The KS plot for λ_{CONST} lies within the 95% confidence bands indicating that the u_s's do not significantly differ from a uniform distribution on the interval $(0,1)$. The autocorrelation function of the x_s's help us determine that the transformed times are also independent. Together, these results indicate that λ_{CONST} is a good approximation to the true underlying conditional intensity function describing the mEPSC process under constant magnesium concentrations.

Figure 2.11 B shows a comparison of the constant rate model in Equation 2.21 and the piecewise constant rate model in Equation 2.22. Since both the K-S plot and the autocorrelation function of the x_s's for the piecewise constant model lie within the 95% confidence interval, we conclude $\lambda_{CONST-EPOCH}$ more ade-

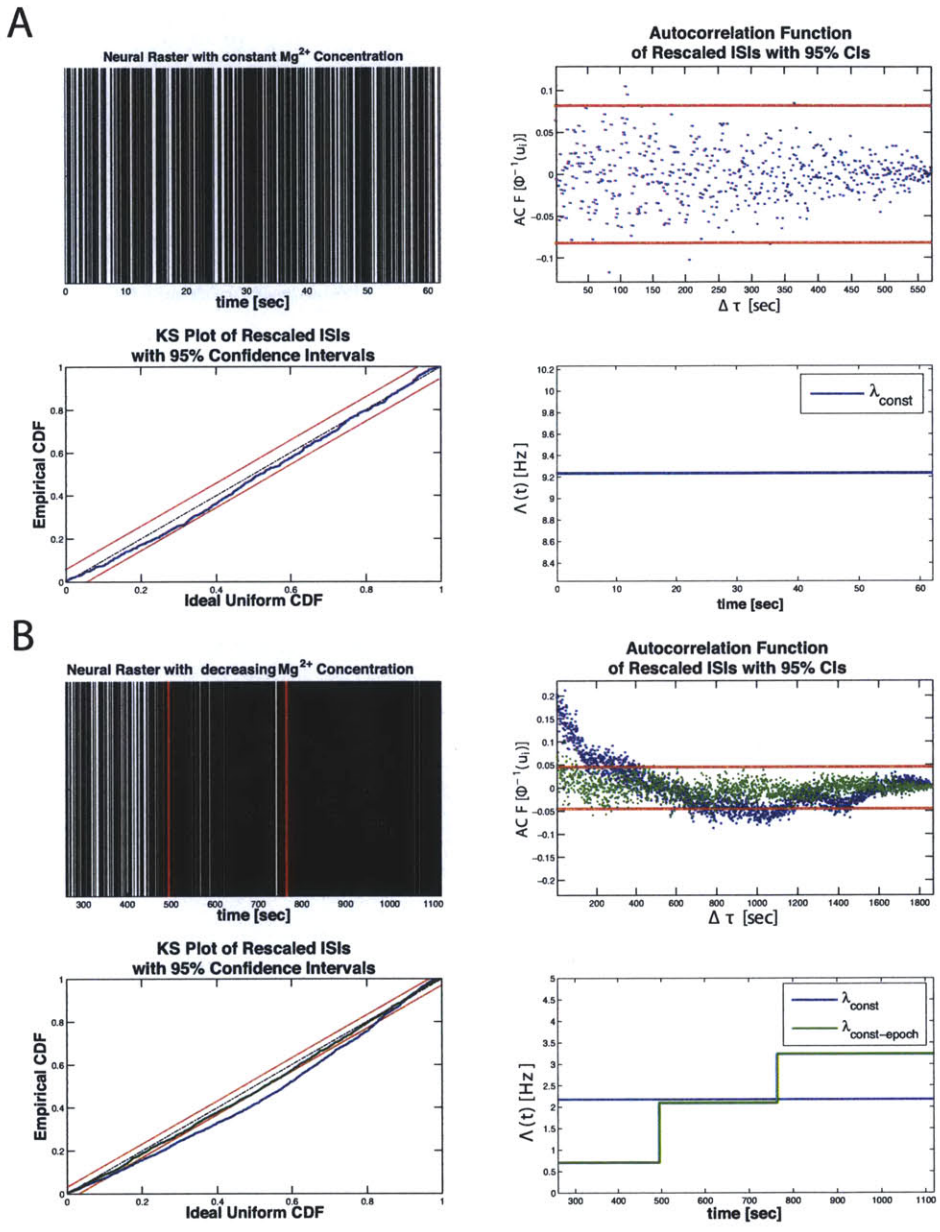

Figure 2.11: **Example 1 Results**. A) nSTAT results summary for the constant baseline firing rate model (Equation 2.21) for the mEPSC data in Figure 2.4 B). (top, left to right) original neural raster, autocorrelation function of the u_s's, K-S Plot, and conditional intensity function estimate. B) (top, left to right) Raster of mEPSC data under varying magnesium concentration, autocorrelation function of the u_s's, K-S Plot and CIF estimate. Note that the piecewise constant rate model yields a K-S plot that falls within the 95% confidence bands and produces rescaled event times whose autocorrelation function is closer to zero across all lags – suggesting independence of the rescaled times under $\lambda_{CONST-EPOCH}$. The estimated CIF (lower right panel) is able to capture the increased rate that is observed in Figure 2.4 C).

quately approximates the true underlying conditional intensity function describing the mEPSC activity under varying magnesium concentrations.

Example 2 - Neural Responses in the presence of a known external stimulus Whisker Stimulus/Thalamic Neurons

Figure 2.12 summarizes the results of the analysis presented in Section . Analysis of the cross-correlation function between the point process residual from the model in Equation 2.21 and the whisker-deflection stimulus demonstrates that the neural firing lags the stimulus by 119 ms. Changes in AIC, BIC and KS statistic are shown in Figure 2.12 B for increasing values of J and indicate that $J = 9$ history windows is most consistent with the data (red star). Figure 2.12 D demonstrates how this length of history captures important temporal properties of the neuron including the refractory period and bursting (i.e. increased firing probability when last spike occurred in the last 1-5ms). Additionally, the GLM regression coefficient for the baseline firing rate indicates that the neuron has a baseline rate of 6.5 Hz $(\exp(-5)/\Delta)$ and that the increased whisker displacement (positive stimulus) has an excitatory effect on the neural firing. Lastly, Figure 2.12 demonstrates that $\lambda_{CONST+STIM+HIST}$ yields a K-S plot that lies within the 95% confidence interval and thus is an adequate description of the true underlying CIF according to the time rescaling theorem.

Example 3 - Neural Responses in the presence of an unknown/implicit stimulus

PSTH

Figure 2.13 compares estimation of PSTH via the standard approach (Gerstein and Kiang, 1960, Palm et al., 1988) and using the GLM formulation of Czanner et al. (2008). Note that the standard PSTH and the PSTH-GLM match exactly. Confidence bands for the PSTH-GLM are indicated by the opaque black lines.

SSGLM-PSTH

Figure 2.14 summarizes the application of the standard PSTH and SSGLM frameworks to the data in Figure 2.7. As shown in Figure 2.14 A and B, the SSGLM estimate of the stimulus effect with 40ms bins is in close agreement with the true underlying stimulus effect. The standard PSTH method (also using 40ms bins) fails to capture the across-trial dynamics (because of its assumption that all of the trials are identical and independent) but is able to capture the within-trial dynamics grossly. Figure 2.14 C shows the spike rate function, $(t_2 - t_1)^{-1} \Lambda_k(t_1, t_2)$, for

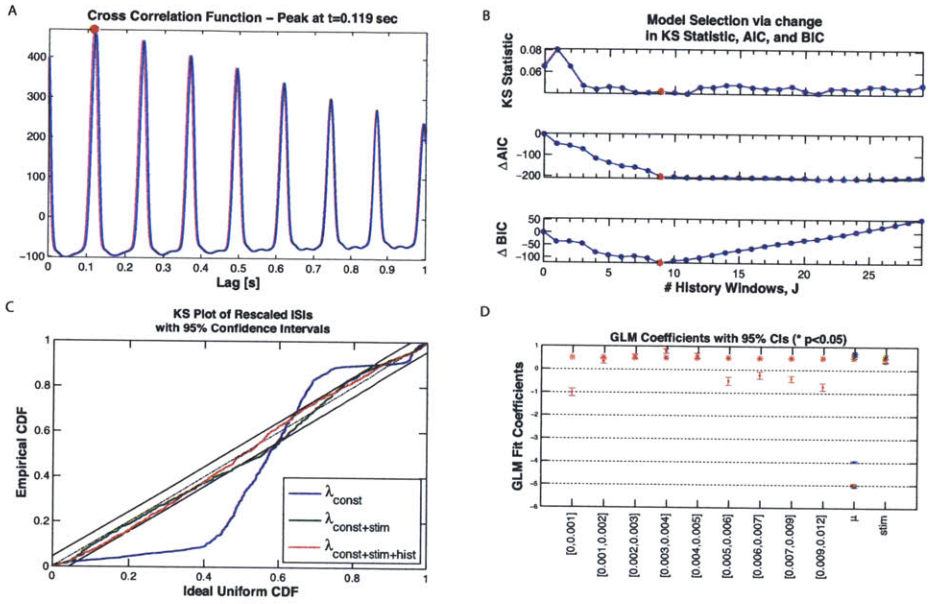

Figure 2.12: **Example 2 Results.** A) Cross-correlation of the constant baseline model residual, $M_{CONST}(t)$, with the stimulus, $s(t)$. The peak at 0.119 seconds suggests that the neural activity lags the stimulus by just over 100ms. B) Model selection for number of history windows. The model in Equation 2.22 was fit for $J = 1, ..., 30$. A minimum in the AIC, BIC, and KS-statistic is observed when $J = 9$ (9 logarithmically spaced time windows over the interval $[0, 12\text{ms}]$), suggesting this as the best choice for the length of history dependence. C) K-S Plot comparison of λ_{CONST}, $\lambda_{CONST+STIM}$, and $\lambda_{CONST+STIM+HIST}$. Inclusion of the stimulus effect yields an improvement in the K-S plot but the resulting model does not fall within the 95% confidence bands. Addition of the history dependence produces a K-S plot that does fall within the 95% confidence bands. D) GLM coefficients for all three candidate models. Note that the history coefficients capture an initial refractory period (within the first 1ms of firing), a region of increased firing probability shortly thereafter (from 1ms-5ms) corresponding to the bursting seen in the absence of the stimulus, and a subsequent period of decreased firing probability.

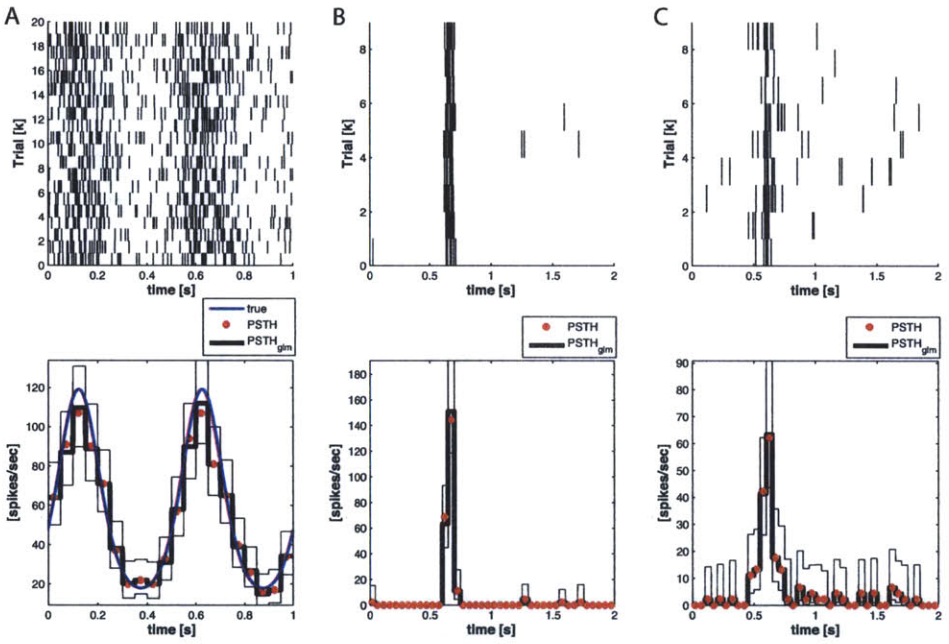

Figure 2.13: **Example 3 PSTH Results.** A) (top) Raster of 20 cells obtained from the conditional intensity function in Equation 2.25via the point process thinning algorithm. (bottom) Comparison of PSTH (red) and PSTH-GLM (black) with 50ms seconds bins to the actual conditional intensity function (blue). Note that the standard PSTH and the PSTH-GLM match exactly. Confidence bands for the PSTH-GLM are shown by the opaque black lines. B) Neuron #6 raster (top) with corresponding PSTH and PSTH-GLM (bottom). C) Neuron #1 raster (top) and corresponding PSTH and PSTH-GLM (bottom).

History Coefficient	Actual	GLM PSTH Estimates (mean±se)	SSGLM Estimates (mean±se)
γ_1	-4	-3.4047 ± 0.2671	-3.4047 ± 0.0024
γ_2	-1	-0.9044 ± 0.0734	-0.9044 ± 0.0085
γ_2	-0.5	-0.3568 ± 0.0643	-0.3568 ± 0.0094

Table 2.1: **History Dependence Parameter Estimates.** Note that both the GLM PSTH and SSGLM methods estimate the same parameters but SSGLM yields estimates with a smaller standard error. This is likely due to more stringent convergence criteria for the SSGLM algorithm (i.e. given additional iterations the GLM PSTH estimates would also yield estimates with smaller standard errors).

$k = 1,...,50$ and the learning trial estimate obtained by computation of the probability in Equation 2.14 (shown in 2.14 E for all trials). Figure 2.14 D shows the within-trial stimulus effect for trial 1 and trial 9 (the learning trial) for comparison.

Example 4 - Neural Responses in the presence of a continuous stimulus - Hippocampal place cells

As demonstrated by Barbieri et al. (2005b), the Zernike polynomial model gave a more accurate and parsimonious description of the individual place fields according to both Akaike and Bayesian Information Criterion (see Figure 2.15 D). The Zernike place field estimates were concentrated in a smaller area and had a wider range of asymmetric shapes (Figure 2.15 A versus Figure 2.15 B).

Example 5 - Decoding Continuous Stimuli based on Point Process Models

Decoding a driving stimulus from Point Process Observations

Figure 2.16 shows the results of decoding the sinusoidal stimulus in Equation 2.34 using 20 cells. Note that even though the original neural raster in Figure 2.9 showed very little correspondence to the driving stimulus, the aggregate information across the population of cells was sufficient to yield an adequate estimate of the stimulus.

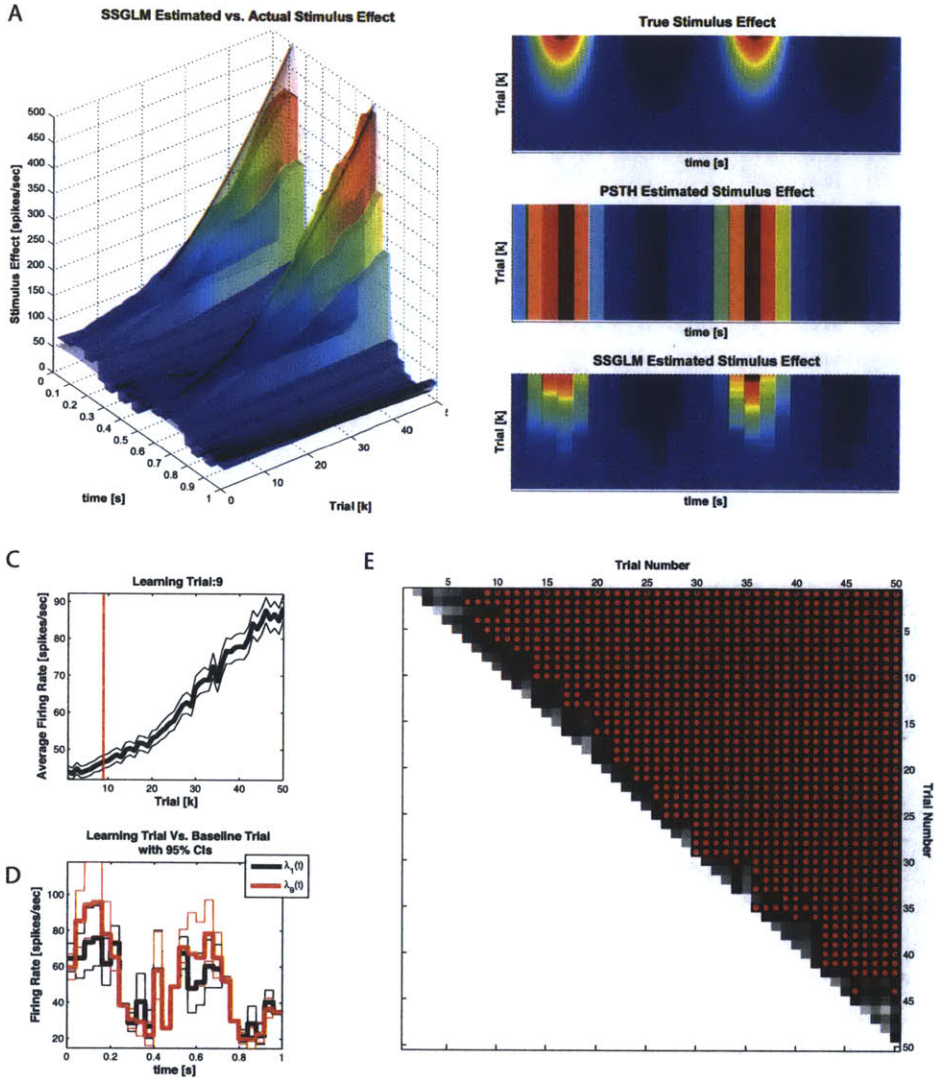

Figure 2.14: **Example 3 SSGLM Results**. A) SSGLM Estimated versus actual stimulus response. Both the PSTH and SSGLM estimates partitioned the time axis using 40ms time bins. B) Comparison of PSTH, SSGLM, and actual stimulus response. C) Plot of the spike rate function, $(t_2 - t_1)^{-1} \Lambda_k(t_1, t_2)$, for $k = 1, ..., 50$. The learning trial, trial 9, is indicated by the vertical red line. D) Comparison of the within-trial spike firing rate (stimulus effect) between the baseline (first) trial and the learning trial. E) Spike rate function comparison matrix. The probability in Equation 2.14 was computed for $k = 1, ..., 49$ and $m > k$. For each trial k on the vertical axis, the * indicates which trials $m > k$ (on the horizontal axis) have an estimated spike rate function that is greater than the spike rate function at trial k with probability greater than 95%.

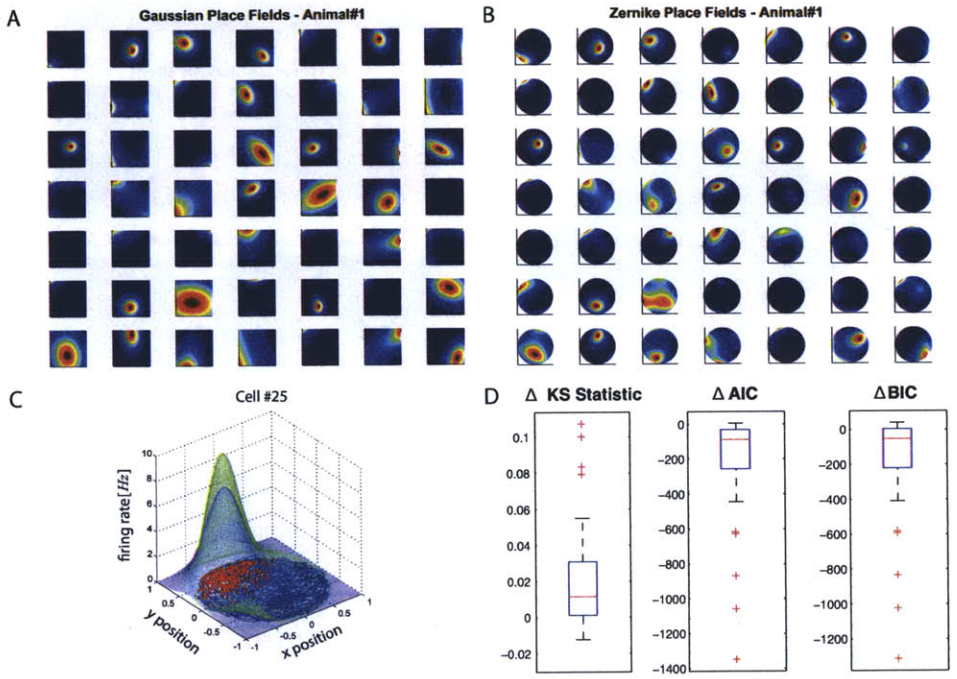

Figure 2.15: **Example 4 Results** - Hippocampal place cell receptive field estimates. A) Gaussian Place fields. B) Zernike place fields. Note that the place fields estimated with the Zernike polynomial basis are able to capture receptive field asymmetries better than the Gaussian estimates. C) Comparison of Zernike and Gaussian receptive field for cell #25. The Gaussian fit is in blue and the Zernike polynomial fit is in green. D) Box plot of change in KS statistics, AIC and BIC across all 49 cells computed as value of statistic in the Gaussian fit minus the value in the Zernike polynomial fit. Note that while the median KS statistics using Gaussian or Zernike basis are similar, the model corresponding to the Zernike receptive fields yield an improvement in terms of the change in AIC and BIC - indicating that the Zernike polynomial models are better fits to the data. Note that for some cells (the outliers marked in red), the improvement is quite dramatic with the use of the Zernike polynomials.

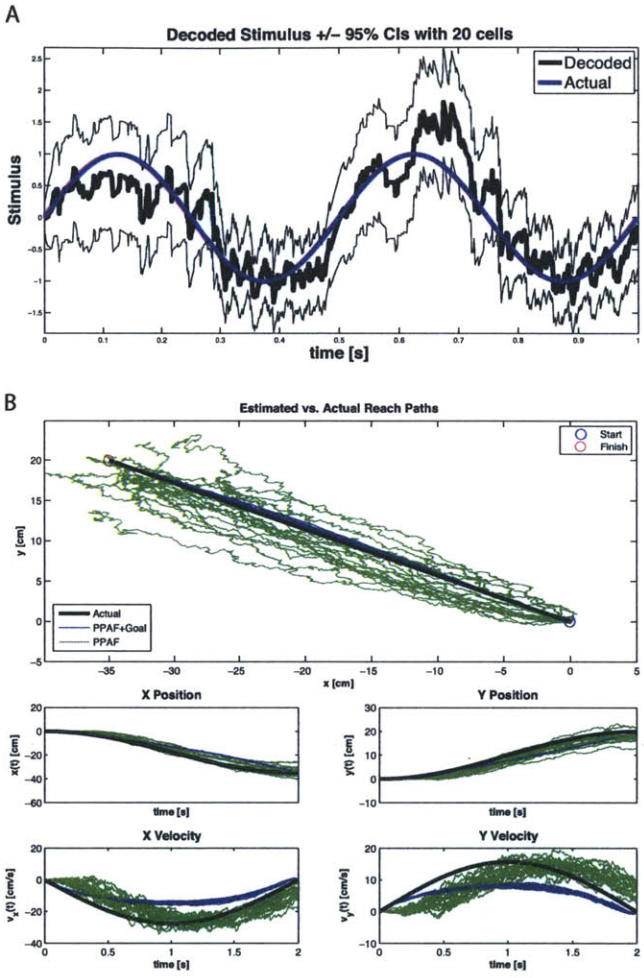

Figure 2.16: **Example 5 Results.** A) Stimulus decoding using the point process adaptive filter. The firing activity of the 20 simulated cells was used with the PPAF in order to decode the stimulus in Equation 2.25. The estimated stimulus is shown in black with the corresponding 95% confidence intervals illustrated by surrounding lines in black. The actual stimulus is shown in blue. B) Decoded movement trajectory using the PPAF (green) and the PPAF with target information (blue). For each trace, the true velocity information was used to simulate the firing of 20 distinct cells according to Equation 2.35 using the point process thinning algorithm. Each cell had a randomly chosen preferred direction. This process was repeated 20 times to show how the algorithms performed in the presence of different cell populations. (top) The PPAF+Goal estimated path in a more faithful reconstruction of the true movement path and shows significantly less variability in across the 20 simulations. Note, however, that comparison the actual movement trajectories shows that the PPAF without goal information is more closely able to track the actual movement dynamics (albeit with significant variability). As the covariance of the final target increases (i.e. certainty in the final target decreases), the PPAF+Goal estimated trajectories become more similar to the PPAF estimates (data not shown).

Decoding a movement trajectory from Point Process Observations

Figure 2.16 B shows the results of decoding a simulated reach using the point process adaptive filter (green) and the point process adaptive filter with the addition of target information (blue). Note that inclusion of target information causes deviation from the actual movement trajectories, but results in improved estimates of the true movement path and ensures arrival at the final target. When the target information is not present, the PPAF tracks the true trajectories more reliably (albeit with larger variability) but rarely reaches the true final target. As the degree of certainty in the final target is decreased (i.e. the final target covariance increases), the decoded trajectories become more similar to the standard PPAF without target information.

Discussion

We have developed the neural Spike Train Analysis Toolbox (nSTAT) for Matlab® to facilitate the use of the Point Process - Generalized Linear Model framework by the neuroscience community. By providing a simple software interface to PP-GLM specific techniques within the Matlab® environment, users of a number of existing open source toolboxes (i.e. Chronux, STAToolkit, etc.) will be able to easily integrate these techniques into their workflow. It is our hope that making nSTAT available in an open-source manner will shorten the gap between innovation in the development of new data analytic techniques and their practical application within the neuroscience community. For the neurophysiologist, we hope the availability of such a tool will allow them to quickly test the range of available methods with their data and use the results to both inform the quality of their data and refine the protocols of their experiments.

Via a series of examples we have demonstrated the use of the toolbox to solve many common neuroscience problems including: 1) systematic building of models of neural firing, 2) characterization of explicit experimental stimulus effects on neural firing, 3) spike rate estimation using the PSTH and extensions of the PSTH (SSGLM) that allow quantification of experience-dependent plasticity (across-trial effects), 4) receptive field estimation, and 5) decoding stimuli such as movement trajectories based on models of neural firing. All of the data, code, and figures used here are included as part of the toolbox. We hope that users will be able to easily modify these examples and use them as a starting point for analysis of their own data.

While the current release of nSTAT contains many commonly used algorithms for analysis of neural data within the PP-GLM framework, there are many avenues for future improvement. In particular, optimization of current algorithm imple-

mentations to support the GPU- and parallel-computing methods within Matlab® are likely to be important for dealing with large data sets. We encourage users to identify areas were the software can be made more efficient and to make their contributions available to the community at large. Future work for nSTAT will include the addition of methods to deal with simultaneous analysis of neural ensembles using multivariate point-process theory together with multinomial generalized linear models (mGLMs) (Chen et al., 2009e, Ba, 2011, Brown et al., 2004), network analysis of multivariate spike trains(Brown et al., 2004, Krumin and Shoham, 2010, Stam and Reijneveld, 2007, Bullmore and Sporns, 2009), and incorporation of causal modeling techniques for neural ensembles (Kim et al., 2011) among others.

Acknowledgement

This work was supported by NIH F31NS058275 - "Automated and Adaptive Lower Extremity Neuro-Rehabilitation for Stroke" to Iahn Cajigas. The authors are indebted to Riccardo Barbieri and Simona Temereanca (Harvard Medical School), Marnie Phillips, Laura Lewis, and Demba Ba (MIT), and Gordon Pipa (Max Planck Institute for Brain Research) for providing the data used to make the examples. The authors would like to thank the reviewers for their constructive comments and suggestions for improving the manuscript, and the members of the MIT Neuroscience Statistics Research Lab for their collegial support.

References

Akaike, H.. Information Theory And An Extension Of The Maximum Likelihood Principle. Second International Symposium on Information Theory 1973;1(1973):267–281.

Andersen, P.K.. Statistical models based on counting processes. New York: Springer, 1997.

Azzalini, A., Bowman, A.W.. A Look at Some Data on the Old Faithful Geyser. Appl Stat-J Roy St C 1990;39(3):357–365.

Ba, D.E.. Algorithms and inference for simultaneous-event multivariate point-process, with applications to neural data. Ph.D. thesis; Massachusetts Institute of Technology; Cambridge; 2011.

Barbarossa, S., Scaglione, A., Baiocchi, A., Colletti, G.. Modeling network traffic data by doubly stochastic point processes with self-similar intensity process

and fractal renewal point process. In: Signals, Systems & Computers, 1997. Conference Record of the Thirty-First Asilomar Conference on. 1997. p. 1112–1116.

Barbieri, R., Brown, E.N.. A point process adaptive filter for time-variant analysis of heart rate variability. In: Engineering in Medicine and Biology Society, 2004. IEMBS '04. 26th Annual International Conference of the IEEE. 2004. p. 3941–3944.

Barbieri, R., Brown, E.N.. Analysis of heartbeat dynamics by point process adaptive filtering. IEEE Trans Biomed Eng 2006a;53(1):4–12.

Barbieri, R., Brown, E.N.. Correction of erroneous and ectopic beats using a point process adaptive algorithm. Conference proceedings : Annual International Conference of the IEEE Engineering in Medicine and Biology Society IEEE Engineering in Medicine and Biology Society Conference 2006b;1:3373–3376.

Barbieri, R., Chen, Z., Brown, E.N.. Assessment of hippocampal and autonomic neural activity by point process models. Conference proceedings : Annual International Conference of the IEEE Engineering in Medicine and Biology Society IEEE Engineering in Medicine and Biology Society Conference 2008;2008:3679.

Barbieri, R., Frank, L.M., Nguyen, D.P., Quirk, M.C., Solo, V., Wilson, M.A., Brown, E.N.. Dynamic analyses of information encoding in neural ensembles. Neural Comput 2004b;16(2):277–307.

Barbieri, R., Matten, E.C., Alabi, A.A., Brown, E.N.. A point-process model of human heartbeat intervals: new definitions of heart rate and heart rate variability. Am J Physiol Heart Circ Physiol 2005a;288(1):H424–35.

Barbieri, R., Wilson, M.A., Frank, L.M., Brown, E.N.. An analysis of hippocampal spatio-temporal representations using a Bayesian algorithm for neural spike train decoding. Neural Systems and Rehabilitation Engineering, IEEE Transactions on 2005b;13(2):131–136.

Bézivin, J., Muller, P.A.. The unified modeling language. UML '98 : beyond the notation : First International Workshop, Mulhouse, France, June 3-4, 1998 : selected papers. Springer Verlag, 1999.

Boashash, B.. Estimating and interpreting the instantaneous frequency of a signal. I. Fundamentals. In: Proceedings of the IEEE. 1992a. p. 520–538.

Bokil, H., Andrews, P., Kulkarni, J.E., Mehta, S., Mitra, P.P.. Chronux: a platform for analyzing neural signals. J Neurosci Methods 2010;192(1):146–151.

Booch, G., Rumbaugh, J., Jacobson, I.. The unified modeling language user guide. Addison-Wesley Professional, 2005.

Brown, E.N., Barbieri, R.. A study of probabilistic models for characterizing human heart beat dynamics in autonomic blockade control. Acoustics 2008;:481–484.

Brown, E.N., Barbieri, R., Ventura, V., Kass, R.E., Frank, L.M.. The time-rescaling theorem and its application to neural spike train data analysis. Neural Comput 2002;14(2):325–346.

Brown, E.N., Kass, R.E., Mitra, P.P.. Multiple neural spike train data analysis: state-of-the-art and future challenges. Nat Neurosci 2004;7(5):456–461.

Brown, E.N., Meehan, P.M., Dempster, A.P.. A stochastic differential equation model of diurnal cortisol patterns. Am J Physiol Endocrinol Metab 2001a;280(3):E450–61.

Bullmore, E., Sporns, O.. Complex brain networks: graph theoretical analysis of structural and functional systems. Nature reviews 2009;10(3):186–198.

Chen, Z., Brown, E.N., Barbieri, R.. A Point Process Approach to Assess Dynamic Baroreflex Gain. Comput Cardiol 2008;35:805–808.

Chen, Z., Brown, E.N., Barbieri, R.. Assessment of autonomic control and respiratory sinus arrhythmia using point process models of human heart beat dynamics. IEEE Trans Biomed Eng 2009b;56(7):1791–1802.

Chen, Z., Brown, E.N., Barbieri, R.. Characterizing nonlinear heartbeat dynamics within a point process framework. IEEE Trans Biomed Eng 2010c;57(6):1335–1347.

Chen, Z., Purdon, P.L., Brown, E.N., Barbieri, R.. A differential autoregressive modeling approach within a point process framework for non-stationary heartbeat intervals analysis. Conference proceedings : Annual International Conference of the IEEE Engineering in Medicine and Biology Society IEEE Engineering in Medicine and Biology Society Conference 2010d;2010:3567–3570.

Chen, Z., Purdon, P.L., Harrell, G., Pierce, E.T., Walsh, J., Brown, E.N., Barbieri, R.. Dynamic assessment of baroreflex control of heart rate during

induction of propofol anesthesia using a point process method. Ann Biomed Eng 2011a;39(1):260–276.

Chen, Z., Putrino, D.F., Ba, D.E., Ghosh, S., Barbieri, R., Brown, E.N.. A regularized point process generalized linear model for assessing the functional connectivity in the cat motor cortex. Conference proceedings : Annual International Conference of the IEEE Engineering in Medicine and Biology Society IEEE Engineering in Medicine and Biology Society Conference 2009e;2009:5006–5009.

Cohen, L., Lee, C.. Instantaneous bandwidth for signals and spectrogram. In: Acoustics, Speech, and Signal Processing, 1990. ICASSP-90., 1990 International Conference on. 1990. p. 2451–2454.

Czanner, G., Eden, U.T., Wirth, S., Yanike, M., Suzuki, W., Brown, E.N.. Analysis of between-trial and within-trial neural spiking dynamics. J Neurophysiol 2008;99(5):2672–2693.

Daley, D.J., Vere-Jones, D.. An introduction to the theory of point processes. New York: Springer-Verlag, 1988.

Dempster, A.P., Laird, N.M., Rubin, D.B.. Maximum Likelihood from Incomplete Data via the EM Algorithm. Journal of the Royal Statistical Society Series B (Methodological) 1977;39(1):1–38.

Eden, U.T., Frank, L.M., Barbieri, R., Solo, V., Brown, E.N.. Dynamic analysis of neural encoding by point process adaptive filtering. Neural Comput 2004a;16(5):971–998.

Eden, U.T., Truccolo, W., Fellows, M., Donoghue, J.P., Brown, E.N.. Reconstruction of hand movement trajectories from a dynamic ensemble of spiking motor cortical neurons. Conference proceedings : Annual International Conference of the IEEE Engineering in Medicine and Biology Society IEEE Engineering in Medicine and Biology Society Conference 2004b;6:4017–4020.

Egert, U., Knott, T., Schwarz, C., Nawrot, M.P., Brandt, A., Rotter, S., Diesmann, M.. MEA-Tools: an open source toolbox for the analysis of multi-electrode data with MATLAB. J Neurosci Methods 2002;117(1):33–42.

Frank, L.M., Brown, E.N., Stanley, G.B.. Hippocampal and cortical place cell plasticity: implications for episodic memory. Hippocampus 2006;16(9):775–784.

Frank, L.M., Eden, U.T., Solo, V., Wilson, M.A., Brown, E.N.. Contrasting patterns of receptive field plasticity in the hippocampus and the entorhinal cortex: an adaptive filtering approach. J Neurosci 2002;22(9):3817–3830.

Frank, L.M., Stanley, G.B., Brown, E.N.. Hippocampal plasticity across multiple days of exposure to novel environments. J Neurosci 2004;24(35):7681–7689.

Georgopoulos, A.P., Schwartz, A.B., Kettner, R.E.. Neuronal population coding of movement direction. Science (New York, NY 1986;233(4771):1416–1419.

Gerstein, G.L., Kiang, N.S.. An approach to the quantitative analysis of electrophysiological data from single neurons. Biophys J 1960;1:15–28.

Goldberg, D.H., Victor, J.D., Gardner, E.P., Gardner, D.. Spike Train Analysis Toolkit: Enabling Wider Application of Information-Theoretic Techniques to Neurophysiology. Neuroinformatics 2009;7(3):165–178.

Haslinger, R., Pipa, G., Brown, E.N.. Discrete time rescaling theorem: determining goodness of fit for discrete time statistical models of neural spiking. Neural Comput 2010;22(10):2477–2506.

Johnson, A., Kotz, S.. Distributions in Statistics: Continuous Univariate Distributions. New York: Wiley, 1970.

Kalman, R.. A new approach to linear filtering and prediction problems . Journal of Basic Engineering 1960a;82(1):35–45.

Kim, S., Putrino, D.F., Ghosh, S., Brown, E.N.. A Granger causality measure for point process models of ensemble neural spiking activity. PLoS Comp Biol 2011;7(3):e1001110.

Krumin, M., Shoham, S.. Multivariate autoregressive modeling and granger causality analysis of multiple spike trains. Computational Intelligence and Neuroscience 2010;2010.

Lewis, P.A.W., Shedler, G.S.. Simulation methods for Poisson processes in nonstationary systems. In: WSC '78: Proceedings of the 10th conference on Winter simulation. IEEE Press; 1978. .

Liu, X.q., Wu, X., Liu, C.. SPKtool: An open source toolbox for electrophysiological data processing. CORD Conference Proceedings 2011;1:854–857.

McCullagh, P., Nelder, J.A.. Generalized linear models. London; New York: Chapman and Hall, 1989.

Meier, R., Egert, U., Aertsen, A., Nawrot, M.P.. FIND–a unified framework for neural data analysis. Neural Netw 2008;21(8):1085–1093.

Moran, D.W., Schwartz, A.B.. Motor cortical representation of speed and direction during reaching. J Neurophysiol 1999;82(5):2676–2692.

Ogata, Y.. On Lewis' simulation method for point processes. Information Theory, IEEE Transactions on 1981;27(1):23–31.

O'Keefe, J.. Place units in the hippocampus of the freely moving rat. Experimental neurology 1976;51(1):78–109.

O'Keefe, J., Conway, D.H.. Hippocampal place units in the freely moving rat: why they fire where they fire. Experimental brain research Experimentelle Hirnforschung Experimentation cerebrale 1978;31(4):573–590.

O'Keefe, J., Dostrovsky, J.. The hippocampus as a spatial map. Preliminary evidence from unit activity in the freely-moving rat. Brain Res 1971;34(1):171–175.

Palm, G., Aertsen, A.M.H.J., Gerstein, G.L.. On the significance of correlations among neuronal spike trains. Biological Cybernetics 1988;59(1):1–11.

Phillips, M., Lewis, L., Constantine-Paton, M., Brown, E.N.. A model-based framework for the analysis of miniature post-synaptic currents. In: BMC Neuroscience. San Antonio, TX, USA; 2010. p. 193.

Pipa, G., Chen, Z., Neuenschwander, S., Lima, B., Brown, E.N.. Efficient spike encoding for mapping visual receptive fields. In: Computational and Systems Neuroscience (COSYNE'09). Salt Lake City, UT, USA; 2009. .

Pipa, G., Chen, Z., Neuenschwander, S., Lima, B., Brown, E.N.. Mapping of visual receptive fields by tomographic reconstruction. Neural Computation (submitted) 2011;.

Rauch, H., Tung, F., Striebel, C.. Maximum Likelihood Estimates of Linear Dynamic Systems. AIAA Journal 1965;3(8):1445–1450.

Schwarz, G.. Estimating the Dimension of a Model. Ann Statist 1978;6(2):461–464.

Srinivasan, L., Eden, U.T., Mitter, S.K., Brown, E.N.. General-purpose filter design for neural prosthetic devices. J Neurophysiol 2007;98(4):2456–2475.

Srinivasan, L., Eden, U.T., Willsky, A.S., Brown, E.N.. A state-space analysis for reconstruction of goal-directed movements using neural signals. Neural Comput 2006;18(10):2465–2494.

Stam, C.J., Reijneveld, J.C.. Graph theoretical analysis of complex networks in the brain. Nonlinear Biomed Phys 2007;1(1):3–3.

Temereanca, S., Brown, E.N., Simons, D.J.. Rapid changes in thalamic firing synchrony during repetitive whisker stimulation. J Neurosci 2008;28(44):11153–11164.

Temereanca, S., Simons, D.J.. Local field potentials and the encoding of whisker deflections by population firing synchrony in thalamic barreloids. J Neurophysiol 2003;89(4):2137–2145.

Thomson, D.. Spectrum estimation and harmonic analysis. In: Proceedings of the IEEE. 1982. p. 1055–1096.

Truccolo, W., Eden, U.T., Fellows, M.R., Donoghue, J.P., Brown, E.N.. A point process framework for relating neural spiking activity to spiking history, neural ensemble, and extrinsic covariate effects. J Neurophysiol 2005;93(2):1074–1089.

Characterization Of Motor Neuronal Responses During Locomotion Under Elastic Load and BMI Conditions

Abstract

While much is known about the anatomy and neural regions involved in the regulation of walking, the realtime adaptations required to handle the ever-changing environment are not well understood. To elucidate the neural mechanisms of locomotion, we studied how task relevant information (e.g. positions, velocities, and forces) modulate single unit neural activity from hindlimb/trunk region of the rat motor cortex during adaptations to robot-applied elastic loads and closed-loop brain-machine-interface (BMI) control during treadmill locomotion. Using the Point Process-Generalized Linear Model (PP-GLM) statistical framework we systematically tested parametric and non-parametric point process models of increased complexity for 573 individual neurons recorded over multiple days in six animals. The developed statistical model captures within gait-cycle modulation, load-specific modulation, and intrinsic neural dynamics. Our proposed model accurately describes the firing statistics of 98.5% (563/573) of all the recorded units and allows characterization of the neural receptive fields associated with gait phase and loading force. Understanding how these receptive fields change during training and with experience will be central to developing rehabilitation strategies that optimize motor adaptations and motor learning.

Introduction

Ambulation crucial activity of daily living (Quinn et al., 2011, Collin et al., 1988). Unfortunately, many diseases and injuries can affect an individuals' ability to walk independently. For example, in the US alone, there are approximately 800,000 new

cases of stroke each year and over 30% of ischemic stroke survivors are unable to walk at six months without assistance (Lloyd-Jones et al., 2009). According to one study by the Christopher & Dana Reeve Foundation, it is estimated that approximately 1.9% of the U.S. population, or some 5,596,000 people, currently suffer from some form of paralysis - largely due to stroke (29%), spinal cord injury (23%), and multiple sclerosis (17%). Limb loss, resulting from trauma or amputation, is another major contributor to loss of ambulation. In the US alone, over 1.7 million people are estimated to have lost a limb (Ziegler-Graham et al., 2008).

Brain machine interfaces (BMIs) hold promise for the restoration of gait. Over the last 15 years there has been a surge in the number of successful applications of BMIs for the control of reaching (Chapin et al., 1999, Velliste et al., 2008, Black et al., 2003). Numerous investigators have recently begun to apply techniques to the lower extremity (Presacco et al., 2011, Fitzsimmons et al., 2009). Current approaches have suffer from major problems such as the constant need to recalibrate(Carmena, 2012). Additionally, in order to make BMI systems widely clinically viable, significant improvements in reliability (lifetime usability of the interface) and performance (achieving control and dexterity comparable to natural movements) need to be achieved (Orsborn et al., 2012). One main limitation of current approaches is based on the limited knowledge of how information about a task is represented by an ensembles of neurons. Researcher currently "bypass" this problem by treating the relationship between neural firing and variables of interest as a "black box" and using regression based methods to obtain linear predictors that can be used to decode movement variables in real-time (Carmena et al., 2003, Presacco et al., 2011, Fitzsimmons et al., 2009, Black et al., 2003). Developing an understanding of information processing at the individual neuron and population level (see Moran and Schwartz (1999), Georgopoulos et al. (1986)) is likely to lead to insights about the control of locomotion in health and will allow for improved information extraction from neural ensembles. Deriving models of neural function that capture how task-relevant information is represented together with an understanding of how these representations change with time, experience, and pathology will help address the current limitations of BMI reliability, performance, and calibration.

In an effort to elucidate the neural mechanisms involved during a closed loop BMI task, we studied how task relevant information (e.g. positions, velocities, and forces) modulate single unit neural activity from hindlimb/trunk region of the rat motor cortex during adaptations to robot-applied elastic loads and closed-loop brain-machine-interface (BMI) control during treadmill locomotion. Using the point process - GLM framework we apply simple parametric models to the neural activity in order to determine the range of neural behaviors present in a population of cells being recorded. From the observed behaviors we posit a single paramet-

ric model that is able to capture the activity of 558/573 cells. Observation of how parameters in this model change over each experimental condition yields insight into the types of changes that occur over the course of minutes and days. Importantly, the proposed model structure is able to capture neural firing dynamics even in the presence of short and long term plasticity. The development of models that capture relevant neural dynamics and information processing in the face of neural plasticity will serve as a stepping stone towards developing BMIs that can track the relevant changes in parameters and thus remain effective of the course of days and hopefully even years.

Methods

Experiment Details

Animals and Surgical Procedures

The experimental setup used herein has been previously described in detail (Song and Giszter, 2011). Briefly, seven adult Sprague Dawley rats, weighing 250-300g, were used in these experiments. Care and treatment of the animals conformed to protocols approved by the University Laboratory Animal Resources and Institutional Animal Care and Use Committee of the College of Medicine of Drexel University.

Two implantations were performed in each rat consecutively in a single surgery. A pelvic orthosis implantation was performed first, followed by a cortical recording electrode implantation. After anesthesia induction, pelvic implants were placed under the bone of the pelvis on each side separately. The sides of the implant were pressed together as tightly as possible without bone trauma and fastened with screws. Finally, epoxy cement (J-B Weld) was applied to the joint were the pelvic implant parts were conjoined to fix the structure. This made it rigid and prevented any displacement as the animal moved after screw release. Implants integrated with the pelvic bone and provided a rigid frame for force application. This setup ensured that the phantom robot (Phantom, SensAble Technologies) was able to apply forces effectively and directly to the skeleton as seen in Figure 3.2.

After the pelvic implantation, the rats' heads were mounted in a stereotaxic frame and a round hole (3mm in diameter) was drilled in the skull. A tetrode array, which consisted of 6 tetrode wires positioned around a spike-shaped tungsten shaft, was implanted stereotaxically (and later verified histologically) in the hindlimb/trunk area of the motor cortex (2.0mm lateral of the midline, 1.6mm caudal to the bregma, and ~ 1.5mm in depth, to give recording sites at ~1.1 mm depth).

Neural Recordings and Spike Sorting

Neural data were recorded using a Cerebrus system (Cyberkinetics/Blackrock Microsystems) commencing 1 week after animals recovered from surgery. In each recording session, rats were first lightly anesthetized with isoflurane gas, and a unity gain preamplifier headstage (Neuralynx MS-27 micro) was connected with the tetrode array via flexible wire cables. After animals fully recovered on the treadmill surface, recordings began. Neural signals were bandpass filtered (300 Hz to 7.5 kHz) and digitized at a sampling frequency of 30 kHz. Spikes were detected on-line when above or under thresholding levels. The detected spikes could be automatically classified on-line after after setting the templates of each waveform. The on-line sorted spikes were used in the closed loop condition described below. The detected spike trains, as well as the thresholded spike waveforms, were saved for off-line analysis.

Multiple single unites were isolated off-line using a commercial off-line sorter (Plexon Neurotechnology Research Systems) using the t-distribution expectation maximization sorting from features of the tetrode waveforms (an implementation of the approach of Shoham et al. (2003). The threshold inter-spike interval for a single unit was set at > 1.6 ms. Only single units that were isolated by these criteria are presented here. Up to 24 channels of neural activity at a time in a single array could be recorded, and one or two individual cells from most wires of the tetrodes could be recorded. A total of 573 well isolated cells from seven rats recorded across 23 sessions from the M1/S1 trunk hindlimb area was used in our analysis. As there is no assurance that the spike recorded on different days were the same, we did not track cells across days. We simply isolated cells afresh each day. We treated these isolations as different cells, although some of the them had the same waveforms across days.

Robot Control and Virtual Forces

The detailed robotic system has been described previously (Giszter et al., 2005). Briefly, a Phantom 1.0 model A or T robot interacts with the rat as it walks on the treadmill. Mechanical interaction occurs though an implanted pelvic orthosis. The robot actions at the pelvis in this study were determined by the combination of two independent (stable) controllers, each of which emulates a passive viscoelastic system at any instance in time.

Baseline

During experiments termed "Baseline", the rat is allows to walk freely on the treadmill with the robot passively attached to the pelvic implant. Movement kinematics

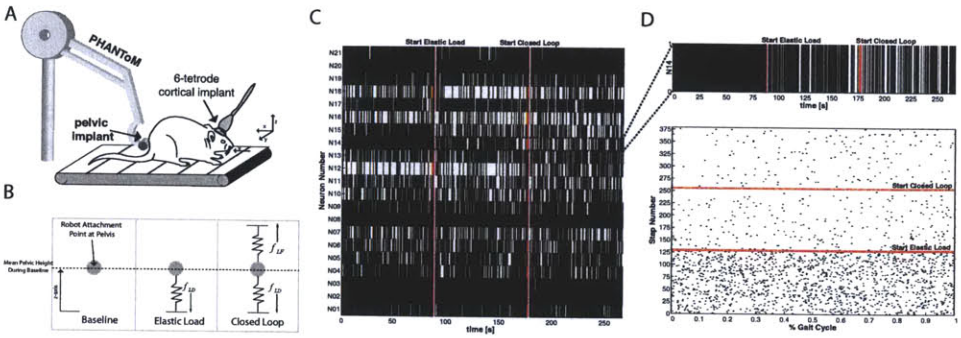

Figure 3.2: **Experimental Setup Summary. A)** Rats were trained to walk on treadmill. Pelvic kinematics and kinetics were recorded from the robot endpoint. 24 channels of neural spiking data were recorded during baseline, open loop (loaded), and closed loop trials as described. **B) Experimental Conditions. C) Sample Neural Raster. D) Single unit activity representation in terms of step number and gait phase.**

at the pelvis are recorded by the position of the robot endpoint together with 24 channels of neural activity.

Virtual Elastic Load

In experiments termed here "Virtual Elastic Load" or simply "Elastic Load," the robot tip position along the vertical z-axis was used to compute a downward elastic load according to Equation 3.2

$$f_{LD} = -K_{LD}(z - z_{LD}) \tag{3.2}$$

where the virtual load stiffness, K_{LD}, was set between 50-90 [N/m] and the load equilibrium position, z_{LD}, was set 13 mm below the mean pelvic height observed during the baseline period (see Figure 3.2 B for an illustration).

Closed-Loop

During "Closed-Loop" experiments, a virtual lift field is attached to pelvis with an equilibrium point, z_{LF}, located 50 mm above the mean pelvic height observed during normal the baseline period, e.g.

$$f_{LF} = -K_{LF}(z - z_{LF}) \tag{3.3}$$

Unlike the load field, the lift field stiffness was allows to be modulated by the neural activity being recorded. The actual stiffness of this lift field, K_{LF}, was computed as

$$K_{LF} = K_{LF_0} \cdot f_{spikes} \tag{3.4}$$

where the nominal stiffness, K_{LF_0}, was set between 200-450 [N/m] and f_{spikes} is the average firing rate computed across all recorded units in a moving 100 ms window (e.g. the total number of spikes observed in the previous 100ms across all channels normalized by the number of channels being recorded, C, and divided by 100 ms). More specifically

$$f_{spikes}(t) = \frac{1}{0.1 \cdot C} \sum_{c=1}^{C} \left(N^c(t) - N^c(t-.1)\right) \tag{3.5}$$

where $N^c(t)$ is a counting process denoting the sum of all spike events up to time t in the c^{th}channel. The total force applied to the pelvis at time t during Closed-Loop experiments was

$$f_T = f_{LD}(t) + f_{LF}(t). \tag{3.6}$$

Experimental Design

The rats were trained to walk on the treadmill. The robot position and force data were recorded simultaneously at 1 kHz for off-line analysis, together with synchronized recordings of neural activity (at 30 kHz). The speed of the treadmill, which was adjusted depending on the normal preferred walking speed of individual rats was set in the range of 0.1-0.14 m/s, within which all rats preferred speed lay. One daily experimental session was divided into three trials: (1) Baseline Trial, in which the rats walked on the treadmill with the robotic tip attached to the pelvic implant but without any forces being applied; (2) Virtual Elastic Load trial, in which an elastic load force, f_{LD}, was applied according to Equation 3.2; (3) Closed-Loop trial, in which a neural driven elastic lift force, f_{LF}, was applied in combination with the above elastic load force, f_{LD}, according to Equation 3.6. The speed of the treadmill was held constant throughout. The experimental setup and protocol at shown in Figure 3.2 A and B respectively. Each session consisted of three 2 min trials of treadmill walking (~120 steps) and 5 min intervals of rest that occurred between each trial. In total, 23 sessions or data sets were obtain in seven normal rats during the recording sessions. Figure 3.2 C shows one sample data set consisting of 21 channels of neural activity recorded over the three trial types. Note that for simplicity the 5 minute rest intervals are not included in the raster. To understand the step to step changes in the neural firing, we transformed each neural spike train

time series as shown in Figure 3.2 D. The step cycle was derived from the robot position parameter p_y, which corresponds to pelvic lateral motion. This movement is precisely synchronized with step phase during normal walking. To identify step cycles from interactive robot motion, the parameter p_y was first bandpass filtered (2nd order Butterworth, passband 0.3 -5Hz). One step cycle was then identified by two consecutive peaks or valleys of the filtered p_y. In the work herein we chose the identify step cycles by consecutive minima in p_y, thus our gait cycle start (0% or 0 degrees of gait phase) corresponds to toe off on the right side and 50% or 180% of gait phase corresponds to toe off on the left. Song and Giszter (2011) showed that this estimate of step phase matched well with foot marker motion and toe off when checked with the video tracking system (95% step cycles from video match with step cycles from robot with an accuracy of 0.01 step cycle).

Our rationale for this experimental design was that rats will adapt their locomotion during the Elastic Load condition, thus expressing some differences in neural activity compared to Baseline. In the Closed-Loop condition, the lift force was provided in parallel with the elastic load. The rat must adapt to both in order to continue locomotion. Moreover, we wished to examine, it the rats would be able to modulate neural firing in order to compensate for the elastic load.

Point Process - Generalized Linear Model Framework

Unlike prior analysis of this data set in Song and Giszter (2011), we treat single unit neural activity as a stochastic point process. Briefly, a point process is completely characterized by its Conditional Intensity Function (CIF) (Daley and Vere-Jones, 1988) defined as

$$\lambda(t|H_t) \triangleq \lim_{\Delta \to 0} \frac{P(N(t+\Delta) - N(t) = 1 \mid H_t)}{\Delta} \tag{3.7}$$

where H_t is all the history information from 0 up to time t and $N(t)$ is a counting process denoting the sum of all spike events up to time t. The conditional intensity function can be considered a generalization of the "rate" for a homogeneous Poisson process. For any finite Δ, the product $\lambda(t|H_t)\Delta$ is approximately equal to the probability of a single spike in the interval $(t, t+\Delta]$ given the firing history up to time t. We term this probability, p_{spike}. Because in any time interval, a spike can only be present or absent, $1 - \lambda(t|H_t)\Delta$ approximates the probability of not observing a spike in $(t, t+\Delta]$ given the firing history up to time t. We term this probability $q_{spike} = 1 - p_{spike}$. The ratio p_{spike}/q_{spike} is typically referred to as the "event odds" or simply the "odds" for a binomial stochastic process and captures the intuitive notion of the relative probability of observing the presence of an event compared to its absence.

Modeling the distribution of the random variable $\lambda(t|H_t)\Delta$ as a member of the exponential family allows the use of the Generalized Linear Model (GLM) framework (McCullagh and Nelder, 1989)to fit statistical models for the conditional intensity function. Here in we model $\lambda(t|H_t)\Delta$ using a Binomial GLM regression model where we write the inverse of the logistic function, $\text{logit}(\lambda(t|H_t)\Delta)$, as a linear function of covariates, e.g.

$$\text{logit}(\lambda(t_n|H_{nj})\Delta) = x_n^T\beta \iff \lambda(t_n|H_{t_n})\Delta = \frac{\exp(x_n^T\beta)}{1+\exp(x_n^T\beta)} \tag{3.8}$$

where x_n^T is the n^{th} row of the design matrix X and β is the vector of model parameters to be estimated. The spike indicator function, ΔN_n, is taken as the observation, termed y_n. That is $y_n = \Delta N_n \sim \lambda(t_n|H_{t_n})\Delta = \frac{\exp(x_n^T\beta)}{1+\exp(x_n^T\beta)}$. The inverse of the logistic function can also be though of as the logarithm of the odds of observing a spike in $(t, t+\Delta]$ given the firing history up to time t. That is,

$$logit(\lambda\Delta) = log\left(\frac{\lambda\Delta}{1-\lambda\Delta}\right) = log\left(\frac{p_{spike}}{q_{spike}}\right) \tag{3.9}$$

where p_{spike} and q_{spike} have been defined previously. Thus $exp(x_n^T\beta)$ is a measure of instantaneous odds of observing a spike given the covariates, x_n, and the parameters, β. Truccolo et al. (2005) provides an excellent summary of the Point Process - Generalized Linear Model (PP-GLM) framework.

Goodness of Fit

AIC (Akaike, 1973), BIC (Schwarz, 1978), and time-rescaling theorem (Brown et al., 2002) were used to assess how well point process models fit the data. In particular, we used the Kolmogorov-Smirnov statistic, defined as the largest deviation between the empirical and actual CDFs of the rescaled spike times from the time rescaling theorem to determine if a model adequately describes the data. Specifically, we accept a model as "adequate" if its K-S statistics falls within the 95% confidence bounds (Johnson and Kotz, 1970). Application of the time-rescaling theorem to sampled data produces some artifacts within K-S plots since the actual spike times could have occurred anywhere within the finite-sized time bins. These artifacts are addressed using the discrete time rescaling theorem (Haslinger et al., 2010).

Point Process Models for Single Unit Activity

In order to investigate the range of single unit activity within the 573 cells recorded, we proposed parametric models of increased complexity and used the time-rescaling

theorem and K-S statistic to determine if the proposed model provided an "adequate" description of the observed firing activity in a statistical sense. Once an adequate model was obtained for a single unit, it was excluded from further analysis.

Model 1 - Homogenous Poisson Model

The simplest model for the activity of a given single unit is one where the firing rate is constant and unrelated to the any of the experimental conditions or covariates. This corresponds to modeling each spike train as the result of a Poisson process with constant rate parameter, μ_0, e.g.

$$\text{logit}\left(\lambda\left(t_n|H_{t_n}\right)\Delta\right) = \mu_0 \tag{3.10}$$

where t_n refers to un-normalized real-time or normalized time within a gait cycle. All subsequent models use t_n as normalized time within a gait cycle. Model 1 was applied first to all of the 573 cells with respect to actual experimental time and cells that were well described by this model were not included in the subsequent analysis. This was done to avoid introduction of any artificial structure into the normalized spike trains as purely a result of the normalization process.

Model 2 - Constant Baseline with History Dependence

Current spiking activity is also related to its past activity, reflecting biophysical properties such as refractoriness and rebound excitation or inhibition (Hille, 2001, Wilson, 1999, Keat et al., 2001). Thus, Model 1 from Equation 3.10 was augmented to allow prior spiking activity to modulate the current probability of firing, e.g.

$$\text{logit}\left(\lambda\left(t_n|H_{t_n}\right)\Delta\right) = \mu_0 + \sum_{q=1}^{Q} \gamma_q \Delta N_k\left(t_n - t_{q-1}, t_n - t_q\right) \tag{3.11}$$

where t_n refers to normalized time within a gait cycle, $\Delta N\left(t - t_{q-1}, t - t_q\right)$ is the total number of spikes that occurred in the time interval $[t - t_{q-1}, t - t_q)$, and Q is the number of history windows to be determined via model selection. The time windows are defined such that $t_0 = 0, t_{32} = 1$, and t_q for $1 < j < 31$ are logarithmically spaced between 0 and 1. To determine the best value of Q, all cells that were not well described by Model 1 were fit by Model 2 with the value of Q ranging from 1 to 32 and the AIC, BIC, and K-S statistics computed for every cell and for each fit. Analysis of the median and mean of these statistics across all cells were compared

for each value of Q. The value of Q that led to the minimum value across the information criteria was selected as optimum, and termed $\hat{Q}$. All subsequent models use this value of $\hat{Q}$ for the total number of history window times. Note that $\hat{Q}$ window times corresponds to $\hat{Q}-1$ history windows.

Model 3 - Condition Dependent Background Firing Rate with History

Having accounted for neurons whose dynamics were well described as unrelated to the task (Model 1) or modulated by their previous firing history (Model 2), we sought to identify any neurons whose activity was Poisson within any condition, but whose rate varied across conditions, e.g.

$$\text{logit}\left(\lambda\left(t_n|H_t\right)\Delta\right) = \mu_{COND} + \sum_{q=1}^{\hat{Q}} \gamma_q \Delta N_k\left(t_n - t_{q-1}, t_n - t_q\right) \tag{3.12}$$

$$\mu_{COND} = \begin{cases} \mu_{BL} & t_n \in [0, T_{BL}] \\ \mu_{LD} & t_n \in (T_{BL}, T_{LD}] \\ \mu_{CL} & t_n \in (T_{LD}, T_{CL}] \end{cases} \tag{3.13}$$

where the history dependence terms, γ_q, were required to be the same across all three experimental conditions, and T_{BL}, T_{LD}, and T_{CL} indicate the end of Baseline, Elastic Load, and Closed-Loop conditions respectively.

Model 4 - Peri-Stimulus Time Histogram with History

Next we considered models that capture the dynamics of neurons that showed firing rate modulation within a step but that showed no changes across conditions. In order to avoid constraining the form of the within-step modulation, we used a peri-stimulus time histogram (PSTH) method to estimate the within-step effect. PSTH histograms are used to visualize the rate and timing of neuronal spike discharges in relation to an external stimulus or event. To make a PSTH, a spike train recorded from a single neuron is aligned with the onset, or a fixed phase point, of an identical repeatedly presented stimulus. The aligned sequences are superimposed in time and then combined to construct a histogram (Gerstein and Kiang, 1960, Palm et al., 1988). In our case, the external stimulus is the beginning of a step.

According to Czanner et al. (2008), the PSTH is a special case of the conditional intensity function defined by the following GLM

$$\text{logit}\left(\lambda\left(k, t_n|\theta\right)\Delta\right) = \sum_{r=1}^{R} \theta_r g_r\left(n\Delta\right) + \sum_{q=1}^{\hat{Q}} \gamma_q \Delta N_k\left(t_n - t_{q-1}, t_n - t_q\right) \tag{3.14}$$

for $k = 1,...,K$ and $n = 1,...,N$. Here k is the trial (step) number, n the temporal index corresponding the time within a step t_n, and

$$g_r(n\Delta) = \begin{cases} 1 & \text{if } n = (r-1)NR^{-1}+1,...,rNR^{-1} \\ 0 & \text{otherwise} \end{cases} \tag{3.15}$$

are the unit pulse functions in the observation interval $(0,T]$ (equivalently $[1,N\Delta]$). Note that the resolution of the PSTH estimate is governed by the number of time bins R. Additionally, note that this conditional intensity function is the same for all trials $k = 1,..,K$ and thus satisfies the invariance across conditions that we sought. Herein we always used $R = 10$.

Model 5 - State Space GLM Lastly, we wanted to identify neurons that showed within-step and across-condition dynamics without constraining the form of the dynamics. To achieve this, we applied the State Space GLM (SS-GLM) framework of Czanner et al. (2008) which extends the standard PSTH to allow for across-step or across-condition dependence. Briefly the SS-GLM framework proposes that the neural conditional intensity function be modeled as

$$\text{logit}\left(\lambda\left(k,n\Delta|\theta\right)\Delta\right) = \sum_{r=1}^{R} \theta_{k,r} g_r(n\Delta) + \sum_{q=1}^{\hat{Q}} \gamma_q \Delta N_k\left(t_n - t_{q-1}, t_n - t_q\right) \tag{3.16}$$

where k is the current step index and $\Delta N_k(t_A,t_B)$ equals the total number of spikes observed in the interval $(t_A,t_B]$ of the k^{th} trial. The stochastic trial-to-trial dependence between the parameters $\theta_k = \left[\begin{array}{cccc} \theta_{k,1} & \ldots & \theta_{k,r} & \ldots \end{array}\ \theta_{k,R}\right]$ is described by the random walk model

$$\theta_k = \theta_{k-1} + \varepsilon_k \tag{3.17}$$

for $k = 1,...,K$, where K is the total number of trials, ε_k is an R-dimensional Gaussian random vector with mean 0 and unknown covariance matrix Σ. The initial vector θ_0 is also assumed to be unknown. Because the parameters θ_k and γ_j of the GLM and the covariance parameter, Σ, of the random walk model are unknown, an iterative Expectation-Maximization algorithm (Dempster et al., 1977) is employed to estimate them. Herein we always used $R = 10$.

Parametric Model

Application of Models 1-5, suggested that the range of behaviors observed in these experiments were well captured by a model with the following properties: (1) a

condition-dependent background firing rate, μ_{COND}; (2) a within-step sinusoidal variation in firing rate; (3) load-magnitude dependent modulation; and (4) prior spiking activity modulation. The following parametric model captures aforementioned properties:

$$\begin{aligned}\text{logit}\left(\lambda\left(k,t_n|H_{t_n}\right)\Delta\right) &= \mu_{COND} + \alpha_{1_{COND}} cos\left(\phi_y\left(t_n\right)\right) + \alpha_{2_{COND}} sin\left(\phi_y\left(t_n\right)\right) \\ &\quad + \alpha_{3_{COND}} f_{LD}\left(t_n\right) + \sum_{q=1}^{\hat{Q}} \gamma_q \Delta N_k\left(t_n - t_{q-1}, t_n - t_q\right) \quad (3.18)\end{aligned}$$

where all parameters are held constant within an experimental condition but allowed to vary between conditions so that the relative effects of the conditions can be explored. Here ϕ_y ranges from 0 at the beginning of a step to 2π at the end of the step and is denoted by the subscript y since each step is identified from the robot tip position, p_y. The phase angle of maximal firing is determined by taking the derivative of Equation 3.18 with respect to ϕ_y and equals

$$\phi_{y_{max}COND} = tan^{-1}\left(\frac{\alpha_{2_{COND}}}{\alpha_{1_{COND}}}\right) \quad (3.19)$$

We term this angle the "preferred gait phase" or "preferred direction" of a cell consistent with the terminology applied other motor cortical cells that exhibit direction selectivity (see Moran and Schwartz, 1999, Georgopoulos et al., 1986 for example). To quantify changes across the entire population of neurons, we report the median values of the preferred directions under each of the three experimental conditions within a trial. The 95% confidence intervals for the medians are computed using Monte Carlo methods.

Receptive Field Reconstruction From Conditional Intensity Function Models

The parametric model proposed in Equation 3.18 can be used to reconstruct the receptive fields of individual cells as a function of load magnitude, f_{LD}, and gait phase, ϕ_y. To generate a receptive field for the c^{th}cell, we solve Equation 3.18 for λ^c. Note that λ^c is a a function of the current condition, $COND$, the current gait phase, ϕ_y, the load magnitude, f_{LD}, and the prior spiking activity, ΔN_k, e.g.

$$\lambda^c\left(k,t_n|H_{t_n}\right) = f\left(COND, \phi_y\left(t_n\right), f_{LD}\left(t_n\right), \Delta N_k\left(t_n\right)\right) \quad (3.20)$$

Fixing t_n, the value of the current condition, $COND$, and setting $\Delta N_k = 0$, we can treat Equation 3.20 as function of the load force magnitude, f_{LD}, and the gait phase,

ϕ_y. By ranging the load magnitude from 0 to 1 and the gait phase from 0 to 2π we obtain a surface that describes how the c^{th} cell responses over a range of loads and gait phases.

Comparing Condition Effects via Odds Ratios

As mentioned in Section Equation 3.9, the binomial GLM regression model yields an estimate of the log odds as a linear function of the covariates. Given the parametric model in Equation 3.18, it is of interest to examine how load-dependent modulation, $\alpha_{3_{COND}}$, and background firing rates, μ_{COND}, change over condition. The odds ratio for the background firing rates with respect to the baseline (all other terms held fixed) is

$$OR_{\mu_{COND},\mu_{BL}} = \frac{p_{COND}/p_{BL}}{q_{COND}/q_{BL}} = exp\left(\mu_{COND} - \mu_{BL}\right) \Leftrightarrow \log\left(OR_{\mu_{COND},\mu_{BL}}\right) = \mu_{COND} - \mu_{BL} \tag{3.21}$$

and between the Load and Closed-Loop condition

$$\log\left(OR_{\mu_{CL},\mu_{LD}}\right) = \mu_{CL} - \mu_{LD} \tag{3.22}$$

Similarly, the odds ratio for load-dependent modulation is

$$\log\left(OR_{\alpha_{3_{COND}},\alpha_{3_{BL}}}\right) = \log\left(OR_{\alpha_{3_{COND}},0}\right) = \left(\alpha_{3_{COND}} - 0\right) f_{LD} \tag{3.23}$$

In order to make conclusions independent of the load magnitude, we consider the change in the log odds ratio for a change in 1 unit of the load force (in Newtons). Thus, we report

$$\Delta\log\left(OR_{\alpha_{3_{COND}},\alpha_{3_{BL}}}\right) = \alpha_{3_{COND}} \tag{3.24}$$

and the corresponding change in the log odds ratio from the Load to the Closed-Loop condition

$$\Delta\log\left(OR_{\alpha_{3_{CL}},\alpha_{3_{LD}}}\right) = \alpha_{3_{CL}} - \alpha_{3_{LD}} \tag{3.25}$$

To quantify changes across the entire population of neurons, we report the median values of the aforementioned log odds ratios and change in log odds ratios per Newton. The 95% confidence intervals for the medians are computed using Monte Carlo methods.

Results

Models of Single Unit Firing Activity

Figure 3.3 A shows representative rasters for neurons that were well described by Models 1-5. Neurons well fit by Model 1 is characterized by a constant spike rate that is independent of the experimental condition and of prior spiking activity. Neurons characterized by Model 2 show a decreased propensity to fire immediately after a spike. Neurons well explained by Model 3 showed a broad range of behavior ranging from decreased firing in the Load and Closed-Loop conditions with respect to baseline or as seen in Figure 3.3 a marked increase in the firing rate during the Closed-Loop condition. Neurons that were well described by Model 4 showed sinusoidal variation in the the firing rate within the gait cycle. This type of behavior had been previously reported by numerous investigators (Armstrong and Drew, 1984b, Beloozerova and Sirota, 1993a, Song and Giszter, 2011). Lastly, Model 5 identified neurons that showed load-magnitude dependent modulation. For example, the sample neuron in Figure 3.3 was strongly inhibited by the increasing load magnitudes across both the Elastic load and Closed-Loop conditions.

History Dependence

Figure 3.3 B summarizes the changes in AIC, BIC, and K-S statistics (relative to the no-history model in Equation 3.10) as the number of history window times, Q, was increased from 1 to 32 (corresponding 1 to 31 history windows) for N=333 cells. Both AIC and K-S statistics show a minimum at 31 history windows or $Q = 32$. However, the maximum decrease in BIC was observed at $\hat{Q} = 23$, which corresponds to 16.1% of the gait cycle. We select $\hat{Q} = 23$ for all subsequent analysis.

Figure 3.4 shows the median conditional odds of spiking, $exp(\gamma_q)$, for $q = 1...23$ across all cells. The gray area encompasses the empirical 95% confidence interval for the conditional odds across all cells. Thus approximately 95% of the cell responses fell within the gray area. The short term history effect reveals that the median refractory period (defined here as the time to return to and odds ratio of 1) of the 333 cells fit by Model 2 was approximately 0.85% of the gait cycle (~5.6ms for a typical 700ms gait cycle).

Model Selection of History Dependence

Having fit the parametric model from Equation 3.18 to all 573 cells, we asked whether the number of history windows selected previously remained optimal for this model. The intuition being that in the absence of relevant covariates, maybe the

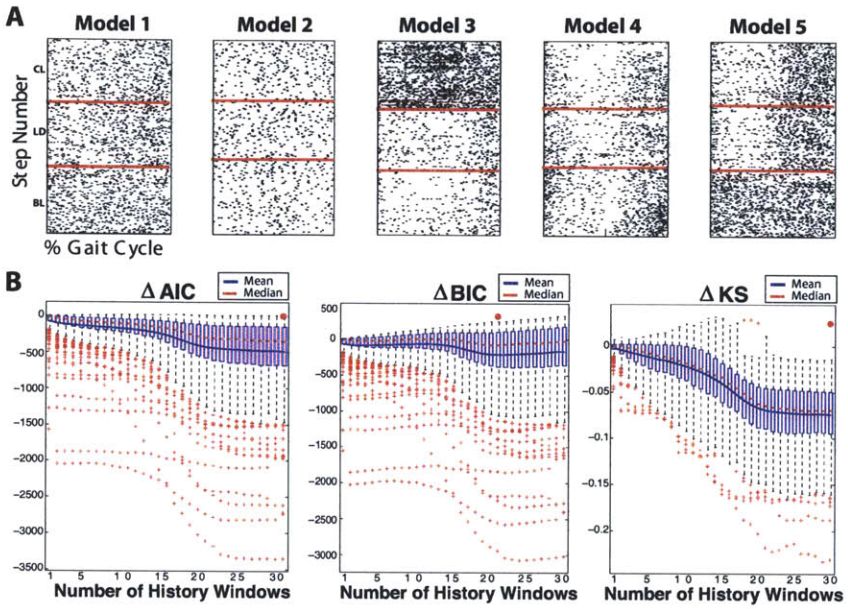

Figure 3.3: **A. Range of Neural Responses.** Representative neurons identified for each of the five proposed models in Section . **B. Model Selection via AIC, BIC, and Kolmogorov-Smirnov Statistics.** Both AIC and K-S statistics show a minimum at 31 history windows or $Q = 32$ (red dot). However, the maximum decrease in BIC was observed at $\hat{Q} = 23$, which corresponds to 16.1% of the gait cycle.

Model Type	Number of Cells Fit	Percent of Total (%)
Model 1	240	42.0
Model 2	298	52.0
Model 3	6	1.1
Model 4	8	1.4
Model 5	6	1.1
All Models	559	97.6
Equation 3.18	558	97.4

Table 3.2: **Parametric Model Fit Results.** Number of cells (out of a total of 573) that were well described by each of the models presented in Section . The last line shows how the parametric model from Equation 3.18 is able to capture the same range of dynamics as Models 1-5.

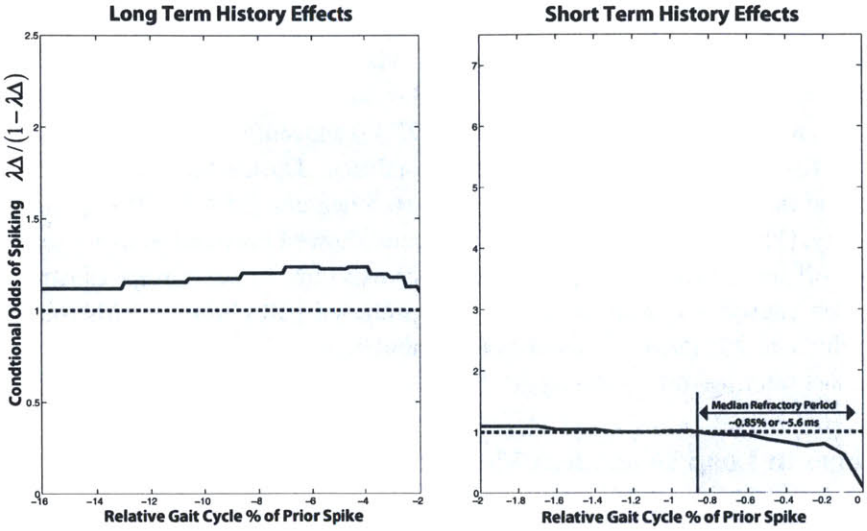

Figure 3.4: **History Effect Summary.** Visual summary of the median conditional odds of spiking given spiking history. This plot shows how prior spiking activity modulates the probability of firing at the current gait cycle phase.

history terms had been selected to be long enough to capture dynamic effects that were in fact due to the extrinsic covariates absent form the model. Interestingly, the $\hat{Q} = 23$ was once again determined to optimal in terms of yielding the largest decrease in the BIC (data not shown).

Changes in Background Firing Rates

Figure 3.5 (top) summarizes the range of background firing rates ($\lambda_{COND} = \frac{1}{\Delta}\frac{exp(\mu_{COND})}{1+exp(\mu_{COND})}$) under each of the three experimental conditions. Loading led to an increase in background firing rates across cells from 3.24 spikes per step (95% CI [2.94, 3.77]) to 4.46 spikes/step (95% CI [4.05, 5]). During the Closed-Loop conditions, cells returned towards their baseline firing rate 2.81 spikes per step (95% CI [2.27, 3.19]). Note that the median firing rate during Closed-Loop firing is not statistically different ($p>0.05$) than the median background firing rate during the Baseline Condition.

Changes in Preferred Gait Phase

Figure 3.5 (top) shows a polar histogram of the preferred gait phase as determined from Equation 3.19 across the Baseline, Elastic Load, and Closed-Loop conditions.

The median preferred phase is indicated by the solid black arrow and the 95% confidence intervals for the median (computed via Monte Carlo) are indicated by the red bands around the median. During the Baseline condition, the median preferred direction was -33 degrees (95% CI [-39.8 -27.1]) and shifted to -8.38 degrees (95% CI [-15.4, -2.4]) during the Elastic Load condition. During the Closed-Loop condition the median preferred direction was 16.5 degrees (95% CI [9.13, 25.7]). In summary, (1) during Baseline ambulation cells showed maximal to firing just prior the toe off on the right side (0 degrees); (2) exposure to the Virtual Elastic Load condition caused a significant shift in the preferred gait phase towards toe-off on the right; and (3) during Closed-Loop ambulation cells showed a preferred gait phase just after toe-off on the right.

Changes in Load Dependent Firing Rate

Elastic Load versus Baseline

Elastic loading led to increased odds ratio of background firing versus baseline (see Equation 3.21) - median log odds ratio 0.25 (95% CI [.19, .30]). This corresponds to an odds ratio of $e^{0.25} \approx 1.284$ or an increase of 28.4%. However, cells became inhibited by a unit increase in load magnitude - median change in log odds ratio per Newton of -0.25 (95% CI [-0.40, -0.08]) from Equation 3.24. This corresponds to change in odds ratio of .7788 per Newton or decrease of 22.1% from the Baseline condition.

When load-dependent changes in firing odds ratio from Equation 3.24 were compared to the log odds ratio of background firing Equation 3.21, a linear trend was observed ($R^2 = 67.2\%$). The linear slope regression coefficient was -1.92 (95% CI [-2.02 -1.80]) indicating that a one unit increase in the log odds of background firing was accompanied by a 1.9 unit decrease in the load-dependent firing odds. A decrease of 1.9 units in log odds ratio per Newton corresponds to a 85% decrease in $\Delta\log\left(OR_{\alpha_{3_{LD}},\alpha_{3_{BL}}}\right)$ ($e^{-1.9} \approx .149$). Conversely a decrease in $\log\left(OR_{\mu_{LD},\mu_{BL}}\right)$ is accompanied by a 1.9 unit increase in $\Delta\log\left(OR_{\alpha_{3_{LD}},\alpha_{3_{BL}}}\right)$, which corresponds to a 570% increase from Baseline. In summary during the Elastic Load condition, (1) the background firing rates of cells increased from baseline; (2) cells became more negatively modulated by the load force magnitude; and (3) increases in background firing rate were accompanied by an decrease in load modulation and vice-versa. Figure 3.6 A (data in blue) summarizes the changes observed between the Load condition and Baseline.

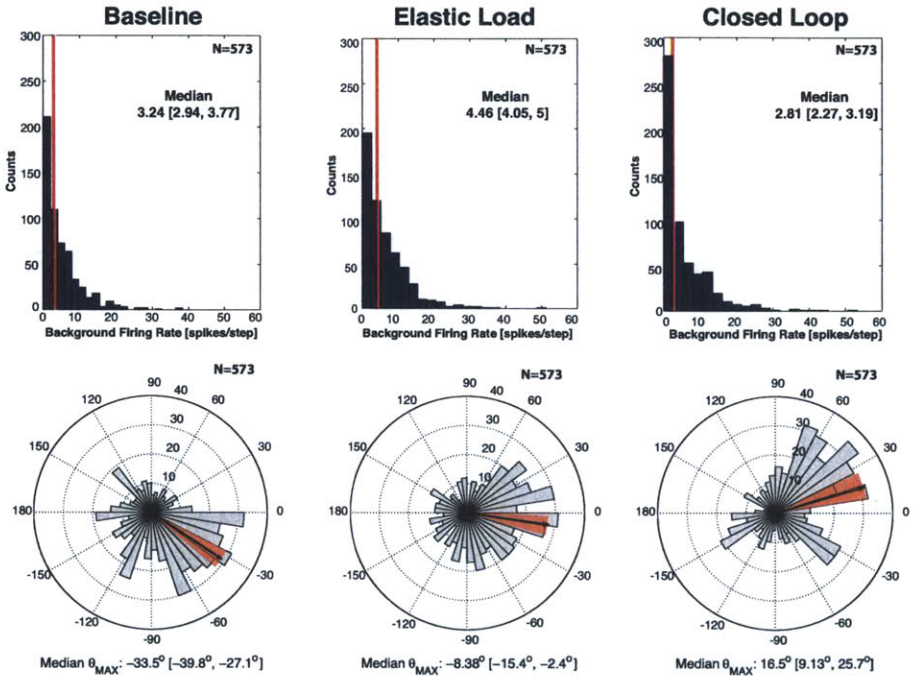

Figure 3.5: (top) **Background Firing rate distributions across conditions.** The parameter, μ_{COND}, was used to compute the background firing rate for all 573 cell across conditions. Loading led to a significant increase in the background firing rate with respect to baseline ($p<0.05$). During the Closed-Loop condition, background firing rates returned towards the median levels observed during Baseline. (bottom) **Distribution of preferred gait phases across conditions.** Polar histogram of the preferred gait phase as determined from Equation 3.19 across the Baseline, Elastic Load, and Closed-Loop conditions. The median preferred phase is indicated by the solid black arrow and the 95% confidence intervals for the median (computed via Monte Carlo) are indicated by the red bands around the median.

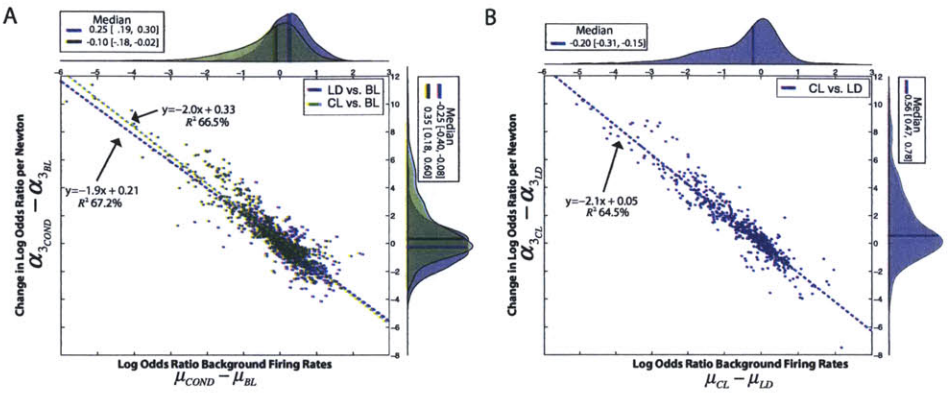

Figure 3.6: **A) Changes Load-dependent modulation vs. changes in background firing rates**

Closed-Loop versus Baseline

The Closed-Loop condition led to a decreased odds ratio of background firing (see Equation 3.21) - median log odds ratio -0.1 (95% CI [-.18, -0.02]). This corresponds to an odds ratio of .905 or a relative decrease in odds of 9.5% from Baseline. Interestingly, cells became strongly modulated by load magnitude - median change in log odds ratio per Newton of 0.35 (95% CI [0.18, 0.60]). This corresponds to a change in odds ratio of 1.42 or a an increase of 42% from Baseline.

When load-dependent changes in the firing odds ratio were compared to background firing rate changes, a linear trend was observed ($R^2 = 66.5\%$). The linear regression coefficient was -2.0 (95% CI [-2.09 -1.95]) indicating that a one unit increase in the log odds of background firing was accompanied by a 2 unit decrease in the load-dependent firing odds. A decrease of 2 units in log odds ratio corresponds to an 86% decrease in the odds with respect to baseline ($e^{-2.0} \approx 0.135$). Conversely, a unit decrease in $\log\left(OR_{\mu_{CL},\mu_{BL}}\right)$ was accompanied by a 2 unit increase increase in $\Delta\log\left(OR_{\alpha_{3_{LD}},\alpha_{3_{BL}}}\right)$ or approximately an increase on 640% increase from Baseline. In summary during the Closed-Loop condition, (1) the background firing rates of cells returned near baseline levels; (2) cells became more strongly modulated by the load force magnitude; and (3) decreases in the background firing rate were accompanied by an increase in load-dependent modulation and vice-versa. Figure 3.6 A (data in green) summarizes the changes observed between the Closed-Loop condition and Baseline.

Closed-Loop versus Elastic Load

Transition from the Elastic Load condition to the Closed-Loop condition led to a decreased odds ratio of background firing (see Equation 3.22) - median log odds ratio of -0.20 (95% CI [-0.31, -0.15]). This decrease corresponds to a relative decrease in odds of 18.1% ($e^{-0.2} \approx .819$). Additionally, there was an increase in $\Delta\log\left(OR_{\alpha_{3_{CL}},\alpha_{3_{LD}}}\right)$ from Equation 3.25 - median change in log odds ratio per Newton of 0.56 (95% CI [0.47, 0, 78]). When load-dependent changes in the firing odds ratio were compared to background firing rate changes between the Closed-Loop and Load conditions, a linear trend also observed ($R^2 = 64.5\%$). The linear regression slope coefficient was -2.10 (95% CI [-2.16, -2.05]) and indicate that cells that increased their background firing rate from the load condition to the closed loop condition did so at the expense of decreased sensitivity to load. In particular, given the negative median shift in the log odds of background firing from Load to Closed-Loop conditions, most cells became more positively modulated by changes in the load force.

In summary, transition from Elastic Load to the Closed-Loop condition led to: (1) decreased background firing rate relative to the Load condition background firing rate; (2) increased load-dependent modulation (cells became more strongly modulated by the magnitude of the load), and (3) decreases in the background firing rate were accompanied by an increase in load-dependent modulation and vice-versa. Figure 3.6 B (data in blue) summarizes the changes observed between the Closed-Loop and Elastic Load condition.

Neural Receptive Fields

Receptive fields for individual cells were constructed as described in Section . Figure 3.7 A shows the load and gait phase receptive fields of 45 simultaneously recorded neurons from animal 4 on day 1 (only Closed-Loop condition is shown for brevity). Figure 3.7 B shows the receptive fields reconstructed from the same animal on day 4. Because neurons were isolated afresh on each day, there is no guarantee of neuron correspondence across days. However, the consistency of receptive fields across days suggests that similar units were indeed isolated across the four days. If neuron are tracked over multiple days, this methodology will allow exploration of receptive field changes as function of experience and experimental condition. As an example, if neuron 2 is treated as the same in both Figure 3.7 A and B, one could say that at any given gait phase, this neuron has (1) become more highly tuned to the load magnitude (note the different scale ranges for the color codes); (2) the preferred gait phase has been maintained across days; and (3) width around the preferred gait phase has become wider with time (indicating

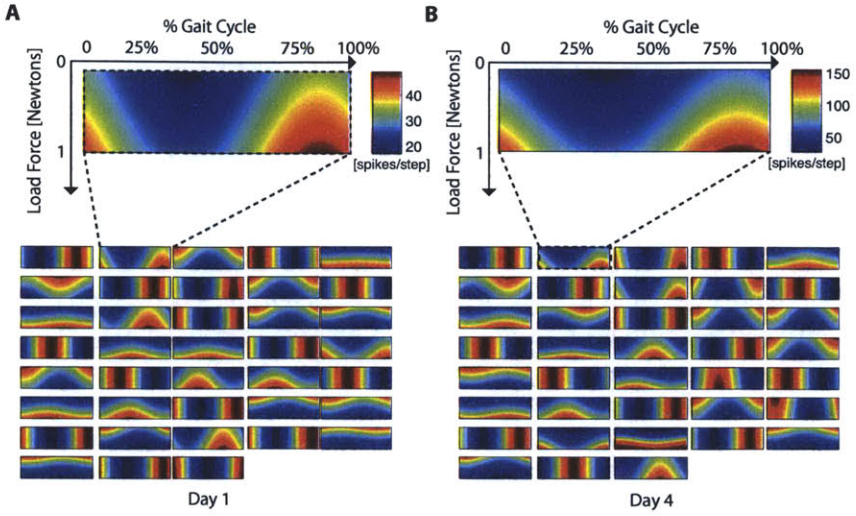

Figure 3.7: **Neural Receptive fields obtained from parametric conditional intensity function models.** The gait phase, ϕ_y was swept from $0 \rightarrow 2\pi$ and the load force, f_{LD}, from $0 \rightarrow 1$ Newton. Gait phases of $0, \pi$, and 2π correspond to $0, 50\%$, and 100% of the gait cycle respectively. phase of A) Receptive fields of 45 neurons from Animal 4 on day 1. B) Receptive fields of 45 neurons from Animal 4 on day 4.

"wider" tuning characteristics"). Detailed analysis of the changes in the receptive field structure of single neurons between conditions and across days is not included herein due to the study limitations previously mentioned.

Discussion

Using the Point Process-Generalized Linear Model (PP-GLM) statistical framework we systematically tested five simple parametric models that allowed us to identify the range of neural dynamics present across a large collection of neurons. Taken together these models were able to explain the statistical properties of 559 out of 573 neurons (97.6%). The systematic application of these models required identification of the appropriate length of self-history that most consistent with the available data. Using well-established information criteria (AIC and BIC) together with the time-rescaling theorem for point process, we determined that firing activity up to 16% of the gait cycle in the past was an important modulator of the current spiking probability and yielded the most succinct model all neurons not well fit by

homogeneous Poisson models. Characterization of the neural dynamics observed across the population also allowed us to propose a single parametric model (consisting of a background firing rate, gait phase modulation, load force modulation, and self-history) that was able to adequately describe the behavior of 97.4% of all cells (558/573). Re-assessment of the appropriate amount of self-history using this model once again revealed that 16% of the gait cycle was the best fit for this data. The proposed parametric model allowed us to characterize the effects of Elastic Loading and Closed-Loop ambulation on background firing rate, preferred gait phase of firing, and load-dependent modulation. Lastly, once the proposed parametric model was applied to individual cells, we were able to explore the neural receptive fields associated with this ambulatory task.

Implications of Brain-Machine Interfaces

Traditional approaches used in Brain-Machine Interfaces (BMIs) for decoding neural information from populations of neurons use linear or non-linear regression models to characterize the relationship between variables of interest and the available neural activity. Unfortunately, in practice, these decoders need to be recalibrated with every session in order to maintain decoding accuracy(Carmena, 2012). Constant recalibration is a major issue that needs to be addressed before BMIs can become widely used by a range of individuals and patients.

Given our findings here such results are to be expected. We observed changes in the neural dynamics that occurred within the duration of single experimental conditions that approximately lasted for 90 seconds or several hundred steps. Our proposed parametric model allowed us to characterize the changes that occurred over three distinct experimental conditions with a single model structure. This result suggests that while there is significant plasticity within a population of neurons, the types of changes that will be observed are in fact constrained to a small set of degrees of freedom. Utilizing the proposed parametric model together with point process specific decoding algorithm such as the Point Process Adaptive Filter (Eden et al., 2004a) or the Hybrid Point Process Filter (Srinivasan et al., 2007) may allow for continuous decoding of gait phase and load forces even in the presence of ongoing adaptations.

Characterization of short and long term plasticity via receptive fields

The receptive fields of neurons are dynamic; that is their responses to relevant stimuli change with experience. Experience dependent-change or plasticity has been documented in a number of brain regions Donoghue (1995), Weinberger (1993), Jog et al. (1999), Pettet and Gilbert (1992), Mehta et al. (1997). We have shown

that our proposed point process model captures the receptive fields of individual cells during different conditions and over the course of days. Understanding how the receptive fields associated with locomotion change during training and with experience will be central to understanding the physiology of cortical locomotion control and the changes observed with pathology.

References

Akaike, H.. Information Theory And An Extension Of The Maximum Likelihood Principle. Second International Symposium on Information Theory 1973;1(1973):267–281.

Armstrong, D.M., Drew, T.. Locomotor-related neuronal discharges in cat motor cortex compared with peripheral receptive fields and evoked movements. The Journal of physiology 1984b;346:497–517.

Beloozerova, I.N., Sirota, M.G.. The role of the motor cortex in the control of accuracy of locomotor movements in the cat. The Journal of physiology 1993a;461:1–25.

Black, M., Bienenstock, E., Donoghue, J.P., Serruya, M., Wu, W., Gao, Y.. Connecting brains with machines: the neural control of 2D cursor movement. In: Neural Engineering, 2003. Conference Proceedings. First International IEEE EMBS Conference on. 2003. p. 580–583.

Brown, E.N., Barbieri, R., Ventura, V., Kass, R.E., Frank, L.M.. The time-rescaling theorem and its application to neural spike train data analysis. Neural Comput 2002;14(2):325–346.

Carmena, J.M.. Becoming Bionic. Spectrum, IEEE 2012;49(3):24–29.

Carmena, J.M., Lebedev, M.A., Crist, R.E., O'Doherty, J.E., Santucci, D.M., Dimitrov, D.F., Patil, P.G., Henriquez, C.S., Nicolelis, M.A.L.. Learning to control a brain-machine interface for reaching and grasping by primates. PLoS biology 2003;1(2):E42–E42.

Chapin, J.K., Moxon, K.A., Markowitz, R.S., Nicolelis, M.A.. Real-time control of a robot arm using simultaneously recorded neurons in the motor cortex. Nat Neurosci 1999;2(7):664–670.

Collin, C., Wade, D.T., Davies, S., Horne, V.. The Barthel ADL Index: A reliability study. Disability and Rehabilitation 1988;10(2):61–63.

Czanner, G., Eden, U.T., Wirth, S., Yanike, M., Suzuki, W., Brown, E.N.. Analysis of between-trial and within-trial neural spiking dynamics. J Neurophysiol 2008;99(5):2672–2693.

Daley, D.J., Vere-Jones, D.. An introduction to the theory of point processes. New York: Springer-Verlag, 1988.

Dempster, A.P., Laird, N.M., Rubin, D.B.. Maximum Likelihood from Incomplete Data via the EM Algorithm. Journal of the Royal Statistical Society Series B (Methodological) 1977;39(1):1–38.

Donoghue, J.P.. Plasticity of adult sensorimotor representations. Current opinion in neurobiology 1995;5(6):749–754.

Eden, U.T., Frank, L.M., Barbieri, R., Solo, V., Brown, E.N.. Dynamic analysis of neural encoding by point process adaptive filtering. Neural Comput 2004a;16(5):971–998.

Fitzsimmons, N.A., Lebedev, M.A., Peikon, I.D., Nicolelis, M.A.L.. Extracting kinematic parameters for monkey bipedal walking from cortical neuronal ensemble activity. Front Integr Neurosci 2009;3:3.

Georgopoulos, A.P., Schwartz, A.B., Kettner, R.E.. Neuronal population coding of movement direction. Science (New York, NY 1986;233(4771):1416–1419.

Gerstein, G.L., Kiang, N.S.. An approach to the quantitative analysis of electrophysiological data from single neurons. Biophys J 1960;1:15–28.

Giszter, S.F., Hart, C., Udoekwere, U., Markin, S., Barbe, C.. A Real-Time System for Small Animal Neurorobotics at Spinal or Cortical Levels. In: Neural Engineering, 2005. Conference Proceedings. 2nd International IEEE EMBS Conference on. 2005. p. 450–453.

Haslinger, R., Pipa, G., Brown, E.N.. Discrete time rescaling theorem: determining goodness of fit for discrete time statistical models of neural spiking. Neural Comput 2010;22(10):2477–2506.

Hille, B.. Ion channels of excitable membranes. Sunderland, Mass.: Sinauer, 2001.

Jog, M.S., Kubota, Y., Connolly, C.I., Hillegaart, V., Graybiel, A.M.. Building neural representations of habits. Science (New York, NY 1999;286(5445):1745–1749.

Johnson, A., Kotz, S.. Distributions in Statistics: Continuous Univariate Distributions. New York: Wiley, 1970.

Keat, J., Reinagel, P., Reid, R., Meister, M.. Predicting Every Spike: A Model for the Responses of Visual Neurons. Neuron 2001;30(3):803–817.

Lloyd-Jones, D., Adams, R., Carnethon, M., De Simone, G., Ferguson, T.B., Flegal, K., Ford, E., Furie, K., Go, A., Greenlund, K., Haase, N., Hailpern, S., Ho, M., Howard, V., Kissela, B., Kittner, S., Lackland, D., Lisabeth, L., Marelli, A., McDermott, M., Meigs, J., Mozaffarian, D., Nichol, G., O'Donnell, C., Roger, V., Rosamond, W., Sacco, R., Sorlie, P., Stafford, R., Steinberger, J., Thom, T., Wasserthiel-Smoller, S., Wong, N., Wylie-Rosett, J., Hong, Y., American Heart Association Statistics Committee and Stroke Statistics Subcommittee, . Heart disease and stroke statistics–2009 update: a report from the American Heart Association Statistics Committee and Stroke Statistics Subcommittee. Circulation 2009;119(3):480–486.

McCullagh, P., Nelder, J.A.. Generalized linear models. London; New York: Chapman and Hall, 1989.

Mehta, M.R., Barnes, C.A., McNaughton, B.L.. Experience-dependent, asymmetric expansion of hippocampal place fields. Proceedings of the National Academy of Sciences of the United States of America 1997;94(16):8918–8921.

Moran, D.W., Schwartz, A.B.. Motor cortical representation of speed and direction during reaching. J Neurophysiol 1999;82(5):2676–2692.

Orsborn, A., Dangi, S., Moorman, H., Carmena, J.. Closed-Loop Decoder Adaptation on Intermediate Time-Scales Facilitates Rapid BMI Performance Improvements Independent of Decoder Initialization Conditions. Neural Systems and Rehabilitation Engineering, IEEE Transactions on 2012;PP(99):1–1.

Palm, G., Aertsen, A.M.H.J., Gerstein, G.L.. On the significance of correlations among neuronal spike trains. Biological Cybernetics 1988;59(1):1–11.

Pettet, M.W., Gilbert, C.D.. Dynamic changes in receptive-field size in cat primary visual cortex. Proceedings of the National Academy of Sciences of the United States of America 1992;89(17):8366–8370.

Presacco, A., Goodman, R., Forrester, L., Contreras-Vidal, J.L.. Neural decoding of treadmill walking from noninvasive electroencephalographic signals. J Neurophysiol 2011;106(4):1875–1887.

Quinn, T.J., McArthur, K., Ellis, G., Stott, D.J.. Functional assessment in older people. BMJ 2011;343(aug22 1):d4681–d4681.

Schwarz, G.. Estimating the Dimension of a Model. Ann Statist 1978;6(2):461–464.

Shoham, S.S., Fellows, M.R.M., Normann, R.A.R.. Robust, automatic spike sorting using mixtures of multivariate t-distributions. J Neurosci Methods 2003;127(2):111–122.

Song, W., Giszter, S.F.. Adaptation to a cortex-controlled robot attached at the pelvis and engaged during locomotion in rats. J Neurosci 2011;31(8):3110–3128.

Srinivasan, L., Eden, U.T., Mitter, S.K., Brown, E.N.. General-purpose filter design for neural prosthetic devices. J Neurophysiol 2007;98(4):2456–2475.

Truccolo, W., Eden, U.T., Fellows, M.R., Donoghue, J.P., Brown, E.N.. A point process framework for relating neural spiking activity to spiking history, neural ensemble, and extrinsic covariate effects. J Neurophysiol 2005;93(2):1074–1089.

Velliste, M.M., Perel, S.S., Spalding, M.C.M., Whitford, A.S.A., Schwartz, A.B.A.. Cortical control of a prosthetic arm for self-feeding. CORD Conference Proceedings 2008;453(7198):1098–1101.

Weinberger, N.M.. Learning-induced changes of auditory receptive fields. Current opinion in neurobiology 1993;3(4):570–577.

Wilson, H.R.. Simplified Dynamics of Human and Mammalian Neocortical Neurons. J Theor Biol 1999;200(4):375–388.

Ziegler-Graham, K., MacKenzie, E.J., Ephraim, P.L., Travison, T.G., Brookmeyer, R.. Estimating the prevalence of limb loss in the United States: 2005 to 2050. Archives of physical medicine and rehabilitation 2008;89(3):422–429.

Assessment of Lower Extremity Motor Adaptation via an Extension of the Force Field Adaptation Paradigm

Abstract

Lower extremity rehabilitation has seen recent increased interest. New tools are available to improve gait retraining in both adults and children. However, it remains difficult to determine optimal ways to plan interventions due to difficulties in continuously monitoring outcomes in patients undergoing rehabilitation. In this paper, we introduce an extension of the Force Field Adaptation Paradigm, used to quantitatively assess upper extremity motor adaptation, to the lower extremity. The algorithm is implemented on the Lokomat lower extremity gait orthosis and is currently being utilized to assess short-term motor adaptation in a group of 40 healthy adult subjects (ClinicalTrials.gov NCT01361867). We described some of our initial findings from this clinical trial. Establishing an understanding of how healthy adults' motor systems adapt to external perturbations will be important to understanding how the adaptive mechanisms involved in gait integrate information and how this process is altered by disease.

Introduction

The field of lower extremity rehabilitation has recently witnessed a surge in interest. Devices such as the PAM/POGO (Reinkensmeyer et al., 2006), the LOPES (Veneman et al., 2007) and the LOKOMAT (Colombo et al., 2000) have played a key role in this trend. Robots allow highly repeatable interventions and serve as instruments to quantify the rehabilitation progress. Despite the current high cost of many of these devices, the introduction of FDA-registered robotic gait retraining devices in the clinic is an important step toward assessing the efficacy of these tools

via randomized multi-centered clinical trials.

Initial studies of robotic technologies for lower extremity rehabilitation interventions show high variability in individual responses (Hidler et al., 2009, Hornby et al., 2008, Husemann et al., 2007, Mayr et al., 2007). Many aspects of robot-assisted gait training could contribute to the differences seen in motor gains across subjects. The level of patient engagement during the rehabilitation session is a factor associated with the magnitude of the observed motor gains following rehabilitation (Koenig et al., 2011). Several researchers have hypothesized that the patient's baseline condition (i.e. pre-rehabilitation functional state and impairment level) correlates with the magnitude of observed motor gains. Additionally, mechanical constraints imposed by the robotic system itself (e.g. limitations in the degrees-of-freedom imposed at the pelvis) during functional rehabilitative tasks may play an important a role in the observed variability in rehabilitation outcomes across patients. Since motor adaptation refers to learning through the alteration of motor commands in response to changes in the environment, by quantifying the adaptive process during rehabilitation one can gain insight into the factors that govern this variability. One would anticipate that adaptations observed during performance of the training session in response to forces generated by the robotic system would be predictive of rehabilitation outcomes.

The goal of the work herein presented is to develop a platform to quantify the motor adaptations that occur during gait retraining. Specifically, we developed a methodology to characterize the rates of lower extremity motor adaptation in a group of healthy adults. The proposed methodology is an extension of a paradigm originally used to test motor adaptation in the upper extremities by Shadmehr and Mussa-Ivaldi (1994). The basis for this paradigm is the introduction of velocity-dependent force perturbations perpendicular to the direction of movement that induce trajectory errors to which the subjects must then adapt. Measurement of a subject's adaptive compensatory forces and restoration of movement kinematics during and after the removal of these perturbations can be used to determine the rates of motor adaptation. The results presented here are preliminary results of an ongoing clinical trial (ClinicalTrials.gov NCT01361867) to assess the rates of motor adaptation in healthy adults. In future studies, we plan to establish a methodology for comparing motor adaptations between healthy individuals and patients based on the work herein presented. The methodology will also provide a potential tool for assessing the efficacy of different rehabilitation methodologies, in terms of the rates of adaption and the retention of motor skills. An abbreviated version of this chapter has been previously published (Cajigas González et al., 2010b).

Methods

The Force Field Adaptation Paradigm

Shadmehr and Mussa-Ivaldi (1994) studied how the central nervous system adapts to changing environment dynamics as the hand interacts with a novel mechanical environment, i.e. an applied force field, using the force field adaptation paradigm (FFAP). In their experimental methodology, a practice period allowed subjects to practice reaching to a target while holding the end-effector of a robotic arm in a force free condition (termed Baseline/Null-Field Movement). After this practice period, a perturbing velocity-dependent force was applied perpendicular to the direction of motion. That is,

$$F(t) = \begin{bmatrix} F_x(t) \\ F_y(t) \end{bmatrix} = \begin{bmatrix} 0 & -B \\ 0 & 0 \end{bmatrix} \begin{bmatrix} v_x(t) \\ v_y(t) \end{bmatrix} \tag{4.2}$$

where $F(t)$ is the vector of end-effector forces, F_x and F_y are the x and y components of the force, B is the viscous damping coefficient, and v_x and v_y are the x and y components of the end-effector velocity. During straight line movements, $v_x = 0$ and v_y is approximately bell-shaped. Thus, according to Equation 4.2, bell-shaped force proportional to v_y is applied in the negative x-direction. During force field movements, subjects were are instructed to continue performing straight line movements at their original movement velocity. Over time, subjects adapted to the force field and re-achieved the baseline trajectory by generating compensatory forces. Upon removal of the force field and return to the baseline condition, the compensatory forces that subjects had learned to apply drove their arms along trajectories that mirrored the path their limbs would have followed had they not compensated for the applied force field. This mirroring, or after-effect, suggests the development of an internal model during the process of adaptation. The time course of the after-effect can be quantified by the perpendicular displacement from the baseline path at the point of maximum velocity/force. Let $\hat{i}$ and $\hat{j}$ be unit vectors in the x and y directions respectively, then the maximum perpendicular deviation from the baseline path is

$$d_{\perp}(t) = \langle \hat{i}\,, p_n(t) - p_0(t) \rangle = x(t) - x_0 \tag{4.3}$$

where $\langle x_1\,, x_2 \rangle = x_1^T x_2$ is the standard Cartesian inner product, x_i^T denotes the transpose of the vector x_i, $p_n(t)$ is the position vector of the end-effector at time t during the n^{th} trial, and p_0 is the position vector at time t during the mean of the baseline trials. Later experiments by Scheidt et al. (2000b) introduced error-clamp (EC) movements (termed there as force-channel movements) during which the subject's arm is limited to move along the original straight line trajectory. The result of error-clamp trials is a minimization of the trajectory error between the original and

current movement paths. Error-clamp movements, interspersed during the force field condition, offer a window into the time course of the adaptive process by measuring the subject's lateral compensatory forces during imposed straight reaching movements. These measured forces can be compared against the applied force field, to determine how well the subject has adapted to the applied force field during the learning block condition. The coefficient of adaptation, a measure of the subject's current level of adaptation, is defined as

$$F_x^n(t) = c_{adapt} F_x^{ideal}(t) \tag{4.4}$$

where $F_x^n(t)$ is the force measured during the n^{th} error clamp trial, $F_x^{ideal}(t)$ is the ideal compensatory lateral force computed from Equation 4.2 using the average velocity in the y-direction during baseline trials, and c_{adapt}, is the coefficient of adaptation. Figure 4.2 (top) summarizes the four conditions for the upper extremity FFAP.

Lower Extremity Force Field Adaptation Paradigm

Extension of the FFAP is a natural approach for testing motor adaptation in the lower limb. Yet the implementation of this paradigm carries a number of intrinsic difficulties for a lower limb system. For example, how does the cyclical nature of the gait cycle correspond to a point-to-point reaching movement or what constitutes a perpendicular perturbation? Our extension of the FFAP to the lower extremity (LE-FFAP) relies on the following observations:

1. The cyclical gait pattern can be considered a point-to-point movement where the start and end points coincide. With this observation, in any coordinate system (joint, end-effector/ankle, Cartesian coordinates, etc.), the standard gait pattern is the curvilinear equivalent to the upper extremity straight line movements.

2. In the lower extremity, the subject's baseline gait pattern defines which movements are parallel to the baseline path. At each point along the gait pattern, a perpendicular direction to the path can be determined and perturbations can be applied in this direction. We define

$$u_{||}(k) = \left[\ u_{||\theta_h}(k),\ \ u_{||\theta_k}(k)\ \right]^T \tag{4.5}$$

and

$$u_{\perp}(k) = \left[\ u_{\perp\theta_h}(k),\ \ u_{\perp\theta_k}(k)\ \right]^T \tag{4.6}$$

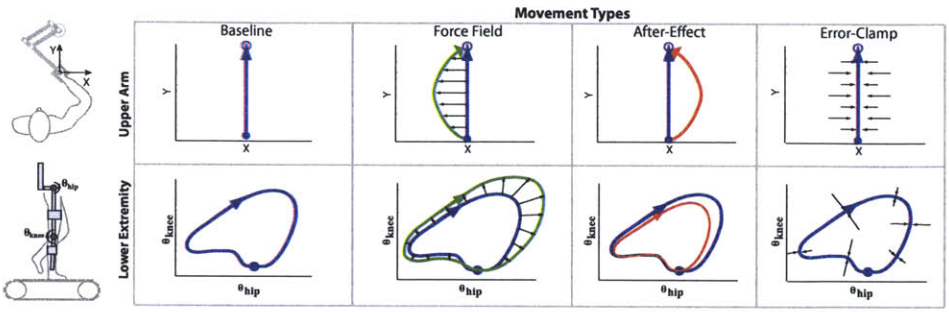

Figure 4.2: **Comparison between the lower and upper extremity FFAP**. *(left-most)* **Baseline Movements**: In the upper extremity FFAP, subjects are asked to make rapid point-to-point movements to a target. In the lower extremity, subjects are asked to walk normally at a specified treadmill speed. The gait cycle can be considered a point-to-point movement where the beginning and end points coincide. *(left of center)* **Force Field:** In the upper extremity FFAP, a velocity dependent force field is applied perpendicular to the direction of movement. In the lower extremity FFAP, unit vectors along the baseline path can be used to define instantaneous coordinate systems oriented parallel and perpendicular to the path. Velocity-dependent force/torque perturbations are then applied along the instantaneous perpendicular direction. *(right of center)* **After-Effect**: In the upper and lower extremity FFAP removal of the force field results in a movement that is the mirror image of the path their limbs would have followed had they not compensated for the applied force field. *(right)* **Error Clamp Movements**: Upper Extremity FFAP/Lower Extremity FFAP - measurement of the interaction forces while the subject is forced to move along their original baseline path allows the adaptive forces to be assessed over time. These compensatory forces/torques can be compared to the ideal compensatory force (defined by the baseline velocity of the subject during baseline movements). Error clamps can be randomly interspersed within the baseline, force field, and unlearning phases at an occurrence of 20% in order to measure forces prior, during, and after adaptation.

as the parallel and perpendicular unit vectors, respectively, at the k^{th} point along the gait cycle. Then

$$T_k = \begin{bmatrix} u_{||\theta_h}(k) & u_{||\theta_k}(k) \\ u_{\perp\theta_h}(k) & u_{\perp\theta_k}(k) \end{bmatrix} \tag{4.7}$$

is the transformation matrix from hip and knee coordinates to path coordinates at the k^{th}point along the gait cycle. For example, T_k can be used to project the instantaneous velocity vector in joint coordinates at k^{th}point of the current gait cycle into the corresponding parallel and perpendicular components with respect to the baseline path. A velocity dependent perturbation torque can then be generated as,

$$\tau(k) = \begin{bmatrix} \tau_{hip}(k) \\ \tau_{knee}(k) \end{bmatrix} = T_k{}^T \begin{bmatrix} 0 & 0 \\ B & 0 \end{bmatrix} T_k \begin{bmatrix} \dot{q}_h(k) \\ \dot{q}_k(k) \end{bmatrix} \tag{4.8}$$

$$\tau(k) = T_k{}^T B T_k \dot{q}(k) \tag{4.9}$$

where τ_{hip} and τ_{knee} are the hip and knee components of the joint torque vector $\tau(k)$, B is the viscous damping coefficient, and $\dot{q}_h$ and $\dot{q}_k$ are the hip and knee components of the joint velocity vector, $\dot{q}(k)$.

3. Compensation to the applied perturbations can be assessed by forcing the subject to walk along their baseline gait trajectory and measuring the generalized interaction forces perpendicular to the baseline path. This is accomplished through implementation of error-clamp trials. During error-clamp trials, the joint torques $\tau(k)$ required to maintain the subject moving along their baseline path is equal and opposite to the torques applied by the subject. Because the perturbing force field is oriented perpendicular to the baseline path, the perpendicular component of the interaction torque during the n^{th} trial, $\tau_\perp^n$, represents the current adaptive compensatory force. This component,$\tau_\perp^n$, is obtained by projecting the joint torques onto the instantaneous perpendicular direction along the baseline path, i.e.

$$\tau_\perp^n(k) = \langle u_\perp , \tau(k) \rangle \tag{4.10}$$

The adaptation coefficient is defined analogously to Equation 4.4, e.g.

$$\tau_\perp^n(k) = c_{adapt}\, \tau_\perp^{ideal}(k) \tag{4.11}$$

where $\tau_\perp^{ideal}(k) = B \cdot v_{||}^{BL}(k)$ is determined from the viscous coefficient B and the parallel velocity component during mean baseline locomotion. The time course of the after-effect can be quantified by the perpendicular displacement

from the baseline path at the point of maximum velocity. We define the perpendicular deviations from the baseline path as

$$d_{\perp}^{n}(k) = \langle u_{\perp}(k), q_n(k) - q_0(k) \rangle \tag{4.12}$$

where $q_n(k) = \begin{bmatrix} \theta_{hip}(k) & \theta_{knee}(k) \end{bmatrix}^T$ is the joint position vector at the k^{th} gait cycle point during the n^{th} trial, and $q_0(k)$ is the position vector at the k^{th} during the mean baseline trials. Figure 4.2 shows a comparison between lower and upper extremity FFAP. We derive two summary measures from Equation 4.12. First we define the point within the gait cycle with the maximal deviation across trials as

$$k_{max} = \arg\max_{n,k} |d_{\perp}^{n}(k)| \tag{4.13}$$

and define the perpendicular error at the point of maximal deviation as

$$d_{\perp}^{max}(n) = d_{\perp}^{n}(k_{max}) \tag{4.14}$$

Equation 4.14 turns out to be informative for looking at individual subject responses. However, k_{max} tends to change across subjects. Thus when comparing across subjects we sum $d_{\perp}^{n}(k)$ between 40% and 65% of the gait cycle (0% corresponds to mid-stance on the perturbed leg), which roughly corresponds to swing phase on the perturbed leg, e.g.

$$d_{\perp}^{sum}(n) = \sum_{k=K_{p_1\%}}^{K_{p_2\%}} d_{\perp}^{n}(k) \tag{4.15}$$

where $K_{p_i\%}$ in the sample within a step corresponding to p_i^{th} percentile of the gait cycle. If the gait cycle is normalized to 500 points, as in our current implementation, $K_{40\%} = 200$ and $K_{65\%} = 325$. $d_{\perp}^{sum}(n)$ is a more robust measure to use when comparing effects across subjects.

Assistance along the movement path

In the long term, we hope to use the LE-FFAP to test motor adaptation in patients with a range of locomotor deficits such as stroke, spinal cord injury, and cerebral palsy. In this case, it is possible that subjects may require assistance along the direction of movement in order to complete a baseline gait cycle. Given a desired torque along the movement direction, $\tau_{||}(k)$, the path-assistive hip and knee torques, $\tau_{hip}(k)$ and $\tau_{knee}(k)$ respectively can be computed using as

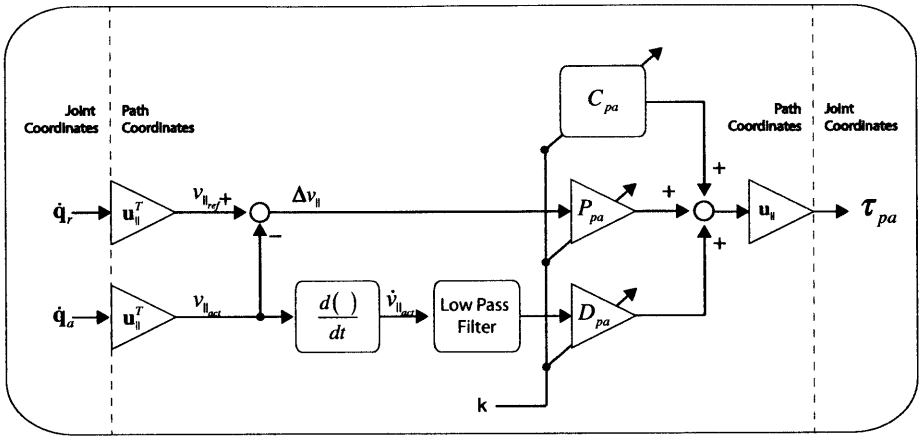

Figure 4.3: **Path Assistance Block Diagram.** Assistance along the movement path is accomplished via the use of a proportional-derivative-constant architecture. $\dot{q}_r = v_r$ is the reference or desired joint velocity vector and $\dot{q}_a = v_a$ the current instantaneous joint velocity vector.

$$\tau_{pa}(k) = \begin{bmatrix} \tau_{hip}(k) \\ \tau_{knee}(k) \end{bmatrix} = T_k^T \begin{bmatrix} \tau_{||}(k) \\ 0 \end{bmatrix} \tag{4.16}$$

$$= u_{||}(k)\,\tau_{||}(k) \tag{4.17}$$

where $\tau_{pa}(k)$ is the vector of path-assistive torques in joint coordinates at the k^{th}point along the gait cycle and T_k is as defined in Equation 4.7. Note that because T_k is orthonormal, then the transformation matrix from path to joint coordinates, T_k^{-1} , equals the transpose of T_k. We allow for a broad range of path assistive torques using a proportion-derivative-constant architecture, e.g.

$$\tau_{||}(k) = C_{pa}(k) + P_{pa}(k)\left(v_{||_{act}}(k) - v_{||_{ref}}(k)\right) + D_{pa}(k)\left(\dot{v}_{||_{act}}(k) - \dot{v}_{||_{ref}}(k)\right) \tag{4.18}$$

where $C_{pa}(k)$, $P_{pa}(k)$, and $D_{pa}(k)$ are the constant, proportional, and derivative gains at the k^{th} point along the gait cycle; $v_{||_{act}}$ and $v_{||_{ref}}$ are the current and reference movement velocities along the path respectively and are obtained via projection of the current and reference joint velocities, $\dot{q}_a$ and $\dot{q}_r$ respectively, onto the current parallel unit vector. Figure 4.3 graphically summarizes Equations 4.17 and 4.18.

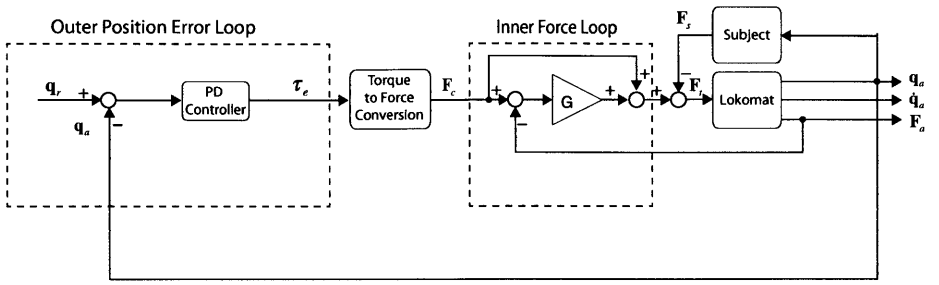

Figure 4.4: **Standard Lokomat Impedance Control System.** The clinical version of the Lokomat uses an impedance control architecture. A PD controller generates corrective torques that aim to minimize the error between the desired joint position, q_r, and the current joint position, q_a. An inner force loop is used to minimized the apparent device inertia - thereby improvement the systems back-drivability. Adapted from**Riener et al. (2005).**

Implementation

The FFAP of Shadmehr and Mussa-Ivaldi (1994) was extended to the lower extremity and implemented on the Lokomat lower extremity gait orthosis (Hocoma AG, Switzerland) (Colombo et al., 2000, 2001, Riener et al., 2005). The standard Lokomat impedance control system is shown in Figure 4.4. For clinical applications, a reference joint trajectory, $q_r(t)$, is pre-specified and compared to the actual joint trajectory, $q_a(t)$, obtained from the exoskeleton potentiometers to generate a joint position error signal. This joint position error is processed by a proportional-derivative (PD) controller to generate a corrective torque, τ_e, that aims to reduce the joint position error. An inner force loop is used to reduce the apparent inertia of the robotic exoskeleton and improve the back-drivability of the system. This impedance control architecture is due to Hogan (1985).

The LE-FFAP begins with the collection of pre-baseline data with the Lokomat in a highly back-drivable state, which allows the subject to move freely within the Lokomat. Implementation of a new Lokomat mode of operation, termed Path Control (Duschau-Wicke et al., 2010), allows subjects to naturally control the timing of their gait. The path control algorithm relies on the synchronization of the current gait cycle with a normalized reference gait cycle. This synchronization is accomplished via the algorithm of (Aoyagi et al., 2007) (See Figure 4.5 top right). The baseline condition of the LE-FFAP requires subjects to walk as freely as possible while attached to the Lokomat. Device loading of the subject was minimized via the generalized elasticity method of Vallery et al. (2009b). This procedure utilizes

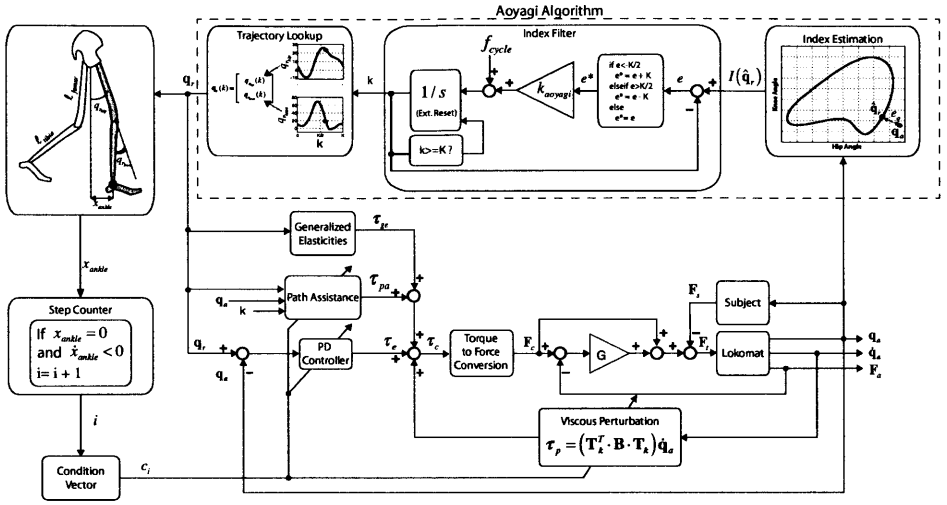

Figure 4.5: **Lower Extremity Force Field Adaptation Paradigm (LE-FFAP) Control System Diagram.** As the subject walks freely in the Lokomat, a step counter is used to determine the current experimental condition. Left and right legs are controlled independently and the desired leg to be perturbed needs to be specified at the beginning of the experiment. There are five possible modes of operation: Baseline (1), Baseline Error Clamp (2), Force Field (3), Force Field Error Clamp (4), and Error Clamp (5). Table 4.3 summarizes which blocks are enabled during which experimental condition. See text for a description of each of the main modules.

the subject's own pre-baseline gait cycle and a model of the Lokomat dynamics to generate an conservative (stable) force field that minimizes subject effort required to move the orthosis along the gait trajectory while maintaining passivity of the control system. Lastly, assistive torques along the movement path (as described in Section) might need to be provided to individuals needing assistance while walking within the Lokomat or to help minimize the effects of the increased subject/device inertia during error clamps in health subjects. Figure 4.5 summarizes all of the major components of Lokomat control system used to implement the Lower Extremity Force Field Adaptation Paradigm (LE-FFAP). (Goldsmith, 2010) provides an in depth description of the first implementation of the LE-FFAP. Notably, assistance along the movement path (Path Assistance) and subject-specific generalized elasticities were absent from our prior implementation.

There are five possible modes of operation required for the implementation of the LE-FFAP - Baseline (1), Baseline Error Clamp (2), Force Field (3), Force Field

Condition	Condition Number	PD Controller	Viscous Perturbation	Path Assistance
Pre-Baseline	0	-	-	-
Baseline	1	-	-	-
Baseline Error Clamp	2	+	-	+
Force Field	3	-	+	-
Force Field Error Clamp	4	+	-	+
Error Clamp	5	+	-	+

Table 4.3: **LE-FFAP Control Modules Active within each Experimental Condition.** Note that path assistance is only present during error clamp trials for our current work with healthy subjects. We envision that this technique can be used in all trial conditions when used with impaired subjects.

Error Clamp (4), and Error Clamp (5). Table 4.3 summarizes which blocks are enabled during which experimental condition.

Subject Recruitment

This clinical trial (ClinicalTrials.gov NCT01361867) is currently being conducted by the Motion Analysis Laboratory at Spaulding Rehabilitation Hospital, Boston, MA. IRB approval has been obtained to recruit 40 healthy adult volunteers (males and females, age 18-55 years, with normal gait). Relevant exclusion criteria include:

1. Lower extremity fractures
2. Current or previous history of orthopedic injury that would prevent safe use of the Lokomat gait orthosis
3. Body/femoral length size beyond the limits of Lokomat robotic legs (femur length between 350-470mm)
4. Body weight > 135kg (~298 lb.) maximum limit of the body weight support system
5. Skin lesions on the lower extremities
6. Cardiovascular or pulmonary contraindications

7. Motor system or proprioceptive impairments
8. Severe cognitive impairments that would prevent the use of the Lokomat gait orthosis

Experimental Procedures

We distinguish between two types of experiments that allow us to study distinct features of the adaptation process of subjects and one type that allows for customization of the robotic exoskeleton to the particularities of each individual's gait pattern. In all experiments a metronome with a period of .7 sec per beat is used to pace the subjects. The treadmill is set to a speed of 3.0 km per hour. The viscous damping coefficient, B, was set to 3.5 Newton-sec/rad.

Pre-Baseline Experiments

During the pre-baseline experiments, a generic gait pattern is used as the template within the lookup tables of the Aoyagi synchronization algorithm. The Generalized Elasticities block is also optimized to the same generic gait pattern. Subject are allowed to walk freely within the device with no applied perturbation forces and joint kinematics are recorded via potentiometers on the Lokomat. From this pre-baseline data, an average trajectory in joint space is obtained for the current subject. This information is used to generate a new template (baseline path) for the Aoyagi synchronization algorithm and the Generalized Elasticities block is optimized to this new gait pattern. Lastly, unit vectors parallel, $u_{||}$, and perpendicular, $u_{\perp}$, to the path are computed and used to determine the perturbation torques to be applied according to Equation 4.9.

After-Effect Experiments

After-Effects experiments allow for the assessment of motor adaptation via the observation of the changes in kinematic error during exposure to the force-field and after removal of the force-field. Theses experiments consist of three blocks:

- **Baseline:** For 100 steps subjects are allowed to walk freely in a force-free condition.
- **Force Field:** For 100 steps subjects are able to walk freely but with the addition of a velocity-dependent force field that is applied perpendicular to the path of motion.

- **After-Effect:** For 100 steps subjects are allowed to walk in force-free condition.

Figure4.6 A shows the condition vector specifying the mode of operation of the Lokomat during each portion of an After-Effects experiment. Maximal perpendicular deviation from the baseline path ($d_{\perp}^{max}(n)$ or $d_{\perp}^{sum}(n)$) as described in Section is used to assess the adaptive changes observed during these experiments.

Error Clamp Experiments

Error-Clamp experiments allow for the assessment of motor adaptation via the observation of the changes in force generation during exposure to the force-field and the decay observed once the force field is removed and motor error is maintained at zero. These experiments consist of three blocks:

- **Baseline:** For 100 steps subjects are allowed to walk freely in a force-free condition. Error-clamp trials are interspersed at random with frequency of 20% (e.g. 1 out of 5 steps is an error clamp).
- **Force Field:** For 100 steps subjects are able to walk freely but with the addition of a velocity-dependent force field that is applied perpendicular to the path of motion. Error-clamp trials are interspersed at a frequency of 20% (e.g. 1 out of 5 steps is an error clamp).
- **Error-Clamp:** For 100 steps subjects are forced to walk along their baseline path.

Figure4.6 B shows the condition vector specifying the mode of operation of the Lokomat during each portion of an Error-Clamp experiment. The adaptation coefficient, c_{adapt}, from Equation 4.11 is used to assess the adaptive changes in force generation observed during these experiments.

Results

After-Effects Experiment

Figure 4.7 shows the results for a single subject during an After-Effect Experiment. Figure 4.7 A shows the joint trajectories during Baseline, Force Field, After-Effect portions of the experiment. There were 100 steps in each phase. Figure 4.7 B shows the mean baseline curve from A, the mean of the first 10 steps in Force Field, and the mean of the first 10 steps in the After-Effects portion of the experiment. Figure 4.7 C shows the maximal perpendicular deviation from the mean baseline

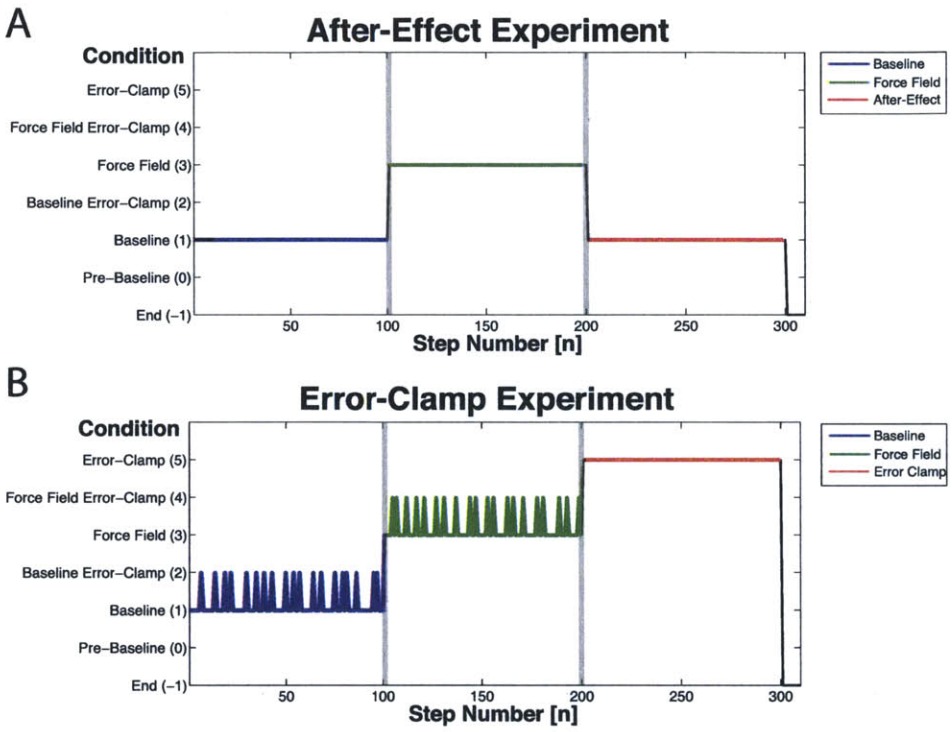

Figure 4.6: **Condition Vectors for After-Effect and Error-Clamp Experiments. A) After-Effect Experiment Condition Vector.** Subjects are allowed to walk in the Baseline condition for 100 steps, followed by exposure to a velocity-dependent force field for 100 steps. After exposure to the force-field, the force field is turn off. Adaptive changes during these experiments are observed via the changes in kinematic error within the Force Field and After-Effects portion of the experiment using a measure of the perpendicular deviation from the baseline path ($d_{\perp}^{max}(n)$ or $d_{\perp}^{sum}(n)$). **B) Error-Clamp Experiment Condition Vector.** Subjects are allowed to walk in the Baseline Condition for 100 steps, followed by exposure to a velocity-dependent force field for another 100 steps. Error-clamp trials are interspersed at random with frequency of 20% within both the Baseline and Force Field conditions. After the end of the Force Field condition, the subject forced to walk along their original baseline path using error-clamp trials for a total of 100 steps. The adaptation coefficient, c_{adapt}, from Equation 4.11 is used to assess the adaptive changes in force generation observed during these experiments.

path, $d_{\perp}^{max}(n)$. The dark curves represent an exponential decay model applied to the data to illustrate the trends and identify relevant time constants. The estimated exponential model was

$$d_{\perp}^{max}(n) = \begin{cases} 0 & 1 < \text{n} < 100 \\ 2.6 \times 10^{-2} \cdot e^{\frac{-t}{84}} & 101 < \text{n} < 200 \\ 3.0 \times 10^{-2} \cdot e^{\frac{-t}{111}} & 201 < \text{n} < 300 \end{cases}$$

where n is the step number. This piecewise regression on $d_{\perp}^{max}(n)$ yields an $R^2$of 77%. While the time constants associated with the Force Field and After-Effects portions of the experiment phases are suggestive that the after-effect process decays at a slightly slower rate than the adaptation process in this subject, the confidence intervals for these coefficients are extremely large (±60 steps). Therefore, the apparent difference between the decay rates observed in this subject is not statistically significant.

Error-Clamp Experiment

Figure 4.8 shows the results of a single subject during an Error-Clamp experiment. Use of a metronome during all experiments helped make the movement velocity along the baseline path consistent across steps and across different portions of the experiment as seen in Figure **4.8** A. The exponential model fit to the adaptation coefficient data yielded an R^2 of 88.9% and time constants for the rise and fall of 11 and 23 steps respectively.

Figure 4.9 shows preliminary aggregate data for both the After-Effect (Panel A) and Error-Clamp (Panel B) experiments.

Discussion

The work herein presented demonstrates how the LE-FFAP can be used to assess lower extremity motor adaptation. The theoretical extension of the FFAP to the lower extremity consisted of viewing the closed loop gait cycle in joint coordinates (equivalently end-effector coordinates) as a point-to-point movement where the beginning and end points coincide. With this analogy made, all portions from the standard FFAP experiments had natural analogues in the lower extremity case. Implementation of the LE-FFAP within the Lokomat lower extremity gait orthosis required the use of various recently published control models for the Lokomat, namely the Path Control algorithm (Duschau-Wicke et al., 2010) and the Generalized Elasticities method of Vallery et al. (2009b). In practice, a robotic exoskeleton

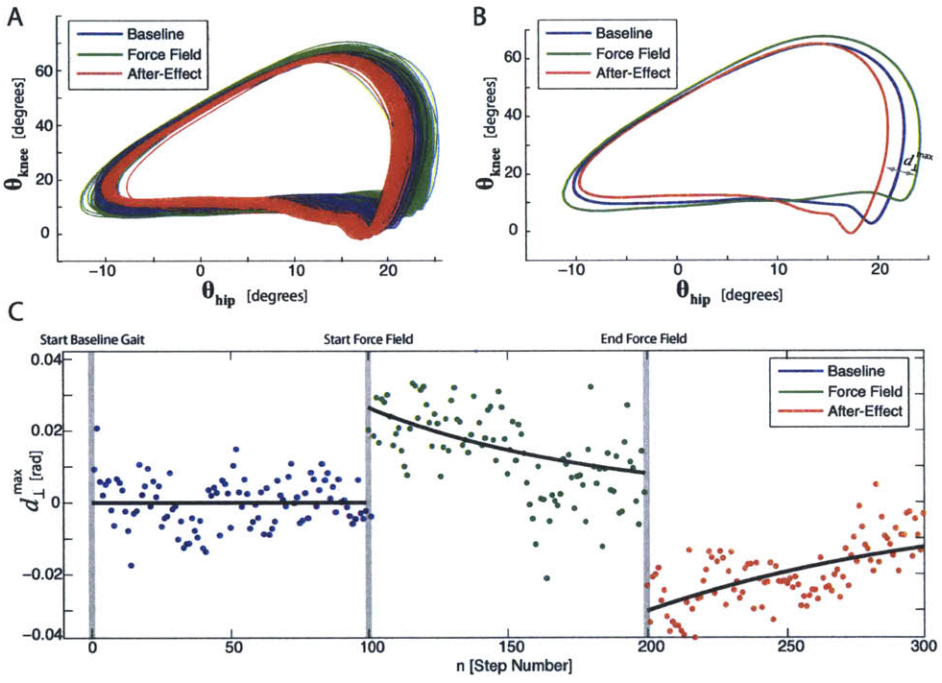

Figure 4.7: **Single Subject After-Effect Experiment Results.** A) Joint trajectories during Baseline, Force Field, and After-Effect phases of experiment. B) Mean trajectories during baseline, force field, and after-effects trajectories. C) Perpendicular deviation from the baseline path at the point of maximum deviation, $d_{\perp}^{max}(n)$ (point indicated in B).

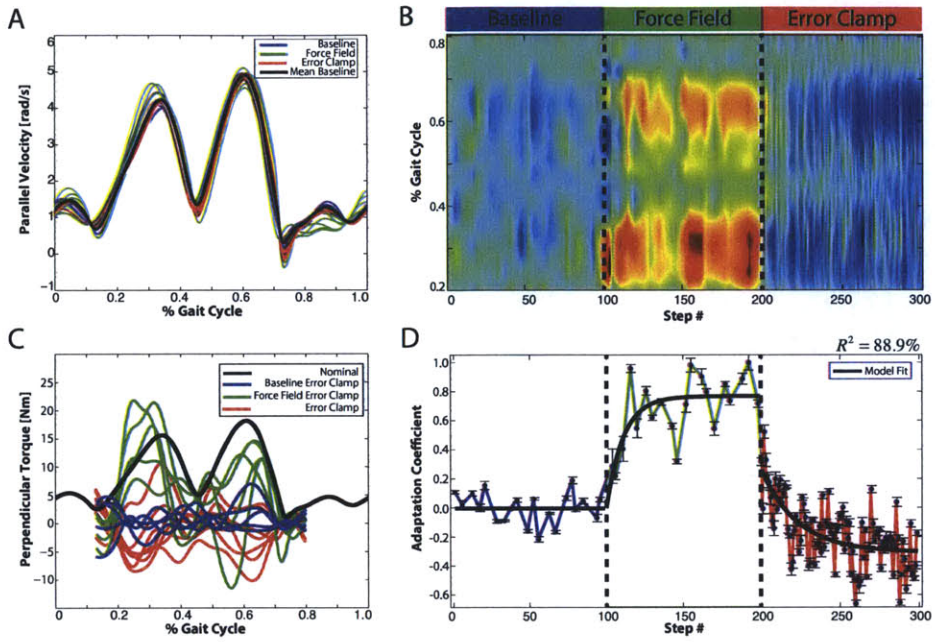

Figure 4.8: **Single Subject Assessment of Motor Adaptation. A) Nominal viscous disturbance.** The nominal perpendicular disturbance that is applied during the Force Field block is proportional to the movement velocity parallel to the baseline movement path, $v_{||_{act}}$. **B) Subject response within and across steps.** Forces during non error-clamp steps were estimated by interpolation for ease of visualization only and are not used in computation of the adaptation coefficient. **C) Subject response within each experimental segment vs. nominal response.** During the Baseline condition, the subject-applied torque perpendicular to the movement path (in blue) is approximately zero since the subject is moving along their baseline path. During the Force Field condition the subject-applied torque (in green) becomes closer to the disturbance being applied, indicating that the subject is adapting to the expected perturbation. During the last experimental block consisting of all error-clamp trials, the subject-applied torque (in red) slowly returns to towards zero. **D) Adaptation Coefficient.** The adaptation coefficient was computed according to Equation 4.11 by using the perpendicular torque during swing phase (within 20%-80% of the gait cycle as measured in the device; mid-stance is defined as 0%). The exponential model fit to the adaptation coefficient data yielded an R^2 of 88.9% and time constants for the rise and fall of 11 and 23 steps respectively.

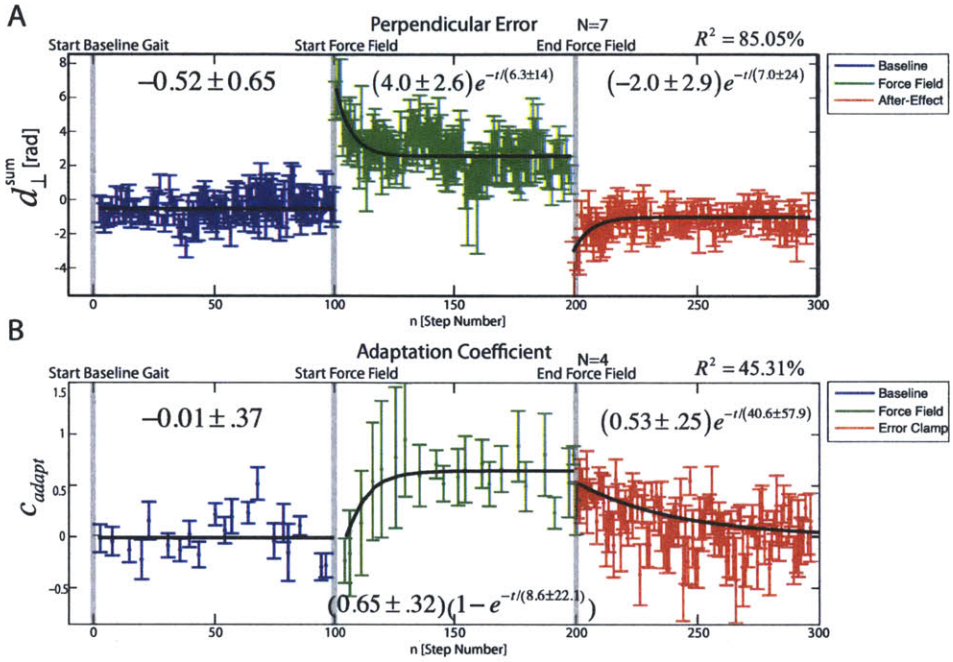

Figure 4.9: **Aggregate After-Effect and Error Clamp experiment responses. A) Maximal perpendicular deviation, $d_{\perp}^{sum}(n)$, during an After-Effect experiment (N=7).** Dark line indicates the mean±SEM across subjects. Note that initial exposure to the force fields leads to a large deviation from the baseline path and that subjects quickly correct for the perturbation (time constant ~6 step). Removal of the force field results in an after-effect. Note that the time constant associated with the after-effects is quite similar to the time constant of adaptation during force field. **B) Adaptation coefficient, $c_{adapt}(n)$ (mean±SEM), obtained from Error-Clamp experiment (N=4).** Note that the adaptation coefficient observed during the last portion of Error-Clamp experiment shows a decay time constant of approximately 5 times the time constant seen during exposure to the force field. Due to the large standard errors on these estimates, this result is only suggestive - a larger number of subjects will needed to make a conclusive statement on the adaptation dynamics during these two segments.

with lower inertia would be ideal for these types of experiments. However, we selected the Lokomat since there are currently more than 300 devices being used around the world. Implementation of the LE-FFAP on this platform thus opens the possibility for developing large scale clinical trials to understand the adaptive processes involved in healthy locomotion and how these processes are affected by diseases like stroke, traumatic brain injury, and spinal cord injury.

A uniform framework for studying upper and lower extremity motor adaptation

Numerous investigators have aim to study motor adaptation in the lower extremity(Emken and Reinkensmeyer, 2005, Reisman et al., 2007, Banala et al., 2009, Lam et al., 2006, Reisman et al., 2005). Unfortunately, the wide range of distinct devices used to conduct these studies make experiments difficult to validate. Moreover, the measures of adaptation reported change across studies. Taken together, these current limitations make it difficult if ot to easily compare results across experiments or to perform meta-analysis of the data available from various studies. We hope that by developing the LE-FFAP for a platform that is standardized and becoming widely available will help to produce study outcome measure that are more easily compared. Additionally, we hope that study protocols can become easily transferrable across institutions so that large scale trials can be undertaken.

Potential uses

Incorporating the LE-FFAP into clinical systems available around the world would open up a number of interesting possibilities. First, the LE-FFAP could be used as an assessment tool within current gait retraining strategies. Being able to understand the effects of distinct rehabilitation strategies on adaptation rates may allow for the identification of strategies that are more effective (e.g. yield larger adaptation rates or longer retention rates). In the long term, such assessment tools might allow clinicians to monitor the adaptation rates of individual patients and design interventions to maximize individual outcomes. Slightly less ambitious, but still insightful, would be the ability to track an individuals' adaptation rate over time. Much like hemoglobin A1C is a useful marker of blood sugar control in a diabetic patient, rates of adaptation may be indicative of the ability of the nervous system acquire new motor behaviors via rehabilitation. Lastly, because the LE-FFAP is analogous to its upper extremity counterpart, an extremely rich set of experimental protocols developed over the last 20 years can be directly applied to lower extremity research. Conversely, the LE-FFAP algorithm, suggests a natural approach for studying cyclical tasks (such as target tracking) in the upper extremity.

Future Work

Future work will include the analysis of aggregate After-Effect and Error-Clamp experiments from 40 healthy adult subject at the conclusion of the ongoing clinical trial. Establishing an understanding of how healthy adults' motor systems adapt to external perturbations will be an important step towards understanding how the adaptive mechanisms involved in gait are altered by disease.

References

Aoyagi, D., Ichinose, W., Harkema, S.J., Reinkensmeyer, D.J., Bobrow, J.E.. A robot and control algorithm that can synchronously assist in naturalistic motion during body-weight-supported gait training following neurologic injury. IEEE Trans Neural Syst Rehabil Eng 2007;15(3):387–400.

Banala, S., Kim, S.H., Agrawal, S., Scholz, J.. Robot Assisted Gait Training With Active Leg Exoskeleton (ALEX). Neural Systems and Rehabilitation Engineering, IEEE Transactions on 2009;17(1):2–8.

Cajigas González, I., Goldsmith, M., Duschau-Wicke, A., Riener, R., Smith, M., Brown, E.N., Bonato, P.. Assessment of lower extremity motor adaptation via an extension of the Force Field Adaptation Paradigm. In: Engineering in Medicine and Biology Society (EMBC), 2010 Annual International Conference of the IEEE. 2010b. p. 4522–4525.

Colombo, G., Joerg, M., Schreier, R., Dietz, V.. Treadmill training of paraplegic patients using a robotic orthosis. J Rehabil Res Dev 2000;37(6):693–700.

Colombo, G., Wirz, M., Dietz, V.. Driven gait orthosis for improvement of locomotor training in paraplegic patients. Spinal Cord 2001;39(5):252–255.

Duschau-Wicke, A., von Zitzewitz, J., Caprez, A., Lunenburger, L., Riener, R.. Path Control: A Method for Patient-Cooperative Robot-Aided Gait Rehabilitation. IEEE Trans Neural Syst Rehabil Eng 2010;18(1):38–48.

Emken, J.L., Reinkensmeyer, D.J.. Robot-enhanced motor learning: accelerating internal model formation during locomotion by transient dynamic amplification. IEEE Trans Neural Syst Rehabil Eng 2005;13(1):33–39.

Goldsmith, M.. A Robotic Assessment of Lower Extremity Motor Adaptation. Master's thesis; Boston University; Boston University; 2010.

Hidler, J., Nichols, D., Pelliccio, M., Brady, K., Campbell, D.D., Kahn, J.H., Hornby, T.G.. Multicenter randomized clinical trial evaluating the effectiveness of the Lokomat in subacute stroke. Neurorehabil Neural Repair 2009;23(1):5–13.

Hogan, N.. Impedance control: An approach to manipulation, parts I, II, II. J Dynamic Syst Meas Control 1985;107:1–23.

Hornby, T.G., Campbell, D.D., Kahn, J.H., Demott, T., Moore, J.L., Roth, H.R.. Enhanced gait-related improvements after therapist- versus robotic-assisted locomotor training in subjects with chronic stroke: a randomized controlled study. Stroke 2008;39(6):1786–1792.

Husemann, B., Muller, F., Krewer, C., Heller, S., Koenig, E.. Effects of locomotion training with assistance of a robot-driven gait orthosis in hemiparetic patients after stroke: a randomized controlled pilot study. Stroke 2007;38(2):349–354.

Koenig, A.A., Omlin, X.X., Bergmann, J.J., Zimmerli, L.L., Bolliger, M.M., Müller, F.F., Riener, R.R.. Controlling patient participation during robot-assisted gait training. CORD Conference Proceedings 2011;8:14–14.

Lam, T., Anderschitz, M., Dietz, V.. Contribution of Feedback and Feedforward Strategies to Locomotor Adaptations. J Neurophysiol 2006;95(2):766–773.

Mayr, A.A., Kofler, M.M., Quirbach, E.E., Matzak, H.H., Fröhlich, K.K., Saltuari, L.L.. Prospective, blinded, randomized crossover study of gait rehabilitation in stroke patients using the Lokomat gait orthosis. Neurorehabil Neural Repair 2007;21(4):307–314.

Reinkensmeyer, D.J., Aoyagi, D., Emken, J.L., Galvez, J., Ichinose, W., Kerdanyan, G., Maneekobkunwong, S., Minakata, K., Nessler, J., Weber, R., Roy, R.R., de Leon, R., Bobrow, J.E., Harkema, S.J., Edgerton, V.. Tools for understanding and optimizing robotic gait training. J Rehabil Res Dev 2006;43(5):657–670.

Reisman, D.S., Block, H.J., Bastian, A.J.. Interlimb coordination during locomotion: what can be adapted and stored? J Neurophysiol 2005;94(4):2403–2415.

Reisman, D.S., Wityk, R., Silver, K., Bastian, A.J.. Locomotor adaptation on a split-belt treadmill can improve walking symmetry post-stroke. Brain 2007;130(Pt 7):1861–1872.

Riener, R., Lunenburger, L., Jezernik, S., Anderschitz, M., Colombo, G., Dietz, V.. Patient-cooperative strategies for robot-aided treadmill training: first experimental results. IEEE Trans Neural Syst Rehabil Eng 2005;13(3):380–394.

Scheidt, R.A.R., Reinkensmeyer, D.J.D., Conditt, M.A.M., Rymer, W.Z.W., Mussa-Ivaldi, F.A.F.. Persistence of motor adaptation during constrained, multi-joint, arm movements. J Neurophysiol 2000b;84(2):853–862.

Shadmehr, R., Mussa-Ivaldi, F.A.. Adaptive representation of dynamics during learning of a motor task. J Neurosci 1994;14(5 Pt 2):3208–3224.

Vallery, H., Duschau-Wicke, A., Riener, R.. Generalized elasticities improve patient-cooperative control of rehabilitation robots. In: Rehabilitation Robotics, 2009. ICORR 2009. IEEE International Conference on. 2009b. p. 535–541.

Veneman, J.F., Kruidhof, R., Hekman, E.E.G., Ekkelenkamp, R., van Asseldonk, E.H., van der Kooij, H.. Design and evaluation of the LOPES exoskeleton robot for interactive gait rehabilitation. IEEE Trans Neural Syst Rehabil Eng 2007;15(3):379–386.

Discussion

This thesis aimed to yield methods for improved lower extremity rehabilitation. We believe that improved patient outcomes will be achieved via the successful integration of knowledge about the underlying neural control of locomotion under a range of conditions and via characterization of the motor adaptations that result during gait retraining.

Neural Spike Train Analysis Toolbox (nSTAT)

We have developed the neural Spike Train Analysis Toolbox (nSTAT) for Matlab® to facilitate the use of the Point Process - Generalized Linear Model framework by the neuroscience community. By providing a simple software interface to PP-GLM specific techniques within the Matlab® environment, users of a number of existing open source toolboxes (i.e. Chronux, STAToolkit, etc.) will be able to easily integrate these techniques into their workflow. It is our hope that making nSTAT available in an open-source manner will shorten the gap between innovation in the development of new data analytic techniques and their practical application within the neuroscience community. For the neurophysiologist, we hope the availability of such a tool will allow them to quickly test the range of available methods with their data and use the results to both inform the quality of their data and refine the protocols of their experiments.

Via a series of examples we have demonstrated the use of the toolbox to solve many common neuroscience problems including: 1) systematic building of models of neural firing, 2) characterization of explicit experimental stimulus effects on neural firing, 3) spike rate estimation using the PSTH and extensions of the PSTH (SSGLM) that allow quantification of experience-dependent plasticity (across-trial effects), 4) receptive field estimation, and 5) decoding stimuli such as movement trajectories based on models of neural firing. All of the data, code, and figures used here are included as part of the toolbox. We hope that users will be able to easily modify these examples and use them as a starting point for analysis of their own data.

Decoding Movement Intent Information during Locomotion

In Chapter 3, we showed that the parametric model in Equation 3.18, was able to describe the firing activity of 558/573 neurons over three distinct walking conditions and over multiple days across 6 different animals. In order to demonstrate how such a model can be used to decode movement information for the control of prosthetic via brain machine interface (BMI) we provide a brief simulation example.

Figure 5.2 A shows the stereotypic hip and knee angles observed during bipedal human gait over the course of 2 steps. The gait phase, $\phi(t)$, is defined as the angle of the vector pointing to the current location in joint space during the gait cycle (see Figure 5.2 B). The origin of the coordinate system corresponds to the mean hip and knee coordinates over the gait cycles shown. We simulated an ensemble of $N = 50$ neurons with the following conditional intensity function

$$\text{logit}\left(\lambda^i(t_n)\Delta\right) = \mu_i + \alpha_1^i cos\left(\phi_y(t_n)\right) + \alpha_2^i sin\left(\phi_y(t_n)\right) \tag{5.2}$$

using the point process thinning algorithm (Lewis and Shedler, 1978, Ogata, 1981). The coefficients α_1^i and α_2^i were randomly selected from a uniform distribution on the interval $[-2,2]$ (e.g. $\alpha_k^i \sim U([-2,2])$ for $k = 1,2$ and $i = 1...N$) and $\mu_i \sim U([0,-4])$ for $i = 1...N$. This corresponds to a population of neurons whose preferred gait phase is uniformly distributed from 0 to 2π. The red circles in Figure 5.2 A and B indicate the preferred gait phase for each simulated neuron.

As shown in Figure 5.2 C, the graphical model for decoding latent state variables from point process observations allows for previous neural firing to affect the probability of current cell firing (e.g. cell refractoriness, bursting, etc.) (Srinivasan et al., 2007). For simplicity, in this example, we do not include the history effect (denoted by gray lines). In this case, the latent state variable is the vector $x_k = x(t_k) = [\cos(\phi(t)), \sin(\phi(t))]^T$.

Figure 5.2 D (top) shows the results of decoding the gait phase from the simulated spiking activity using the Point Process Adaptive Filter (PPAF) of Eden et al. (2004a). The actual gait phase, $\phi(t)$, and hip and knee angles ($\theta_{hip}(t)$ and $\theta_{knee}(t)$ respectively) are denoted by solid black lines. Solid blue line denotes the estimated gait phase $\hat{\phi}(t) = \tan^{-1}\left(\frac{\sin(\phi(t))}{\cos(\phi(t))}\right)$ along with the 95% confidence intervals for the estimate. The solid blue lines for the joint angles denote $\hat{\theta}_{hip}(t)$ and $\hat{\theta}_{knee}(t)$ defined as $\hat{\theta}_i(t) = \theta_i(t_{min})$ where $t_{min} = \text{argmin}_x\left(\left(\phi(x) - \hat{\phi}(t)\right)^2\right)$.

Our work in Chapter 3 showed that the preferred gait phase, background firing rate, and load-dependent firing coefficients show adaptation across loading condi-

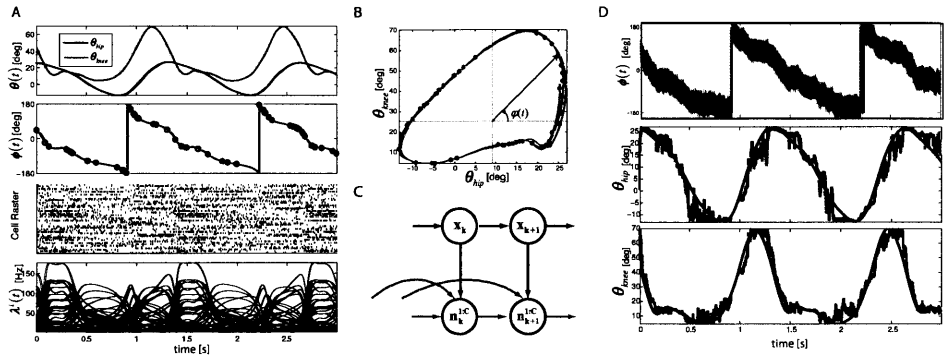

Figure 5.2: **Decoding Movement Intent Information during Locomotion using simulated data. A) Simulated Gait Data and Neural Rasters.** From top to bottom: Joint Angles for hip ($\theta_{hip}(t)$) and knee ($\theta_{knee}(t)$), gait phase ($\phi(t)$), cell raster, and conditional intensity functions ($\lambda^i(t)$) for each of the 50 cells simulated according to 5.2 using the point process thinning algorithm. **B) Gait cycle in Joint Coordinates.** $\phi(t)$ is defined as the angle of the vector pointing to the current location in joint space during the gait cycle. The origin of the coordinate system corresponds to the mean hip and knee coordinates over the gait cycles shown. Red circles indicate the location of maximal firing along the gait cycle for each simulated neuron (e.g. the preferred gait phase of each cell). **C) Probabilistic Graphical Model.** In general the graphical model for decoding latent state variables from point process observations allows for previous neural firing to affect the probability of current cell firing (e.g. cell refractoriness, bursting, etc.) (Eden et al., 2004a, Srinivasan et al., 2007). For simplicity, in this example, we do not include this effect (denoted by gray lines). In this case, the latent state variable is the vector $x_k = x(t_k) = [\cos(\phi(t)), \sin(\phi(t))]^T$. **D) Point Process Decoding Results.** Actual $\phi(t)$, $\theta_{hip}(t)$, and $\theta_{knee}(t)$ are denoted by solid black lines. Solid blue line denotes the estimated gait phase $\hat{\phi}(t) = \tan^{-1}\left(\frac{\sin(\phi(t))}{\cos(\phi(t))}\right)$ +/- one standard deviation computed based on the estimated latent state variables reconstructed from the point process observations. The solid blue lines for the joint angles denote $\hat{\theta}_{hip}(t)$ and $\hat{\theta}_{knee}(t)$ defined as $\hat{\theta}_i(t) = \theta_i(t_{min})$ where $t_{min} = \text{argmin}_x\left((\phi(x) - \hat{\phi}(t))^2\right)$.

tions and across days. Future work should aim to develop extensions of the PPAF to allow for tracking of parameter coefficients and covariates across time so that the effects of neural plasticity can be systematically studied.

Assessment of Lower Extremity Motor Adaptation

Numerous investigators have aim to study motor adaptation in the lower extremity(Emken and Reinkensmeyer, 2005, Reisman et al., 2007, Banala et al., 2009, Lam et al., 2006, Reisman et al., 2005). Unfortunately, the wide range of distinct devices used to conduct these studies make experiments difficult to validate. Moreover, the measures of adaptation reported change across studies. Taken together, these current limitations make it difficult if to easily compare results across experiments or to perform meta-analysis of the data available from various studies. We hope that by developing the LE-FFAP for a platform that is standardized and becoming widely available will help to produce study outcome measure that are more easily compared. Additionally, we hope that study protocols can become easily transferrable across institutions so that large scale trials can be undertaken.

Incorporating the LE-FFAP into clinical systems available around the world would open up a number of interesting possibilities. First, the LE-FFAP could be used as an assessment tool within current gait retraining strategies. Being able to understand the effects of distinct rehabilitation strategies on adaptation rates may allow for the identification of strategies that are more effective (e.g. yield larger adaptation rates or longer retention rates). In the long term, such assessment tools might allow clinicians to monitor the adaptation rates of individual patients and design interventions to maximize individual outcomes. Slightly less ambitious, but still insightful, would be the ability to track an individuals' adaptation rate over time. Much like hemoglobin A1C is a useful marker of blood sugar control in a diabetic patient, rates of adaptation may be indicative of the ability of the nervous system acquire new motor behaviors via rehabilitation. Lastly, because the LE-FFAP is analogous to its upper extremity counterpart, an extremely rich set of experimental protocols developed over the last 20 years can be directly applied to lower extremity research. Conversely, the LE-FFAP algorithm, suggests a natural approach for studying cyclical tasks (such as target tracking) in the upper extremity.

Future work will include the analysis of aggregate After-Effect and Error-Clamp experiments from 40 healthy adult subject at the conclusion of the ongoing clinical trial. Establishing an understanding of how healthy adults' motor systems adapt to external perturbations will be an important step towards understanding how the adaptive mechanisms involved in gait are altered by disease.

References

Banala, S., Kim, S.H., Agrawal, S., Scholz, J.. Robot Assisted Gait Training With Active Leg Exoskeleton (ALEX). Neural Systems and Rehabilitation Engineering, IEEE Transactions on 2009;17(1):2–8.

Eden, U.T., Frank, L.M., Barbieri, R., Solo, V., Brown, E.N.. Dynamic analysis of neural encoding by point process adaptive filtering. Neural Comput 2004a;16(5):971–998.

Emken, J.L., Reinkensmeyer, D.J.. Robot-enhanced motor learning: accelerating internal model formation during locomotion by transient dynamic amplification. IEEE Trans Neural Syst Rehabil Eng 2005;13(1):33–39.

Lam, T., Anderschitz, M., Dietz, V.. Contribution of Feedback and Feedforward Strategies to Locomotor Adaptations. J Neurophysiol 2006;95(2):766–773.

Lewis, P.A.W., Shedler, G.S.. Simulation methods for Poisson processes in nonstationary systems. In: WSC '78: Proceedings of the 10th conference on Winter simulation. IEEE Press; 1978. .

Ogata, Y.. On Lewis' simulation method for point processes. Information Theory, IEEE Transactions on 1981;27(1):23–31.

Reisman, D.S., Block, H.J., Bastian, A.J.. Interlimb coordination during locomotion: what can be adapted and stored? J Neurophysiol 2005;94(4):2403–2415.

Reisman, D.S., Wityk, R., Silver, K., Bastian, A.J.. Locomotor adaptation on a split-belt treadmill can improve walking symmetry post-stroke. Brain 2007;130(Pt 7):1861–1872.

Srinivasan, L., Eden, U.T., Mitter, S.K., Brown, E.N.. General-purpose filter design for neural prosthetic devices. J Neurophysiol 2007;98(4):2456–2475.